



Doctoral Thesis

## Design, characterization and simulation of avalanche photodiodes

**Author(s):**

Meier, Hektor Taavi Josef

**Publication Date:**

2011

**Permanent Link:**

<https://doi.org/10.3929/ethz-a-006445001> →

**Rights / License:**

[In Copyright - Non-Commercial Use Permitted](#) →

This page was generated automatically upon download from the [ETH Zurich Research Collection](#). For more information please consult the [Terms of use](#).

# Design, Characterization and Simulation of Avalanche Photodiodes



Diss. ETH No. 19519

# Design, Characterization and Simulation of Avalanche Photodiodes

A dissertation submitted to  
ETH ZURICH

for the degree of  
Doctor of Sciences

presented by

HEKTOR TAAVI JOSEPH MEIER

Dipl. El.-Ing. ETH  
born April 6th, 1981  
citizen of Aristau AG, Switzerland

accepted on the recommendation of

Prof. Dr. Wolfgang Fichtner, examiner  
Prof. Dr. Bernd Witzigmann and Dr. Markus Blaser,  
co-examiner

2011



# Abstract

Avalanche photodiodes (APDs) are high-sensitivity, semiconductor photo-detectors. In this work, two APDs for next generation 10 Gbit/s fiber-to-the-home (FTTH) passive optical networks (PON) are designed, characterized and analyzed. Furthermore, a prototype of a 25 Gbit/s APD is presented.

The three mesa InAlAs/InGaAs separated absorption, charge and multiplication (SACM) APDs show a low breakdown voltage with a small temperature dependence. The maximal  $-3$  dB bandwidth is 6.7 – 11.8 GHz and the gain-bandwidth product is larger than 80 GHz. The measured sensitivity of a prototype receiver at 10 Gbit/s for a BER of  $10^{-9}$  is better than  $-27$  dBm which makes this devices eligible for next generation 10 Gbit/s PON.

The analysis of the temperature dependence of the dark current identifies generation-recombination within the InGaAs absorber as the dominating mechanism. The dark current activation energies of APDs with avalanche and tunneling breakdown are compared. Based on S11 and S12 measurements, the impact of RC-limitations on the bandwidth is analyzed and a transit time limited bandwidth is extracted. The effect of low electric field in the absorber region on the transport of holes and the device bandwidth is analyzed. This effect concerns SACM APDs with high punch-through and low breakdown voltage.

The analysis is supported by the simulation of carrier transport within the APD in presence of fast changing, high electric fields and transport across hetero-junction band diagram energy offsets. For this purpose, a transport simulator based on the Monte Carlo (MC) method is implemented. The band structure is represented by a

spherical, non-parabolic approximation with three conduction band and three valence band valleys. The simulation results show good agreement with measurements and give insight to performance critical physics, such as carrier velocity overshoots and non-local impact ionization. The simulator allows a quantitative design optimization of future APD devices.

# Zusammenfassung

Lawinenmultiplikation-Photodioden, in engl. avalanche photodiodes (APD), sind hoch sensitive, halbleiterbasierte Photodetektoren. Diese Arbeit beschäftigt sich mit dem Entwurf, der Charakterisierung und der Analyse der nächsten Generation dieser Dioden für die Verwendung in  $10^{\text{Gbit/s}}$  passiven faseroptischen Telekommunikationsnetzwerken, in engl. fiber-to-the-home (FTTH) passive optical networks (PON). Der Prototyp einer APD für  $25^{\text{Gbit/s}}$  wird präsentiert.

Drei InAlAs/InGaAs Mesa-APDs mit getrennter Absorption, Ladungs- und Multiplikationsregion, in engl. separated absorption, charge and multiplication (SACM), werden präsentiert. Die Dioden zeigen tiefe Durchbruchspannung mit einer kleinen Temperatureabhängigkeit. Die maximale  $-3\text{ dBe}$  Bandbreite liegt bei  $6.7 - 11.8\text{ GHz}$  und das Verstärkungsbandbreiteprodukt ist höher als  $80\text{ GHz}$ . Die gemessene Sensitivität eines Prototypempfängers bei  $10^{\text{Gbit/s}}$  für eine BER von  $10^{-9}$  ist besser als  $-27\text{ dBm}$ . Die APD kann daher für die nächste Generation von  $10^{\text{Gbit/s}}$  PON verwendet werden.

Die Analyse der Temperaturabhängigkeit des Dunkelstroms zeigt eine Dominanz der Generation-Rekombinationsmechanismen in der InGaAs Absorberregion. Ein Vergleich der Dunkelstromaktivierungsenergien für APDs mit Lawinen- und Tunneldurchbruch wird gezeigt. Basierend auf S11 und S12 Messungen wird der Einfluss der RC-Limitierung in allen drei APDs analysiert und eine transitzeitabhängige Bandbreite ermittelt. Es zeigt sich, dass ein zu kleines elektrisches Feld in der Absorberregion, zu einer suboptimalen maximalen Bandbreite

führt, da Löchern nicht mit der Sättigungsgeschwindigkeit transportiert werden. Insbesondere SACM APDs mit hoher Durchreichspannung, engl. punch-through voltage, und tiefer Durchbruchspannung, engl. breakdown voltage, sind davon betroffen.

Die Analyse der APD wird durch die Simulation des nichtgleichgewicht Transports in Präsenz von schnell ändernden, hohen elektrischen Feldern und Heteroübergängen unterstützt. Zu diesem Zweck wurde ein Trägertransport-Simulator basierend auf der Monte Carlo (MC) Methode entwickelt. Die Bandstruktur wird durch eine sphärische, nichtparabolische Näherung repräsentiert. Die Simulationsergebnisse sind in guter Übereinstimmung mit den Messresultaten. Der Simulator erlaubt den Einblick in die Physik der APD. Geschwindigkeitsüberschüsse der Ladungsträger und nicht-lokale Stossionisierung werden analysiert. Dies ermöglicht die Optimierung des Entwurfs zukünftiger APDs.

# Contents

<b>Abstract</b>	<b>v</b>
<b>Zusammenfassung</b>	<b>vii</b>
<b>1 Introduction</b>	<b>1</b>
1.1 Motivation . . . . .	1
1.2 Scope . . . . .	2
<b>I Design of Avalanche Photodiodes</b>	<b>3</b>
<b>2 Avalanche Photodiode</b>	<b>5</b>
2.1 Fields of Application . . . . .	5
2.1.1 Fiber-to-the-Home . . . . .	5
2.1.2 Optical Ethernet Link . . . . .	7
2.1.3 Optical Interconnects . . . . .	7
2.2 Avalanche Multiplication . . . . .	8
2.3 Non-local Impact Ionization . . . . .	11
2.4 SACM APD . . . . .	12
2.4.1 Device Structure and Fabrication . . . . .	13
2.4.2 Multiplication Layer Material . . . . .	15
2.4.3 Reliability and Reproducibility . . . . .	16
2.5 Basic Functional Principle . . . . .	17
2.6 Steady-State Characteristics . . . . .	18
2.6.1 Quantum Efficiency and Responsivity . . . . .	18
2.6.2 Dark and Photo Current . . . . .	19

2.6.3	Punch-Through Voltage . . . . .	21
2.6.4	Avalanche Breakdown Voltage . . . . .	22
2.6.5	Field Control Layer . . . . .	23
2.7	Sensitivity . . . . .	24
2.7.1	Excess Noise Factor . . . . .	24
2.7.2	Optimal Operation Point . . . . .	25
2.8	Device Bandwidth . . . . .	27
2.9	Transient Characteristics . . . . .	28
2.9.1	RC-Limitation . . . . .	28
2.9.2	Dielectric Relaxation Time . . . . .	29
2.9.3	Transit Time Limitation . . . . .	30
2.9.4	Avalanche Build-Up Time . . . . .	32
2.10	k-Ratio Improvement . . . . .	34
2.10.1	Multiplication Layer Thickness . . . . .	34
2.10.2	Band Gap Engineering . . . . .	34
<b>3</b>	<b>APD Design</b>	<b>37</b>
3.1	Design of Epitaxial Structure . . . . .	37
3.2	APD Devices . . . . .	39
<b>4</b>	<b>Measurement Analysis Results</b>	<b>43</b>
4.1	Capacitance-Voltage Characteristics . . . . .	43
4.2	Stationary VI-characteristics . . . . .	44
4.2.1	Definitions . . . . .	44
4.2.2	Setup . . . . .	45
4.2.3	Dark Current . . . . .	46
4.2.4	Photo Current . . . . .	48
4.2.5	Responsivity . . . . .	49
4.2.6	Multiplication Gain . . . . .	50
4.2.7	Breakdown Voltage Temperature Dependence . . . . .	51
4.2.8	Dark Current Temperature Dependence . . . . .	52
4.2.9	Dark Current Dependence on Diameter . . . . .	54
4.3	Dynamic Characteristics . . . . .	56
4.3.1	Frequency Domain Measurement Setup . . . . .	56
4.3.2	S11 Results . . . . .	57
4.3.3	S12 Results . . . . .	60
4.3.4	Time Domain Measurement Setup . . . . .	66
4.3.5	Rise- and Fall-Time . . . . .	66

4.3.6	Rise- and Fall-Time Measurement . . . . .	66
4.3.7	Sensitivity . . . . .	70
4.3.8	Eye Diagram . . . . .	70
4.4	Summary . . . . .	73
4.4.1	Design . . . . .	73
4.4.2	Analysis . . . . .	73
<b>II</b>	<b>Simulation of Avalanche Photodiodes</b>	<b>75</b>
<b>5</b>	<b>Simulation of Avalanche Photodiodes</b>	<b>77</b>
5.1	Simulation Model Requirements . . . . .	77
5.1.1	Non-Equilibrium Transport . . . . .	77
5.1.2	Non-Local Impact Ionization . . . . .	81
5.1.3	Carrier Energy . . . . .	81
5.1.4	Summary . . . . .	82
5.2	Boltzmann Transport Equation . . . . .	83
5.3	State-of-the-art APD Simulations . . . . .	85
5.4	Monte Carlo Method . . . . .	87
5.4.1	Introduction . . . . .	87
5.4.2	Physical Models . . . . .	87
5.4.3	Statistical Enhancement . . . . .	90
5.4.4	Self-Scattering Reduction . . . . .	93
5.4.5	Poisson Equation . . . . .	94
5.4.6	Carrier Propagation . . . . .	95
5.4.7	Simulator Overview . . . . .	97
<b>6</b>	<b>Monte Carlo Calibration Results</b>	<b>101</b>
6.1	Bulk Properties . . . . .	101
6.1.1	Simulation Procedure . . . . .	102
6.1.2	Bulk Mean Carrier Velocity and Energy . . . . .	102
6.1.3	Bulk Impact Ionization Rate . . . . .	106
6.2	PIN Diode . . . . .	107
6.2.1	Simulation Procedure . . . . .	107
6.2.2	Simulation Results . . . . .	109

<b>7</b>	<b>APD Simulation Results</b>	<b>115</b>
7.1	Capacitance vs. Voltage . . . . .	115
7.1.1	Introduction . . . . .	115
7.1.2	CV-Fit . . . . .	116
7.2	FFMC Computation Time . . . . .	119
7.3	FFMC w/o Band Diagram Offset . . . . .	120
7.3.1	Gain vs. Voltage . . . . .	120
7.3.2	Multiplication Excess Noise . . . . .	122
7.3.3	Impact Ionization Profile . . . . .	123
7.3.4	Carrier Arrival Time . . . . .	124
7.3.5	Gain-Bandwidth Characteristics . . . . .	127
7.4	FFMC with Band Diagram Offset . . . . .	130
7.4.1	Carrier Arrival Time . . . . .	130
7.4.2	Gain-Bandwidth Characteristics . . . . .	132
7.5	SCMC . . . . .	134
7.5.1	General Remarks . . . . .	134
7.5.2	Computation Time . . . . .	134
7.5.3	Device A . . . . .	135
7.5.4	Device B . . . . .	138
7.6	Summary . . . . .	142
<b>III</b>	<b>Conclusion</b>	<b>145</b>
<b>8</b>	<b>Conclusion and Outlook</b>	<b>147</b>
8.1	Conclusion . . . . .	147
8.2	Outlook . . . . .	148
<b>A</b>	<b>MC Simulation Flow</b>	<b>151</b>
<b>B</b>	<b>Scattering Rate Formula</b>	<b>153</b>
B.1	Polar Optical Phonon Scattering . . . . .	153
B.2	Non-Polar Optical Phonon Scattering . . . . .	154
B.3	Elastic Acoustic Phonon Scattering . . . . .	154
B.4	Alloy Scattering . . . . .	155
B.5	Impact Ionization . . . . .	155
B.6	Electron Intervalley Scattering . . . . .	156

<b>C Monte Carlo Material Parameters</b>	<b>157</b>
C.1 $\text{In}_{0.53}\text{Ga}_{0.47}\text{As}$ . . . . .	157
C.2 $\text{In}_{0.52}\text{Al}_{0.48}\text{As}$ . . . . .	160
<b>D Scattering Rates</b>	<b>163</b>
<b>E Drift-Diffusion Simulation Parameters</b>	<b>169</b>
<b>F Static Dielectric Constant</b>	<b>171</b>
<b>Bibliography</b>	<b>173</b>



# Chapter 1

## Introduction

### 1.1 Motivation

Future video-based services require an increased data rate in access networks as well as in large data centers. In the long term, the bandwidth can only be guaranteed by fiber optical transmission media [1]. High-speed avalanche photodiodes (APDs) provide the sensitivity and speed needed for next generation fiber optical transmission systems. APDs provide up to 5-10 dB higher sensitivity than PIN photodiodes. They are suited for applications with weak light signal and nevertheless high bandwidth requirements. This work focuses on devices for future 10G optical access networks (IEEE 802.3av) as well as for 40G and 100G fiber optical ethernet links (IEEE 802.3ba).

Even though APDs are well established devices many questions remain unsolved. This is mainly due to extended possibilities of modern semiconductor technology. Today's fabrication technologies allow field shaping, band gap engineering, use of hetero-structured materials on the nanometer scale and strongly reduced device dimensions.

Avalanche multiplication provides the desired signal amplification in APDs. The required carrier energies for avalanche multiplication is in the order of the band gap of the material. Dynamics of the carriers in presence of fast changing, high electric fields and sudden

band diagram energy offsets are essential for the accurate description of the avalanche multiplication process.

From a modeling point of view, drift-diffusion (DD) remains a very popular transport model in semiconductor device simulation. Standard DD models give a good description of carrier transport at low carrier energies. However, DD models fail to describe transport on a small device scale, for which the carrier energy distribution can not be described by an equilibrium function.

Only an accurate modeling of non-equilibrium transport and non-local impact ionization allows for an analysis of current state-of-the-art APDs and reveals optimization potential for future high-speed devices. The study of hot carrier effects can directly be applied to other modern semiconductor devices with small dimensions and large, fast changing electric fields.

## 1.2 Scope

This thesis presents concepts and results for the simulation, the design and the analysis of state-of-the-art APDs.

The work is divided in two main parts. Part one gives an introduction to basic physics and concepts of APDs. A series of new APD devices have been designed, fabricated and characterized. The analysis of the measurement results enhances the knowledge on this type of detectors and allows for a targeted design improvement in future devices.

Part two introduces the Monte Carlo (MC) simulation framework. Multiplication gain, impulse response, impact ionization, carrier velocity and energy profiles are analyzed. The calibrated simulation model provides a tool for predictive, physic-based design improvements of new high-speed APDs.

## Part I

# Design of Avalanche Photodiodes



# Chapter 2

## Avalanche Photodiode

The aim of this chapter is to give an overview on the field of applications, basic physics, trade-offs and current state-of-the-art of APD technology.

### 2.1 Fields of Application

The following list is not exhaustive. The focus is on major emerging fields of application for state-of-the-art high-speed telecommunication APDs.

#### 2.1.1 Fiber-to-the-Home

Video-based services such as video-on-demand (VOD), high definition IP TV (HD-IPTV), video conferencing, voice over IP (VoIP) or remote storage applications are the main drivers for increased bandwidth requirements in modern access networks [2]. Such services ask for guaranteed-symmetric bandwidth as well as high quality of service. Twisted-pair copper cables provide a bandwidth length product of approximative  $10 \text{ Mbkm/s}$  while single mode optical fibers offer  $10^6 \text{ Mbkm/s}$  [1]. Fiber losses can be as low as  $0.15 - 0.5 \text{ dB/km}$  [1, 3], independent of transmission bandwidth. A well established international standard for the distance between central office and subscriber location is 20 km

[1, 4]. Over such a distance the bandwidth for video-centric services can only be provided using an optical fiber transmission media in proximity of every subscriber. Such installations are called fiber-to-the-home or premise (FFTH/P) networks.

Passive optical networks (PON) are a popular architecture for FTTH [2]. They form a point-to-multipoint network with no active components between the central office and subscriber. A single segment of gigabit-capable PON (GPON) is typically split between 32 subscribers [2]. Point-to-point connection would be advantageous and future proof regarding bandwidth requirements. However, this solution would not be cost efficient due to the large number of required fibers [1]. The point-to-multipoint architecture allows to easily expand the number of subscribers. Deployment of the network does not ask for any electrically powered active components which reduces installation and maintenance cost [2]. Due to the optical transparency of PON a long lifetime of the fiber network is expected. In order to upgrade a system only transmitter and receiver need to be replaced.

The next generation 10 GPON (ITU-T G.987, to be ratified) and 10G EPON (IEEE 802.3av, ratified September 2009) are to be deployed around 2011-2013 [2]. IEEE 802.3av defines standards for the physical and data link layers of the standard open system interconnection (OSI) model. The data rate for downstream (DS) at  $\lambda = 1575 - 1580$  nm and upstream (US) at  $\lambda = 1260 - 1280$  nm are 10G in symmetric or 10G/1G in an asymmetric configuration. The combination of high sensitivity and high bandwidth requirements can only be provided by APDs. Some key specifications for the receiver in a IEEE 802.3av standard are summarized in Tab. 2.1 [2]. The sensitivity in Tab. 2.1 is given for a bit-error-rate (BER) of  $10^{-3}$  before forward error correction (FEC). FEC is mandatory for 10G EPON. The undecoded-BER corresponds approximately to a decoded-BER of  $10^{-12}$  [2]. Without FEC, for a reach of 20 km and for a BER of  $10^{-9}$ , a sensitivity of approximately  $-27$  dBm should be reached at  $10 \text{ Gb/s}$ .

Further requirements for APDs in 10G EPON are high yield and low manufacturing costs in order to hit a price target of approximately  $6 - 10$  \$/unit. High reliability in harsh environments with temperature variations between  $-40^\circ\text{C}$  to  $100^\circ\text{C}$  and  $< 1\%$  failure in 10–20 years are required. The light sensitive area should be  $> 30 \mu\text{m}$  for low-cost

class	PR10		PR20		PR30	
type	DS	US	DS	US	DS	US
distance (km)	10	10	10/20	10/20	20	20
split ratio	1:16	1:16	1:32/16	1:32/16	1:32	1:32
receiver type	PIN	APD	PIN	APD	APD	APD
sensitivity (dBm)	-20.5	-24	-20.5	-28	-28.5	-28
damage level (dBm)	1	0	1	-5	-9	-5

Table 2.1: Key parameters for optical receiver in 10G EPON (IEEE 802.3av). Table adapted from [2].

coupling to single-mode fibers. The breakdown voltage should be low to reduce power consumption as well as to relax the requirements on the bias circuitry.

### 2.1.2 Optical Ethernet Link

The growing traffic demand on the network backbone increases the bandwidth requirements on data aggregation points. Higher ethernet bandwidth is needed to avoid potential bottlenecks in server and storage applications. In June 2010 the IEEE 802.3ba standard for 40 Gb/s and 100 Gb/s ethernet has been ratified. The standard includes parallel transmission over 4 wavelengths at 25 GHz. The sensitivity requirements create a major interest in development of new 25 GHz APDs.

### 2.1.3 Optical Interconnects

Many of today's supercomputing and server systems rely on optical rack to rack interconnects which provide a power and space efficient solution for the growing amount of data transfer. For next generation exascale computing systems [5] it is considered to use optical links on short distances from few mm for on-chip and several cm for on-off-chip communication. Silicon integrated optical waveguides provide potentially low loss, highly scalable optical interconnects with a high wiring density [6]. The main drawback using optical interconnects is

the power consumption of electro-optical and optical-electrical conversion [5] which in general uses more power than it is gained by the low link loss. In [5] it is concluded that today's optical interconnects are highly unoptimized and therefore are not yet suited for such applications. One main reason appears to be a lack of research in this field due to a missing mass market. This may change as soon short range optical interconnects are considered to be applied for mainstream computing.

The internal signal gain of avalanche photodetector technology allows to detect low power optical signals which relaxes the optical power budget for other components. The internal signal gain may result in a significant reduction of required on-chip area for optical transmitters as well as transimpedance amplifiers and therefore decreases costs and power consumption. Challenges are CMOS compatible integration technology, high reliability and low temperature dependence to reduce temperature control. The photo-detector should provide low dark current, small footprint, low power consumption as well as a low CMOS compatible bias voltage. In the long term, an integrated optical transceiver (RX+TIA) should present a power budget of approximately  $0.05 - 0.5 \text{ pJ/bit}$  for a total link power of  $0.21 - 0.75 \text{ pJ/bit}$  [5].

To operate avalanche photodetectors at a low bias voltage the device has to be scaled aggressively. Non-local impact ionization and non-equilibrium transport effects have to be exploited to achieve the required performance. For an example of the integration of avalanche photodetectors based on monolithic germanium (Ge) and silicon refer to [7] for a vertical illuminated APD and to [6] for a waveguide photodetector structure.

Development of high-performance, small scale APDs requires an extensive understanding on non-equilibrium transport effects which can be provided by accurate simulation tools.

## 2.2 Avalanche Multiplication

The high sensitivity of APDs results from internal signal gain by means of avalanche multiplication. Photon generated electrons and holes are multiplied which increases the initial photo current.

The charge carriers gain energy in the presence of the electric field or a band diagram energy offset occurring at hetero-interfaces. The ballistic flight of the carrier is regularly interrupted by scattering with the lattice, impurities or other carriers which may alter its energy and its propagation. If the electric field is strong enough, the carrier can achieve an energy  $E_1$  which is larger than the band gap energy  $E_g$ . At that point the carrier is eligible to create a new electron-hole pair by means of impact ionization which is illustrated in Fig. 2.1. The initial carrier and its two children share the remaining energy  $E_1 - E_g = E'_1 + E'_2 + E'_3$ . The three carriers propagate further and may lead to another impact ionization event. A chain of such impact ionization events is called avalanche multiplication. Avalanche breakdown occurs if avalanche multiplication goes towards infinity.

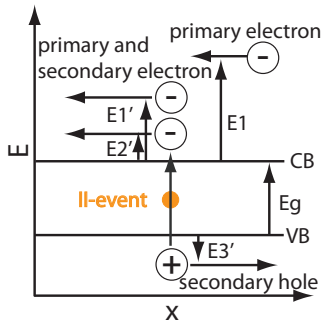


Figure 2.1: Schematic representation of an electron induced impact ionization event.

The inverse of the mean distance between two consecutive impact ionization events is called impact ionization rate,  $\alpha$  for electrons and  $\beta$  for holes [8]. In general,  $\alpha$  and  $\beta$  increase with the applied electric field because the carrier achieves the required energy for an impact ionization event over a smaller distance. The impact ionization rates decrease for higher temperature because an increased phonon scattering rate [9] is slowing down the acceleration process. An analytic,

phenomenological expression of the impact ionization rate vs. electric field  $E$  is given by [10]

$$\alpha(E) = a_e e^{\left(-\frac{b_e}{E}\right)^{c_e}} \quad (2.1)$$

$$\beta(E) = a_h e^{\left(-\frac{b_h}{E}\right)^{c_h}} \quad (2.2)$$

with  $a_e, b_e, c_e, a_h, b_h$  and  $c_h$  being parameters to fit the measured impact ionization rates in a bulk material. The ratio between hole and electron impact ionization is called impact ionization ratio or  $k$ -ratio [8]

$$k = \frac{\beta}{\alpha}. \quad (2.3)$$

The  $k$ -ratio is an important parameter for APDs since it determines device bandwidth and noise which will be shown in Sec. 2.7 and Sec. 2.9.4. For an electron multiplying material for which  $\alpha > \beta$ , it is desirable to have a very low  $k$ -ratio. This means that  $\alpha \gg \beta$ . For a hole multiplying material the  $k$ -ratio should be as large as possible or  $\alpha \ll \beta$ .

The multiplication gain  $M$  represents the ratio between multiplied total current  $J = J_n + J_p$  and initial injected current. Multiplication gain is classified according to the type of carrier which initiates the avalanche multiplication process.  $M_n$  is the electron induced multiplication gain and  $M_h$  is the hole induced multiplication gain. In an analytical form  $M_n$  can be expressed by [11]

$$M_n = \frac{J}{J_n(0)} = \frac{e^{\psi(W)}}{1 - \int_0^W \beta(x') e^{x'} dx'} \quad (2.4)$$

with

$$\psi(x) = \int_0^x (\alpha(x') - \beta(x')) dx', \quad (2.5)$$

with  $J_n(0)$  being the injected electron current at position zero. The gain depends on electron and hole impact ionization rates as well as the width of the multiplication region  $W$ .

## 2.3 Non-local Impact Ionization

The above description is based on a local impact ionization theory. Local impact ionization models relate  $\alpha$  and  $\beta$  at any point in the device to local material properties and the local electric field. Non-local impact ionization takes into account the history of the carrier prior to the impact ionization event, e.g. changes in carrier energy due to the electric field or band diagram profile.

Fig. 2.2 shows the probability density function (PDF) of the distance before a first impact ionization event for an electron starting with zero kinetic energy. A local analytic model and a non-local model are compared for various electric fields. In both cases the bulk impact ionization rate  $\alpha$  is the same.

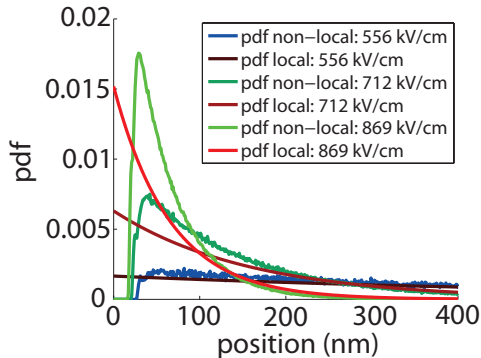


Figure 2.2: Normalized distribution of the distance of the first impact ionization event for an initial carrier energy of 0 eV in  $\text{In}_{0.52}\text{Al}_{0.48}\text{As}$ . Compared are a non-local impact ionization model based on MC and an analytical local model. The bulk impact ionization rate  $\alpha$  is the same in both cases.

The non-local model shows an electric field dependent dead-space. The dead-space represents the distance a carrier requires to achieve the threshold energy for an impact ionization event [12]. In general, the dead-space for electron- and hole-induced impact ionization are not the same due to different scattering probabilities and different effective carrier masses. For increasing electric field the dead-space

decreases because the carriers achieve the required energy for an impact ionization event over a smaller distance. The PDF of subsequent impact ionization events behave similar. However, the dead-space and the shape of the PDF is altered due to the non-zero initial carrier energy. The effect of dead-space starts to influence the performance in thin multiplication regions for which the dimension of the dead-space becomes comparable.

The PDF in the non-local case is becoming more narrow for high electric fields. This means that the position of the impact ionization events are becoming more deterministic [12]. This reduces the variation in numbers of impact ionization events every carrier will cause which lowers the excess noise related to the ionization process (see Sec. 2.7).

## 2.4 SACM APD

The first avalanche photodiode concepts were based on strongly reverse-biased PIN diodes [13, 14]. The intrinsic region consists of a material with low band gap energy to absorb light in the desired wavelength. At the same time, this layer provides avalanche multiplication by means of impact ionization. The high field required for the avalanche multiplication process gives rise to strong band-to-band-tunneling resulting in a large dark current. In a separated absorption and multiplication (SAM) structure the electric field in the absorption region is low, while the electric field in the multiplication region is high [14]. The use of a large band gap material for the multiplication layer becomes possible which reduces the band-to-band-tunneling probability.

To reduce transit time and sensitivity of the APD, the thickness of the multiplication region needs to be reduced (see Sec. 2.7 and Sec. 2.9.4). Further reduction of device thickness and therefore higher electric fields within the structures asks for an additional field separation layer. The so called field control layer between the multiplication layer and the absorber layer provides an additional well definable field separation. The so called separated absorption, charge and multiplication (SACM) structure allows to further decrease the multiplication layer thickness while keeping the field in the absorber low.

### 2.4.1 Device Structure and Fabrication

The III-V APDs in this work are based on indium phosphide (InP), lattice matched indium aluminum arsenide ( $\text{In}_{0.52}\text{Al}_{0.48}\text{As}$ ) and indium gallium arsenide ( $\text{In}_{0.53}\text{Ga}_{0.47}\text{As}$ ) as well as linear interpolations between the latter two ternary materials. From now on, we refer to the ternary materials as InAlAs and InGaAs, respectively. For the linear interpolated, lattice matched material  $\text{In}_{1-x-y}\text{Al}_x\text{Ga}_y\text{As}$  with  $x = 0.25$  and  $y = 0.23$  we use the term InAlGaAs.

The schematic of a typical InAlAs/InGaAs layer structure of a cylindrical mesa SACM APD is shown in Fig. 2.3. The purpose of each layer is tabulated in Tab. 2.2. Dimension and doping densities of each layer are discussed in Sec. 3.1.

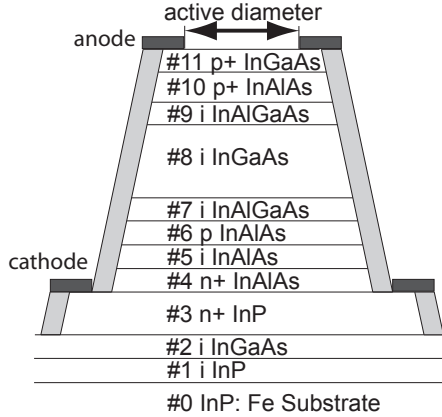


Figure 2.3: Schematic layer structure of a SACM mesa APD.

The majority of our devices are fabricated by a molecular beam epitaxy (MBE). The p-type dopant in that case is beryllium (Be) and the n-type dopant is silicon (Si). In a post-processing step a mesa is etched to provide lateral field confinement. Next, the structure is passivated using a silicon nitride (SiN) process and p- and n-side metallizations are applied. If the device is front-illuminated the inner

layer	material	type	purpose
#0	InP	n	substrate
#1	InP	undoped	buffer
#2	InGaAs	undoped	etch-stop
#3	InP	n <sup>+</sup>	n-side contact layer
#4	InAlAs	n <sup>+</sup>	current spreading buffer
#5	InAlAs	undoped	multiplication
#6	InAlAs	p	field control layer
#7	InAlGaAs	undoped	grading, reduced electron pile-up
#8	InGaAs	undoped	light absorption
#9	InAlGaAs	undoped	grading, reduced hole pile-up
#10	InAlAs	p <sup>+</sup>	current spreading buffer
#11	InGaAs	p <sup>+</sup>	p-side contact layer

Table 2.2: Typical layer structure of a SACM APD.

diameter of the p-contact metallization ring defines the active diameter. If the device is bottom illuminated the p-contact is used as mirror and allows to increase the responsivity of the structure.

## Growth Technology

The epitaxial structure of the SACM APD can be grown for example by MBE or metallorganic vapor phase epitaxy (MOVPE).

MBE is performed in ultra high vacuum. The pure source material is sublimated in heated furnaces and forms a constant beam of atoms. This beam streams with very few collisions upon a heated substrate where the material is deposited and forms an epitaxial layer [15]. MBE offers very abrupt, even monoatomic, material boundaries. However, the process is time consuming, quite expensive compared to other technologies and very sensitive to the quality of the vacuum and to impurities. This makes MBE less reliable and cost efficient for mass production compared to MOVPE. However, MBE is very well suited for prototyping.

In MOVPE the semiconductor material is provided in form of metal-organic gases which are either at atmospheric or low pressure [15]. The gas flows over the heated substrate where it condensates, in general, in a diffusion-limited regime.

In both epitaxial growth technologies the dopant species are incorporated during the deposition process. The main advantage is the higher control of tight doping profiles compared to diffused or ion implanted profiles [15, 16]. Doping concentrations which can be achieved by epitaxial methods are  $5 \cdot 10^{15} \text{ 1/cm}^3$  to  $5 \cdot 10^{18} \text{ 1/cm}^3$  [15] for donors and  $5 \cdot 10^{15} \text{ 1/cm}^3$  to greater than  $1 \cdot 10^{19} \text{ 1/cm}^3$  [15] for acceptors. This good control of the doping profile is essential for the fabrication of high-performance SACM APDs. It provides a technique to implement highly doped, very thin field control layers (#6) surrounded by intrinsic material as well as to very precisely control the thickness of the multiplication layer (#4) [16].

### 2.4.2 Multiplication Layer Material

The choice of an appropriate material for the multiplication region depends on several factors.

1. The saturation velocity of the carriers should be as high as possible to provide fast transit times.
2. The material should provide a large band gap. The breakdown behavior should be dominated by avalanche breakdown instead of Zener breakdown [17]. This consideration is particularly important for thin multiplication layers for which a higher electric field is required to achieve the same multiplication gain compared to thick layers.
3. The  $k$ -ratio should be as small as possible for an electron injection design. This improves sensitivity as well as device speed in the high gain regime (see Sec. 2.7 and Sec. 2.9.4).
4. The temperature dependence of the impact ionization coefficients should be as small as possible to reduce the temperature dependence of the avalanche breakdown voltage (see Sec. 2.6.4).

5. The material should be reliable in production and allow the combination with an absorber material in the telecommunication wavelength of 1350 – 1550 nm.

Many modern telecommunication APDs are based on the III-V material group. Popular material combinations include InP matched InAlAs and InGaAs. This is due to the absorption properties of InGaAs, the favorable properties of InAlAs as multiplication layer, the possibilities for band gap engineering by modification of the material composition as well as the mature growth technology. InAlAs has a bulk  $k$ -ratio of approximately  $\beta/\alpha = 0.29 - 0.5$  [18]. In comparison, InP is a hole multiplication material with  $\alpha/\beta = 0.4 - 0.5$  [12].  $\text{Al}_x\text{Ga}_{1-x}\text{As}$  shows a very low  $k$ -ratio of approximately  $\beta/\alpha = 0.2$  ( $x = 0.8$ ) [19]. For  $x < 0.6$  this ratio becomes significantly higher. Silicon is a good multiplication material with a  $k$ -ratio of approximately 0.02 – 0.03 [20] to 0.1 [7]. However, Si is transparent in the telecommunication wavelength. This asks for sophisticated wafer bonding on InGaAs in order to become useful for telecom applications [21].  $\text{Hg}_{0.7}\text{Cd}_{0.3}\text{Te}$  shows an effective  $k$ -ratio of  $\beta/\alpha = 0$  up to a gain of 100 [22]. Theoretically, this is the ideal  $k$ -ratio. Monte Carlo simulation [23] suggest that this particular effect is due to the large ratio of the hole and electron effective mass and the larger scattering rate for holes. Furthermore, due to a small inter-valley scattering rate, electrons remain in the  $\Gamma$ -valley and show a significantly lower impact ionization threshold energy than holes [23].

Material properties for the use in APD devices are not in all cases well known. In the long term, ab-initio band calculations are required, assisted by MC simulation of impact ionization rates to find materials with intrinsically low  $k$ -ratio.

### 2.4.3 Reliability and Reproducibility

In general, it is assumed that planar structures are more reliable than mesa structures [12, 24–26]. The exposed junction edges of the mesa structure may lead to instability of the dark current [24] due to degradation caused by thermal over-stress or chemical instability. Long term reliability of passivated mesa APD structures remains a topic of current research.

However, MBE or MOVPE grown mesa structures show higher reproducibility than planar structures with diffused junctions. This is an important factor for commercial success. In planar structures, the p+–side is in most cases achieved by zinc (Zn) diffusion in one or two diffusion steps [27]. The exact positioning and shape of the diffusion front are essential for a reproducible breakdown voltage. Lateral field confinement and prevention of edge breakdown in planar structures can be provided by Zn diffusion of guard rings [25,27]. However, these are difficult to fabricate in reproducible manner [28]. Another way to shape the electric field in lateral direction is to etch the surface [29], to use regrowth techniques [28] or to implement spatially confined charge control layers [16].

## 2.5 Basic Functional Principle

Fig. 2.4(a) shows a band diagram of a typical SACM APD in an electron multiplication configuration. A primary electron-hole pair is created due to optical absorption in the absorber region (1). The primary hole drifts through the absorber towards the p-side of the depletion region. The electron is injected into the high field region (2) where it is accelerated due to the strong gradient in the conduction band. It may eventually create a secondary electron-hole pair by means of impact ionization (3). The primary and secondary electron continue to travel towards the n-side of the depletion region. The secondary hole is accelerated towards the absorber region. All of them may or may not impact ionize again (4). The secondary holes will finally enter the low field absorber region (5) and continue to travel towards the p-side of the depletion region. The electrons leaving the depletion region on the n-side and the holes leaving the depletion region on the p-side represent majority carriers in these layers. It can be assumed that the space charge barrier prevents majority carriers to enter the depletion layer again [3].

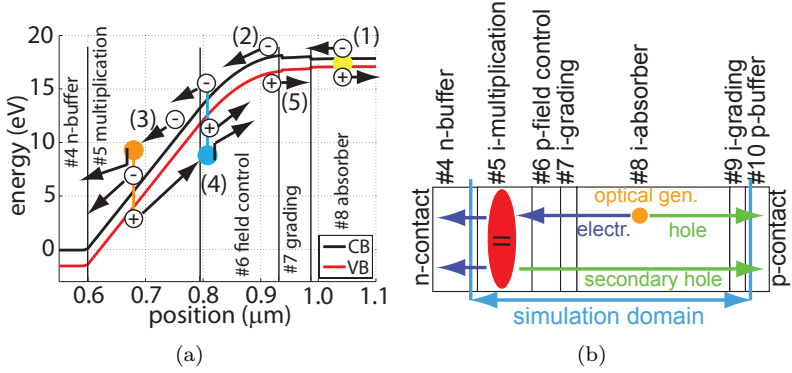


Figure 2.4: Functional principle of a SACM APD: (a) schematic band diagram and typical history of photo generated charge carriers, (b) schematic of the drift transport.

## 2.6 Steady-State Characteristics

### 2.6.1 Quantum Efficiency and Responsivity

Quantum efficiency  $\eta$  is the ratio between the flux of generated electron-hole pairs that contributes to the detector current and the flux of incident photons. The quantum efficiency can be written in its simplest form as [8]

$$\eta = (1 - r)\xi \left(1 - e^{(-\alpha(\lambda)W_{\text{abs}})}\right) \quad (2.6)$$

with  $r$  being the optical power reflectivity of the surface,  $\xi$  the fraction of the generated electron-hole pairs that contribute to the photo current,  $\alpha(\lambda)$  the wavelength dependent absorption coefficient of the material and  $W_{\text{abs}}$  the distance the light travels through the absorptive material.

The responsivity  $R$  (in A/w) relates the incoming optical power with the resulting photo current [8].

$$R = \frac{M\eta q}{h\nu} = \frac{i_p}{P_{\text{in}}} \quad (2.7)$$

with  $M$  being the multiplication gain,  $P_{\text{in}}$  the optical input power and  $\nu$  the frequency of the incoming light.

## 2.6.2 Dark and Photo Current

The current vs. voltage and capacitance vs. voltage characteristics for a SACM APD are shown in Fig. 2.5(a). The total current can be written as

$$i = M(i_{\text{dm}} + i_{\text{p}}) + i_{\text{du}}. \quad (2.8)$$

$M$  is the multiplication gain,  $i_{\text{dm}}$  is the multiplied dark current,  $i_{\text{p}}$  is the photo current and  $i_{\text{du}}$  is the unmultiplied dark current. Dark current is a leakage current which is independent of the amount of illumination. The measurement of responsivity vs. lateral position in the APD in Fig. 2.5(b) [30] shows that multiplication gain is homogenous within the center of the device and drops towards zero at the device boundary. Therefore, this quantity should be

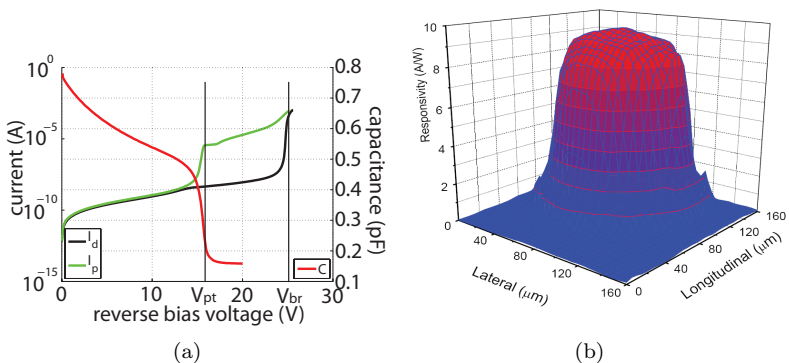


Figure 2.5: SACM APD (a) current vs. voltage and capacitance vs. voltage characteristic, (b) responsivity along the active device diameter [30].

minimized. Three main mechanisms lead to reverse bias dark current: diffusion, generation-recombination and band-to-band tunneling [31]. In general, the dark current increases for higher temperature. Its

temperature and bias voltage dependence allows to identify its origin to a certain extent.

### Diffusion

The dark current due to diffusion results from thermally generated minority carriers diffusing into the depletion region and traveling towards the opposite side. The dark current contribution can be written as [31]

$$i_d = i_s \left( e^{\left(\frac{qV}{kT}\right)} - 1 \right) \quad (2.9)$$

with  $V$  the applied reverse bias voltage. The saturation current  $i_s$  is given by [31]

$$i_s = qn_i^2 A \left( \sqrt{\frac{D_n}{\tau_n}} \frac{1}{N_a} + \sqrt{\frac{D_p}{\tau_p}} \frac{1}{N_d} \right) \quad (2.10)$$

with the intrinsic carrier concentration  $n_i$ ,  $D_n$  and  $D_p$  being the minority carrier diffusion constants,  $\tau_n$  and  $\tau_p$  being the minority carrier diffusion lifetime.

### Generation-Recombination

Dark current due to generation-recombination in the depletion region can be written as [31]

$$i_{gr} = \frac{qn_i AW}{\tau_{eff}} \left( e^{\left(\frac{qV}{2kT}\right)} - 1 \right) \quad (2.11)$$

with the thickness  $W$  of the depletion layer,  $\tau_{eff}$  is the effective carrier lifetime and  $V$  the reverse bias voltage. At increased reverse bias voltage, the dark current due to generation-recombination is proportional to  $n_i \propto \exp(-E_g/2kT)$  which dominates with its temperature dependence.

### Tunneling

Band-to-band tunneling arises in presence of high electric fields and low band gap material. The tunneling current can be expressed as [31]

$$i_t = \gamma A e \left( -\frac{\Theta m_0^{\frac{1}{2}} E_g^{\frac{3}{2}}}{q \hbar E_m} \right) \quad (2.12)$$

with  $A$  the area of the device,  $\Theta$  a model parameter ( $\Theta = 0.3$  for InGaAs [31]),  $E_m$  is the maximal electric field. The pre-factor  $\gamma$  is given by [31]

$$\gamma = \left( \frac{2m^*}{E_g} \right)^{\frac{1}{2}} \left( \frac{q^3 E_m V}{4\pi^2 \hbar^2} \right). \quad (2.13)$$

The implication of band-to-band tunneling on the design of the APD are discussed in Sec. 2.6.5.

### 2.6.3 Punch-Through Voltage

At zero applied bias the depletion region is formed within the multiplication layer (#5), parts of the n-type buffer (#4) and the p-type field control layer (#6) (see Fig. 2.6). Increasing the reverse bias voltage, the depletion region grows mainly in direction of the field control layer (#6) due to the significantly higher doping on the n-side (#4). The expansion of depletion layer results in a decrease of the device capacitance (see Fig. 2.5(a)). The slope of the CV-characteristics gives a direct indication of the field control layer doping concentration.

Once the boundary of the depletion layer reaches the low doped grading (#7) and absorber region (#8), it expands rapidly for only a small voltage change. This condition is called punch-through and the corresponding bias voltage is called punch-through voltage  $V_{pt}$ . At punch-through the corresponding capacitance drops sharply. The dark current increases due to the wider depletion region as well as higher generation-recombination in the low band gap absorber material. After punch-through the photo current sets in. Photo generated carriers are swept out of the absorption layer and will now reach the n- and p-side of the depletion layer before they recombine. Above punch-through the maximal unmultiplied responsivity  $R_u = R/M$  is achieved.

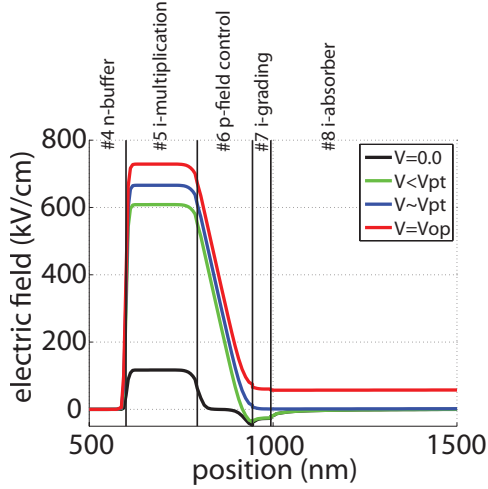


Figure 2.6: Electric field profile for various reverse bias voltages in a SACM APD

## 2.6.4 Avalanche Breakdown Voltage

At high reverse bias, avalanche breakdown can be observed by a sudden increase of the dark and photo current (see Fig. 2.5(a)). At avalanche breakdown, the number of impact ionization events increases dramatically and the multiplication gain  $M$  goes towards infinity. The corresponding voltage is called breakdown voltage  $V_{br}$ . If the final current is not limited by the external circuit thermal destruction of the device will occur.

The impact ionization rate decreases for higher temperature due to enhanced phonon scattering (see Sec. 2.2). The lower impact ionization rate leads to a larger  $V_{br}$ . The linear relationship between breakdown voltage and temperature is described by the parameter [32]

$$\rho = \frac{\Delta V_{br}}{\Delta T}. \quad (2.14)$$

Robust operation over a large temperature range asks for a small  $\rho$ . The value of  $\rho$  strongly depends on the material, e.g. InAlAs shows a smaller  $\rho$  than InP [32].

Thin multiplication layers show a significantly smaller temperature dependence [9, 32] which is an effect of non-local impact ionization. In thin layers a significantly higher electric field is required to cause avalanche breakdown. This reduces the impact ionization dead-space as shown in Sec. 2.3. The carriers achieve the threshold energy faster and scatter with fewer phonons in between impact ionization events. Hence, the increased phonon scattering rate at elevated temperature has a smaller impact in thin multiplication regions [9]. A typical value of  $\rho$  for a 200 nm thick InAlAs multiplication layer is approximately 21 mV/K [26] to 25 mV/K [33], for a 130 nm thick multiplication region  $\rho = 15$  mV/K [16].

### 2.6.5 Field Control Layer

Fig. 2.6 illustrates the functional principle of the field control layer (#6). The drop of the electric field from the left to the right side of the field control layer remains constant after punch-through. The field separation is enhanced for increased layer doping and thickness. The field separation should be small enough

- to guarantee  $V_{\text{pt}} < V_{\text{br}}$ . Furthermore, it is desirable to have a significant  $\Delta V = V_{\text{br}} - V_{\text{pt}}$  as safety margin for process variations or temperature fluctuations and to offer an increased operation range with various multiplication gains,
- to provide an electric field larger than 50 – 100 kV/cm in the InGaAs absorber. Electrons and holes should travel with their saturation velocity.

The field separation should be large enough

- to prevent band-to-band tunneling in the grading (#7) and absorber layer (#8) layer which becomes the dominant dark current mechanism for an electric field of approximately 180 kV/cm,
- to avoid impact ionization in the absorber layer which may strongly reduce device bandwidth [34],
- to reduce the breakdown voltage  $V_{\text{br}}$ . A small  $V_{\text{br}}$  lowers the power consumption of the detector and simplifies the biasing of the APD.

$V_{pt}$  and in particular  $V_{br}$  are very sensitive to doping and thickness variations of the field control layer. In combination with the non-local nature of impact ionization in thin multiplication layers, the predictive design of SACM APDs is challenging and requires sophisticated simulation tools.

## 2.7 Sensitivity

Receiver sensitivity is the minimum number of photons or optical energy required to achieve a predefined signal-to-noise ratio (SNR) or a predefined bit-error-rate (BER) for a given data rate [8]. The SNR of a detected current signal is  $SNR = \bar{i}^2/\sigma_i^2$ , with  $\bar{i}$  the mean signal current and  $\sigma_i^2$  the statistical variance of that current. The BER stands for the probability of erroneous detection of a bit which occurs if the electrical decision circuit can not distinguish between a "0" and a "1". This may happen if the SNR is too low or if the data rate is too high.

### 2.7.1 Excess Noise Factor

The randomness of the optical absorption process gives rise to photoelectron noise. The mean value of the photoelectron flux is equal to  $\bar{m} = \eta\phi$  with  $\eta$  being the quantum efficiency and  $\phi = P_{in}/h\nu$  the mean photon flux for an optical input power  $P_{in}$ . The corresponding SNR is  $SNR = \eta\bar{n}$  with  $\bar{n} = \phi T$  the mean number of photons arriving in a time interval  $T$  at the receiver [8]. The photo current noise which is created by random absorption position and time is associated to shot noise [3].

In APDs the photo current is amplified by avalanche multiplication. This introduces an additional noise component due to the randomness of the impact ionization events in position and time. The SNR of the photo current in presence of mean multiplication gain  $\bar{M}$  is [8]

$$SNR = \frac{\eta\phi}{2B} \frac{1}{F} \quad (2.15)$$

with the bandwidth of the receiver  $B$ .  $F$  is the excess noise factor which can be expressed according to local impact ionization theory [8, 35]

$$F(\bar{M}) = \frac{\langle M^2 \rangle}{\langle M \rangle^2} = k\bar{M} + (1 - k) \left( 2 - \frac{1}{\bar{M}} \right) \quad (2.16)$$

with  $k$  being the  $k$ -ratio of the avalanche multiplication process.  $F$  increases for larger  $k$ -ratio as well as for higher mean multiplication gain  $\bar{M}$  (see Fig. 2.7). In presence of avalanche multiplication, the SNR of the photo current is always decreasing.  $F$  is  $\geq 1$ , even for the ideal case of  $k = 0$ .

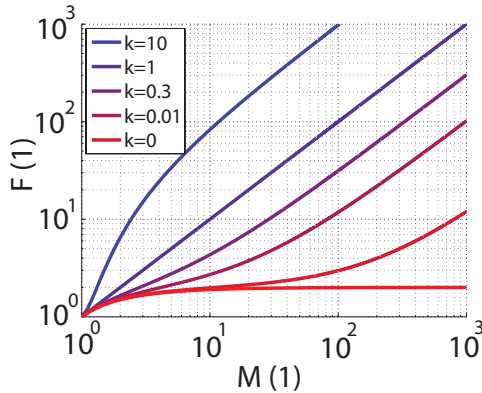


Figure 2.7: Theoretical excess noise factor for various  $k$ -ratio.

## 2.7.2 Optimal Operation Point

An optimal operation point in terms of multiplication gain exists for which the sensitivity of the APD receiver is maximized in a given configuration [36]. In this section we will shortly explain the reason for this optimal operation point.

Beside the multiplication excess noise, additional noise arises from the electronic receiver circuit including parasitics of the detector. For this simplified analysis it is convenient to combine all electric noise sources and to define the circuit noise parameter [8]  $\sigma_q = \sigma_r/2Bq$

with  $\sigma_r$  the root-mean-square (rms) value of the combined electric noise current source. The circuit noise parameter represents the rms number of circuit-noise electrons collected in the time  $T$ . In a first approximation, the total SNR of the detector and circuit can be expressed by [8]

$$\text{SNR} = \frac{\bar{M}^2 \bar{m}^2}{\bar{M}^2 F \bar{m} + \sigma_q^2}. \quad (2.17)$$

Solving above equation for the optical input power  $P_0$ , we can derive a theoretical estimation of the receiver sensitivity in terms of a predefined minimal  $\text{SNR}_0$  which we want to achieve

$$P_0 = \frac{2Bh\nu}{\eta} \frac{\text{SNR}_0 \bar{M}^2 F + \sqrt{\text{SNR}_0^2 \bar{M}^4 F^2 + 4\sigma_q^2 \bar{M}^2 \text{SNR}_0}}{2\bar{M}^2}. \quad (2.18)$$

Fig. 2.8 shows  $P_0$  vs. multiplication gain for a bandwidth  $B = 10$  GHz and for an  $\text{SNR}_0 = 100$ . Three devices with a  $k = 1.0$ ,  $k = 0.3$  and  $k = 0.0$  are compared for two circuit noise currents with  $\sigma_r = 100$  nA and  $\sigma_r = 500$  nA. We assume a wavelength of  $\lambda = 1550$  nm and

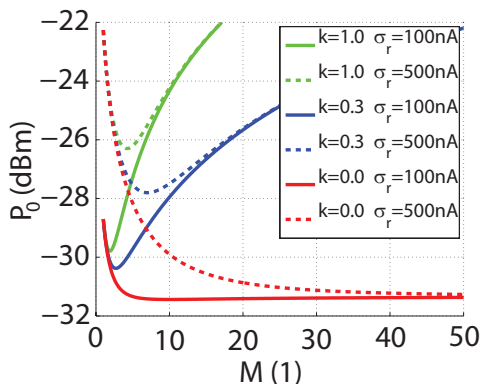


Figure 2.8: Theoretical sensitivity vs multiplication gain.

a responsivity at this wavelength of  $R = 0.88$ . The sensitivity for unity gain corresponds to the case of a PIN diode. For increasing multiplication gain, the sensitivity improves until an optimum

is reached. A lower  $k$ -value results in a better optimal sensitivity. For higher multiplication gain the sensitivity deteriorates due to increased multiplication excess noise.

## 2.8 Device Bandwidth

In general, the avalanche photodiode has a low pass characteristic. The term bandwidth is associated to two kind of measures in photodetectors, the electric  $-3$  dBe bandwidth and the optical bandwidth  $-3$  dBo.

The  $-3$  dBe bandwidth corresponds to the frequency for which the detector output power falls to  $1/2$  of its DC value. The output power  $P_{\text{out}}$  is related to the responsivity  $R$  by

$$P_{\text{out}} = R_L I_{\text{out}}^2 = R_L (RP_{\text{in}})^2. \quad (2.19)$$

The  $-3$  dBe bandwidth corresponds to the frequency for which the responsivity  $R$  falls to  $1/\sqrt{2}$  of its DC value

$$R_{f_{3\text{dBe},A/W}} = \frac{1}{\sqrt{2}} R_{\text{DC},A/W} \quad (2.20)$$

with  $R_{\text{DC}}$  being the responsivity at DC in A/w. The responsivity in dB is given by

$$R_{\text{dB}} = 20 \log_{10} \frac{R_{A/W}}{1 A/W}. \quad (2.21)$$

This means that Eq. 2.21 corresponds in dB to

$$R_{f_{3\text{dBe},\text{dB}}} = R_{\text{DC},\text{dB}} - 3 \text{ dB}. \quad (2.22)$$

The  $-3$  dBo optical bandwidth corresponds to the frequency for which the detector output voltage or current falls to  $1/2$  of its DC value. This definition is popular for the determination of the maximal data rate an optical detector can be operated [37]. The output current is related to the responsivity by

$$I_{\text{out}} = RP_{\text{in}}. \quad (2.23)$$

Therefore, the  $-3$  dBo bandwidth corresponds to the frequency for which responsivity  $R$  falls to  $1/2$  of its DC value. In terms of dB this corresponds to

$$R_{f_{3\text{dBo,dB}}} = R_{\text{DC,dB}} - 6 \text{ dB}. \quad (2.24)$$

The  $-3$  dBo bandwidth corresponds to the  $-6$  dBe bandwidth.

## 2.9 Transient Characteristics

An estimation of the signal rise time is possible by combining individual rise times of each layer in a SACM APD. This is valid if the rise time of one layer is independent of each other layer and all layers can be modeled as subsequent stages in a signal path. If no signal overshoot occurs, the total rise time is given by [38]

$$t_{\text{tot}} = \sqrt{t_1^2 + t_2^2 + \dots + t_N^2} \quad (2.25)$$

with  $t_n$  being the rise time for each individual layer. The rise time  $t_n$  is related to the time constant  $\tau_n$  by [36]  $t_n = \ln(9)\tau_n = 2.2\tau_n$  which results from the definition of the rise time being the time between 0.1 and 0.9 of the maximal signal amplitude. In terms of  $-3$  dBe bandwidth, the above formalism results in [3, 36]

$$\frac{1}{f_{3\text{dBe}}^2} = \frac{1}{f_1^2} + \frac{1}{f_2^2} + \dots + \frac{1}{f_N^2} \quad (2.26)$$

whereas  $f_n$  are the individual  $-3$  dBe bandwidths. By formulating time constants for each subsequent transport mechanism, a first estimation of the total  $-3$  dBe bandwidth and comparison of the impact of various bandwidth limiting effects becomes possible [39].

### 2.9.1 RC-Limitation

The RC-limited bandwidth is given by

$$f_{\text{RC}} = \frac{1}{2\pi\tau_{\text{RC}}} \quad (2.27)$$

with  $\tau_{\text{RC}}$  being the RC-time constant.  $\tau_{\text{RC}}$  includes electrical bandwidth limitations due to resistance and capacitance of the APD as

well as all parasitics resulting from contact, bonding wires and packaging. Fig. 2.9 shows a simplified equivalent circuit of an avalanche photodiode [3].

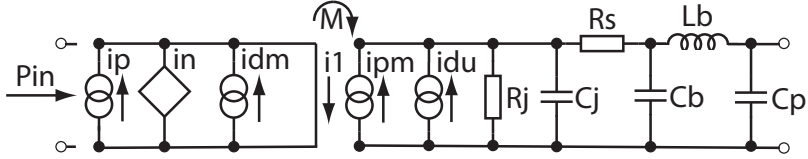


Figure 2.9: Equivalent circuit for an APD [3].

The multiplied current  $i_{pm}$  includes the initial photocurrent  $i_p$  as well as the multiplied portion of the dark current  $i_{dm}$ . The unmultiplied dark current  $i_{du}$  is added to the total current.  $R_j$  is the junction resistance.  $C_j$  is the junction capacitance which mainly depends on the total area of the device and the width of the depletion layer.  $R_s$  is the series resistance, mainly of APD p- and n-buffer regions and the contacts.  $C_b$  is the parasitic capacitance of the contacts and the bonding pad.  $L_b$  and  $C_p$  are the inductance and the capacitance of a possible bonding wire and the capacitance of the packaging. The parasitics can be estimated by separate measurements and by S11 measurements of the APD device (see Sec. 4.3.2).

## 2.9.2 Dielectric Relaxation Time

Photo generated carriers leaving the depletion region, electrons leaving on the n-side and holes leaving on the p-side, represent a space charge disturbing the neutrality of the highly doped buffer region. The time constant for the decay of this space charge is called dielectric relaxation time [17, 40]

$$\tau_r = \frac{\epsilon_s}{\sigma} \quad (2.28)$$

with  $\epsilon_s$  being the dielectric constant of the material and  $\sigma$  the conductivity of the material. In general, the dielectric relaxation time constant is in orders of a few tens of fs. Therefore, it can most often be neglected.

### 2.9.3 Transit Time Limitation

A major design trade-off in APDs is between responsivity and response speed. Most telecommunication APDs rely on depleted absorbers. Carriers generated within the depletion region are swiftly transported towards the boundary of the depletion region. Carriers generated outside the depletion region diffuse into the depletion region or into the contact which is in most cases a rather slow process. Furthermore, these carriers may recombine within the diffusion length before they reach the depletion region. The requirements on responsivity result in a rather thick absorption regions and hence to thick depletion layers which results in long transit times of the carriers.

Primary electron-hole pairs generated in the absorber region drift towards the n- and p-side, respectively (see Fig. 2.4(b)). In the low gain regime, the bandwidth of the device is limited by the transit time of the carriers traveling through the depletion layer [41] (see Fig. 2.11(a)). In particular, the secondary holes generated in the multiplication region dominate the total transit time [34]. Once the electrons and holes enter their respective majority region, they relax very fast by means of dielectric relaxation. An estimate for the time constant related to the drift of the carrier through a depleted layer is given by [17, 36]

$$\tau_d = \frac{d}{v_s} \quad (2.29)$$

with  $d$  being the thickness of the layer and  $v_s$  the saturation velocity of the carrier in this corresponding layer.

### Transit Time Reduction

There are several ways to deal with the trade-off between responsivity and response speed. First, reducing the thickness of the device and improving responsivity by means of optics. For example, it is possible to use front side metallization as a mirror and therefore double the effective length of the absorber region [42, 43]. More complex approaches use resonant cavity structures to allow the light to pass several times through the absorber. Structures with only 60 nm of absorber layer thickness can achieve an external quantum efficiency of up to 70 % at selective wavelengths and a transit time limited bandwidth of 20 GHz

[44]. Another method is to use a waveguide structure where the light passes perpendicular to the current flow [45, 46].

### Unipolar-Carrier-Transport

The concept of unipolar-carrier-transport (UTC) PIN-diodes [47] can be adopted for APDs as well. This is known under the name of un-depleted absorber [45] or neutral absorber (NA) [43, 46]. The goal of this approach is to significantly reduce the transit time of the carriers, in particular secondary holes and nevertheless provide a high responsivity. In NA SACM APDs the absorber is in general p-doped. Photo-generated electrons diffuse towards the n-side and enter the depletion layer while the majority holes relax within the dielectric relaxation time. A graded doping profile may provide an additional quasi-electric field to accelerate the electron transport through this structure. On the p-side of the absorber typically a diffusion barrier is incorporated to prevent diffusion of electrons in that direction. Due to an extraordinary mobility of electrons in p-type InGaAs ( $\mu_e = 2.9 \cdot 10^3 \text{ cm}^2/\text{Vs}$  in p-doped  $9 \cdot 10^{18} \text{ 1/cm}^3$  [48]), the diffusion length is quite large. In the absence of a quasi-electric field, the time constant for electron transport in the high doped absorber can be estimated by [49]

$$\tau_a = \left( \frac{W_a^2}{2D_e} + \frac{W_a}{v_{th}} \right) \quad (2.30)$$

with  $W_a$  being the absorber layer thickness,  $D_e$  the electron diffusion constant,  $v_{th} = 2.5 \cdot 10^7 \text{ cm/s}$  [49] being the thermionic emission velocity for electrons.

NA SACM APDs can achieve a maximal bandwidth of 20 GHz, a gain-bandwidth product of 160 GHz for an external quantum efficiency of approximately 23% using a 450 nm thick gradually doped absorber [45]. Applying a waveguide structure, a maximal bandwidth of 36.5 GHz and a gain-bandwidth product of 170 GHz is presented by [46]. In [43] a maximal bandwidth of 30 GHz is achieved, with a gain-bandwidth product of 140 GHz (InP multiplication layer) and a responsivity of  $0.71 \text{ A/w}$  using the top metallization as an optical mirror.

### Hetero-Interface Trapping

Abrupt hetero-junctions can lead to slow tails in the step response of photodiodes due to charge pile-up at the hetero-junction discontinuity [50]. These carriers remain at the hetero-junction barrier until they recombine or are thermionically emitted. A graded hetero-interface as shown in Fig. 2.10 can strongly improve the transient response [34].

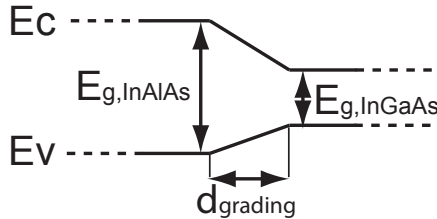


Figure 2.10: Typical grading layer between InAlAs and InGaAs. The transition layer consists of linearly graded, InP lattice matched  $\text{In}_{1-x-y}\text{Al}_x\text{Ga}_y\text{As}$ . A typical grading distance is 50 nm [34].

### 2.9.4 Avalanche Build-Up Time

Electrons entering the multiplication region will initiate a chain of impact ionization events as illustrated in Fig. 2.11(b). Initial as well as secondary electrons created by impact ionization travel towards the n-side of the depletion region. The secondary holes created by impact ionization travel towards the p-side. The subsequent generation of new electron-hole pairs results in a time delay. The avalanche build-up time constant associated with this process dominates the bandwidth in the higher gain regime (see Fig. 2.11(a)). An approximation for the avalanche build-up time constant for a local impact ionization theory is given by [51]

$$\tau_m = N(k)Mk \frac{d_{\text{mult}}}{v_{\text{mult}}}. \quad (2.31)$$

$d_{\text{mult}}$  is the thickness of the multiplication region and  $v_{\text{mult}}$  the mean carrier velocity (electron and hole combined) in the multiplication region.  $N(k)$  is a parameter which depends on  $k$  and has been extracted for local impact ionization theory [51].

In a first approximation, the avalanche time constant increases linearly with the multiplication gain  $M$ . This linear relationship defines the so called gain-bandwidth (GB) product which is illustrated in Fig. 2.11(a) by the dashed line in the avalanche build-up time regime.  $\tau_m$  is proportional to the  $k$ -ratio. Therefore, the  $k$ -ratio should be as small as possible to improve the GB-product.

It should be noted that unintentional impact ionization outside the multiplication layer is particularly detrimental to the bandwidth of the device [34].

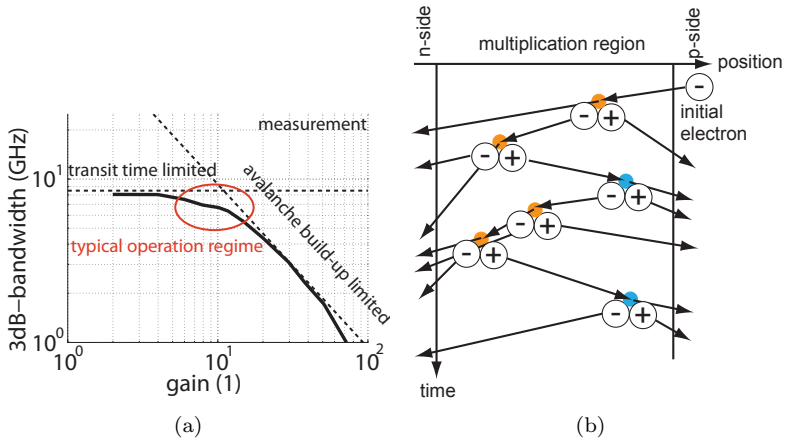


Figure 2.11: SACM APD (a) bandwidth vs. gain characteristic, (b) schematic of avalanche multiplication for an electron multiplication gain  $M_e = 13$ . Orange stands for electron initiated impact ionization events. Blue stands for hole initiated impact ionization events.

## 2.10 k-Ratio Improvement

In Sec. 2.7 and Sec. 2.9.4 it has been shown that a low  $k$ -ratio is beneficial for a high sensitivity and a high GB-product. The  $k$ -ratio can be changed by choosing an appropriate multiplication layer material, as discussed in Sec. 2.4.2. However, in this section we will discuss the possibilities to alter the effective  $k$ -ratio by properly engineering of the multiplication region.

### 2.10.1 Multiplication Layer Thickness

Reducing the thickness of the multiplication layer results in a smaller effective  $k$ -ratio [52]. Thin multiplication regions require a higher electric field to achieve the same multiplication gain compared to thick multiplication regions. According to non-local impact ionization theory (see Sec. 2.3), the higher field results in a narrower pdf. The positions of the impact ionization events are more deterministic. This results in a smaller fluctuation of the gain and a lower excess noise factor  $F(\bar{M})$ . Therefore, the effective  $k$ -ratio in Eq. 2.16 from the local theory decreases for thinner multiplication regions compared to the bulk value.

A 200 nm thick InAlAs layer provides a  $k$ -ratio of approximately  $\beta/\alpha = 0.18$  [44], 150 nm results in  $\beta/\alpha = 0.15$  [45, 53]. For comparison, the bulk  $k$ -ratio of InAlAs is  $\beta/\alpha = 0.29 - 0.5$  [18]. For a thickness of 100 nm [54], dark current due to band-to-band tunneling in the InAlAs multiplication layer starts to be significant. Therefore, a further reduction of the multiplication layer width would not be beneficial.

A low  $k$ -ratio can also be achieved for very thick multiplication regions ( $> 2 \mu\text{m}$ ) [55]. For the same multiplication gain a significantly smaller electric field is required. At low electric field the bulk  $k$ -ratio becomes small. However, this approach is not suited for high speed devices due to the long transit time in thick multiplication regions.

### 2.10.2 Band Gap Engineering

The layer structure can be a complex pattern of several materials. Engineered band diagrams in the multiplication region such as shown

in Fig. 2.12 are designed to increase electron-induced impact ionization in favor of hole-induced impact ionization [56–58]. An engineered InGaAlAs/InAlAs multiplication layer can achieve  $\beta/\alpha = 0.1$  [58].

Due to modifications of the band diagram, the electrons and holes are accelerated and decelerated differently which alters their mean distance between impact ionization events individually. Furthermore, due to the sudden steps in the band diagram, carriers abruptly increase their kinetic energy. This can result in a locally enhanced number of impact ionization events. The position of the impact ionization event is more deterministic which results in a lower excess noise factor  $F$  and a lower effective  $k$ -ratio.

In so called superlattice structures different materials are alternated periodically to achieve the same effect. Fig. 2.13 shows two possible superlattice structures. One is based on an abrupt hetero-junction with an effective  $\beta/\alpha = 0.25$  [42] while the other counts on graded hetero-interfaces with  $\beta/\alpha = 0.1 - 0.3$  [59, 60].

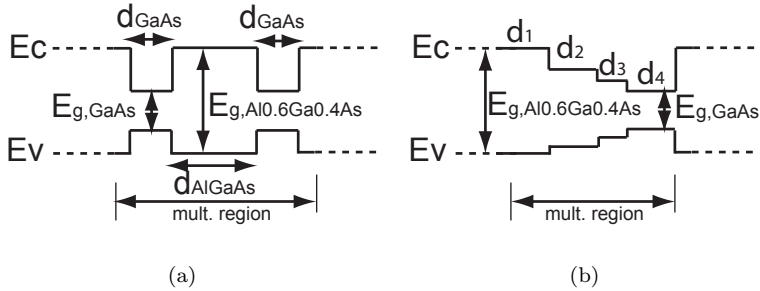


Figure 2.12: Engineered multiplication layer (a) featuring two GaAs wells with  $d_{\text{GaAs}} = 35 - 50$  nm where the majority of the impact ionization events take place. An  $\text{Al}_{0.6}\text{Ga}_{0.4}\text{As}$  layer with  $d_{\text{InAlAs}} = 85$  nm separates those two wells [56], (b) multiplication region based on step wise change of the Al content in  $\text{Al}_x\text{Ga}_{1-x}\text{As}$ ,  $d_1 = 50$  nm,  $d_2 = 30$  nm,  $d_3 = 10$  nm,  $d_4 = 50$  nm [57].

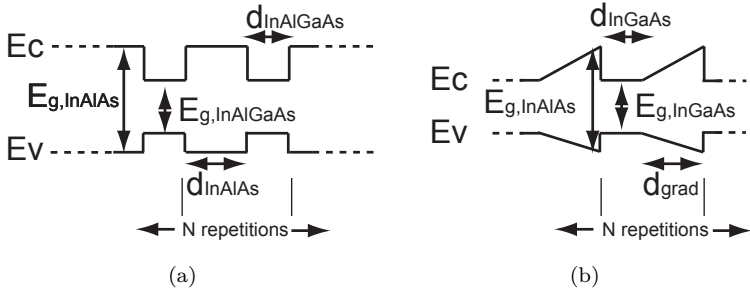


Figure 2.13: Two possible superlattice configurations (a) InAlAs/InAlGaAs superlattice structure with abrupt interfaces. Typical dimensions are 11 periods of  $d_{\text{InAlGaAs}} = 9 \text{ nm}$  and  $d_{\text{InAlAs}} = 13 \text{ nm}$  [42], (b) InAlAs/InAlGaAs superlattice structure with graded interfaces. Typical dimensions are  $d_{\text{grad}} = 20 - 100 \text{ nm}$  and  $d_{\text{InGaAs}} = 20 - 100 \text{ nm}$  [59]

# Chapter 3

## APD Design

This chapter summarizes the structure specifications of the APDs analyzed in this work. The fields of application are 10 Gbit/s FTTH and 25 Gbit/s fiber optical links. The requirements are stated in Sec. 2.1.1. The designs presented in this work focus on following aspects:

- Low  $k$ -value multiplication process for high sensitivity and high gain-bandwidth product. This is achieved by thin multiplication layers. The trade-off of thin multiplication layers is discussed in Sec. 2.10.1.
- Balancing of the trade-off between small transit time and high responsivity. This topic is discussed in Sec. 2.9.3.
- Low breakdown voltage for low power operation and simple electrical bias circuitry. The design criteria for the field control layer are discussed in Sec. 2.6.5.
- 30  $\mu\text{m}$  active diameter for cost efficient coupling to optical fibers. The large diameter results in an increased device capacitance.

### 3.1 Design of Epitaxial Structure

Five epitaxial structures have been designed. Epitaxial structure I, II, IV and V have been developed using drift-diffusion (DD) and

hydrodynamic (HD) based transport models. Not all of these designs resulted in a functional APD device (see Tab. 3.1). Epitaxial structure III has been designed using a calibrated MC simulator. Epitaxy I to IV have been grown in an MBE process while epitaxy V has been grown in an MOVPE process.

epi.	design method	fabrication method	functional APD
I	DD/HD	MBE	✓
II	DD/HD	MBE	✓
III	MC	MBE	✓
IV	DD/HD	MBE	$V_{br} < V_{pt}$
V	DD/HD	MOVPE	$i_{tunnel} \uparrow$

Table 3.1: Overview on epitaxial structure design.

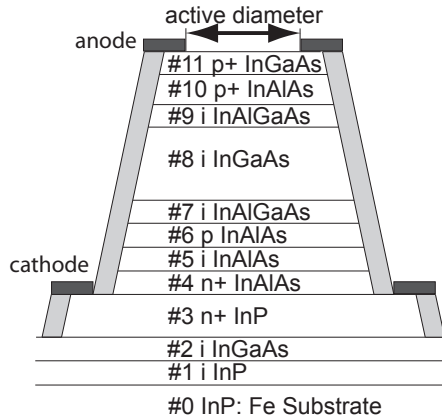


Figure 3.1: Schematic layer structure of a SACM mesa APD.

The epitaxial structures I, II and III are summarized in Tab. 3.2. A schematic of the SACM APD structures is shown in Fig. 3.1. Epitaxy I and II have a 150 nm p-type field control layer (#6) with a doping

concentration of  $2.3 \cdot 10^{17} \text{ 1/cm}^3$  and  $2.5 \cdot 10^{17} \text{ 1/cm}^3$ , respectively. Beside this difference both structures are identical. They have a 200 nm undoped InAlAs multiplication layer (#5) and a  $1 \mu\text{m}$  thick undoped InGaAs absorber layer (#8). The 50 nm thick grading layers (#7,#9) are made of intrinsic  $\text{In}_{1-x-y}\text{Al}_x\text{Ga}_y\text{As}$  with  $x = 0.25$  and  $y = 0.23$ . For further description of each layer, please refer to Tab. 2.2. Epitaxy III has a significantly thinner multiplication layer (#5) of 150 nm compared to epitaxy I and II. The idea behind this modification is the reduction of the effective  $k$ -ratio of the avalanche multiplication (see Sec. 2.10.1). The absorber layer (#8) is 550 nm thick which reduces the transit time of primary and secondary carriers (see Sec. 2.9.3).

Two additional epitaxial structures have been fabricated (see Tab. 3.3). However, they are only analyzed with respect to their current vs. voltage characteristic. Epitaxy IV is similar to epitaxy I and II. It has a significant higher field control layer (#6) doping of  $2.7 \cdot 10^{17} \text{ 1/cm}^3$  which results in  $V_{\text{pt}} \simeq V_{\text{br}}$ . Epitaxy V is fabricated using MOVPE. The fabricated structure shows a significantly smaller field control layer doping than specified. This results in a significant higher electric field in the absorber (#8) which leads to band-to-band tunneling.

## 3.2 APD Devices

Based on the presented epitaxial structures, mesa APDs are fabricated. In this work, mainly three devices are characterized: device A, B and C. Additional devices are only characterized with respect to their current vs. voltage characteristics in comparison with the previous three devices. Device B' and B'' allow to analyze the scaling of the dark current with respect to the device diameter of epitaxial structure II. Device D and E are interesting regarding the dark current activation energy due to their particular breakdown mechanics. A complete list of the devices under test (DUT) is given in Tab. 3.4. All devices with exception of device B'' are top-illuminated devices.

A schematic of the electrical contact layout is shown in Fig. 3.2. The ground-signal-ground (GSG) configuration allows for convenient connection with Cascade Microtech AP40 GSG-150 high frequency

layer	material			thickness (nm)			doping ( $1/\text{cm}^3$ )		
	I	II	III	I	II	III	I	II	III
#0	InP:Fe			$1.5 \cdot 10^5$			Fe		
#1	n-InP			100			$< 1 \cdot 10^{16}$		
#2	n-InGaAs			25			$< 1 \cdot 10^{16}$		
#3	n-InP			400			$7 \cdot 10^{18}$		
#4	n-InAlAs			200			$5 \cdot 10^{18}$		
#5	i-InAlAs			200	150		$< 1 \cdot 10^{15}$		
#6	p-InAlAs			150			$2.3 \cdot 10^{17}$	$2.5 \cdot 10^{17}$	$2.3 \cdot 10^{17}$
#7	i-InAlGaAs			50			$< 1 \cdot 10^{16}$		
#8	i-InGaAs			1000	550		$< 1 \cdot 10^{15}$		
#9	i-InAlGaAs			50			$< 1 \cdot 10^{16}$		
#10	p-InAlAs			400			$3 \cdot 10^{18}$		
#11	p-InGaAs			100			$1.4 \cdot 10^{19}$		

Table 3.2: Epitaxial structures I, II and III analyzed in this work.

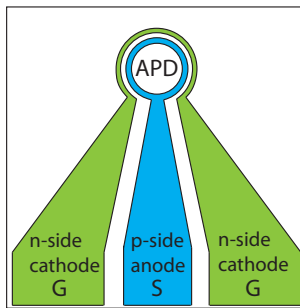


Figure 3.2: Schematic layout of electrical contact pads

probes and Cascade Microtech DCP 150R probe needles. The separated APD chips are attached to small ceramic plates using a thermally conductive glue. This makes the handling of the device on the wafer prober much easier. The ceramic plates are thin enough to avoid any

layer	material		thickness (nm)		doping ( $1/\text{cm}^3$ )	
	IV	V	IV	V	IV	V
#0	InP:Fe	InP:Fe	$1.5 \cdot 10^5$	-	Fe	-
#1	n-InP		100		$< 1 \cdot 10^{16}$	
#2	n-InGaAs		25		$< 1 \cdot 10^{16}$	
#3	n-InP		400		$7 \cdot 10^{18}$	
#4	n-InAlAs		200		$5 \cdot 10^{18}$	
#5	i-InAlAs		200		$< 1 \cdot 10^{15}$	
#6	p-InAlAs		150		$2.7 \cdot 10^{17}$	$2.3 \cdot 10^{17}$
#7	i-InAlGaAs		50		$< 1 \cdot 10^{16}$	
#8	i-InGaAs		1000		$< 1 \cdot 10^{15}$	
#9	i-InAlGaAs		50		$< 1 \cdot 10^{16}$	
#10	p-InAlAs		400		$3 \cdot 10^{18}$	
#11	p-InGaAs		100		$1.4 \cdot 10^{19}$	

Table 3.3: Epitaxial structures IV and V for current vs. voltage analysis.

significant temperature gradients between the thermochuck and APD chip. A fiber optical lens is used to improve the coupling of light into the APD structure.

device	epitaxy	type	active diameter ( $\mu\text{m}$ )	data rate (GBit/s)
A	I	top	32	10
B	II	top	32	10
C	III	top	12	25
B'	II	top	12	10
B''	II	bottom	85	2.5
D	IV	top	32	10
E	V	top	32	10

Table 3.4: APD devices analyzed in this work.

# Chapter 4

## Measurement Analysis Results

This chapter summarizes the main results of the APD device characterization and analysis.

### 4.1 Capacitance-Voltage Characteristics

The measurement of the device capacitance vs. reverse bias voltage is a major characterization tool for the quality control of the fabrication process. The CV-characteristics allow to determine layer thickness and doping concentration of the fabricated devices which may differ significantly from the specified values.

The capacitance-voltage (CV) measurements have been performed on a Agilent 4284A Precision LCR Meter at 1 MHz frequency. The setup is shown in Fig. 4.1.

The resulting capacitance for Device A, B and C are shown in Fig. 4.2. The capacitance at zero Volts, the gradient of the capacitance vs. voltage characteristic and the punch-through voltage are indications for the field control layer doping. Under the assumption that the diameter of the device and the parasitic capacitances are known, the reconstruction of the epitaxial layer structure is possible which will be discussed in Sec. 7.1.

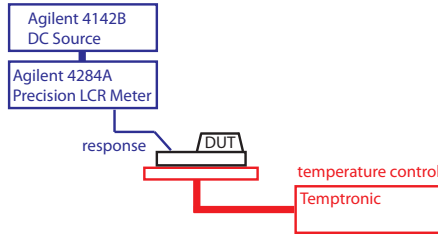


Figure 4.1: Setup for CV measurement.

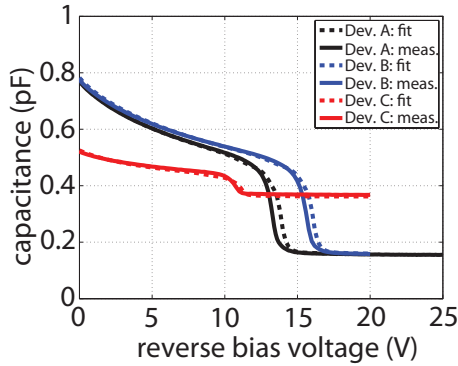


Figure 4.2: Measured CV characteristics for device A, B and C

## 4.2 Stationary VI-characteristics

### 4.2.1 Definitions

Following definitions are used:

1. The punch-through voltage  $V_{pt}$  is the voltage where the derivative of the photo current with respect to the voltage  $\partial i_p / \partial V$  is at its maximum due to the rapid depletion of the absorber region.
2. The voltage for unity gain  $V_{m1} > V_{pt}$  is the voltage where the second derivative of the photo current with respect to the voltage

$\partial^2 i_p / \partial V^2$  is zero. This reflects the assumption of a plateau with respect to the applied voltage for which the responsivity remains constant and the multiplication gain is equal to one. Impact ionization prior to punch-through, e.g. in devices with a small difference between  $V_{pt}$  and  $V_{br}$ , leads to an underestimated avalanche multiplication gain by this definition.

3. Multiplication gain for a reverse bias voltage  $V$  is defined as the ratio between the photo current measured at  $V$  and the photo current measured at  $V_{m1}$ .
4. The breakdown voltage  $V_{br}$  is the voltage where the dark current exceeds  $i_d = i_{dm} + i_{du} = 0.1$  mA. Above this voltage, the dark current is influenced by the series resistance depending on the dimension of the APD. This definition of the breakdown voltage corresponds to a multiplication gain of several thousand.

### 4.2.2 Setup

Dark current and photo current vs. voltage (VI) characteristics are measured using an Agilent 4156C precision semiconductor parameter analyzer. The setup is shown in Fig. 4.3. The APD is placed on a temperature controlled chuck of a Cascade Microtech Summit 9600 thermal probe station. The devices are protected from parasitic illumination by a metallic casing. The temperature of the chuck is controlled using a Temptronic heating element. The exact temperature in the middle of the chuck is verified to  $\pm 1\%$  of the absolute temperature using an independent DH-802C temperature sensor. The discrepancy between the temperature measured by the Temptronic thermochuck element and the independent temperature sensor is within  $\pm 1$  K after 5 min settling time. The devices are contacted using a set of Cascade Microprobe DCP 150R probe needles. For the DC optical input signal an Exalos SLED ESL1510-2100 is used, driven by a LDC-3742 laser diode controller. The optical input is damped using a JDS Fitel HA9 optical attenuator. The light is coupled into the APD device using a fiber optical lens.

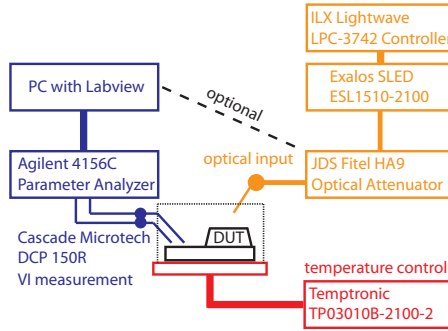


Figure 4.3: Setup for VI-measurement.

### 4.2.3 Dark Current

Dark current vs. reverse bias voltage for device A and B are shown in Fig. 4.4(a) and Fig. 4.4(b). Both devices show the typical increase of the dark current as well as an increase of the breakdown voltage for increasing temperature. The dark current increases after the punch-through, mainly due to the lower band gap of the absorber region (#8) material and the larger depletion region thickness (see Sec. 2.6.3).

The dark current in device C (see Fig. 4.4(c)) decreases compared to device A and B, mainly due to the smaller device diameter. The influence of the device diameter will be discussed in Sec. 4.2.9.

For device D,  $V_{pt}$  and  $V_{br}$  nearly coincide which is a result of a very high field control layer doping (see Fig. 4.5(a)). The resulting dark current is dominated by mechanisms in the multiplication layer (#5) and the field control layer (#6).

The field control layer (#6) doping of device E is too low. Furthermore, an evidence of significant p-type background doping in the absorber (#8) has been found. This results in a high electric field in the absorber, in particular close to the interface between absorber (#8) and grading (#7). The resulting band-to-band tunneling dominates the dark current characteristics. For increased temperature, tunneling current increases (see Fig. 4.5(b)). Applying the definition of  $V_{br}$  to such kind of devices, a reduction of the breakdown voltage

for increasing temperature would be observed. This makes it easy to distinguish tunneling breakdown from avalanche breakdown.

The dark current for device A, B and C around the typical operation point of approximately  $0.9 \cdot V_{br}$  is shown in Tab. 4.1. The dark current for all devices is below 20 nA which is good enough for most high sensitivity applications. In general, the variation between different devices of the same wafer are small in terms of dark current and breakdown voltage.

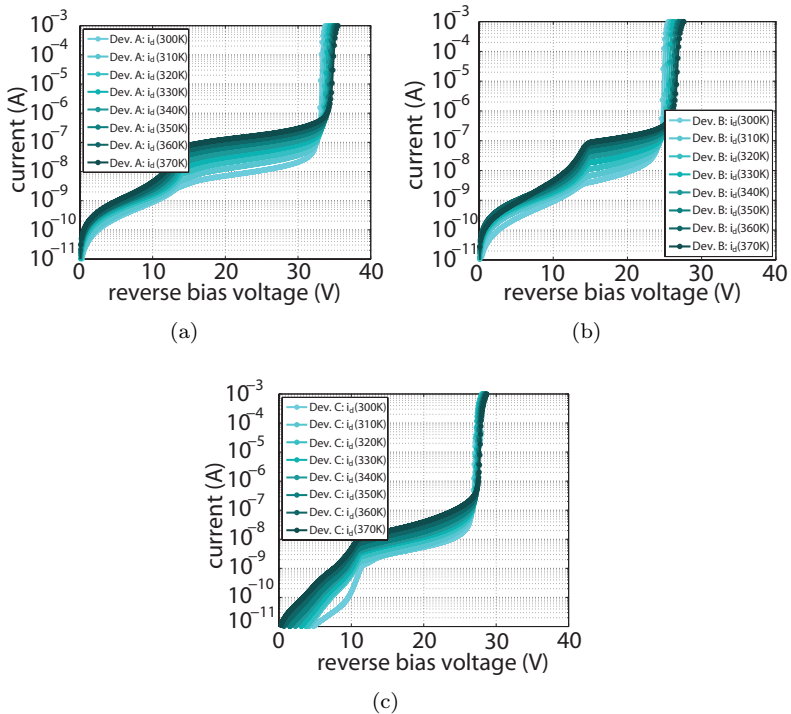


Figure 4.4: Measured dark current vs. reverse bias voltage: (a) device A, (b) device B, (c) device C

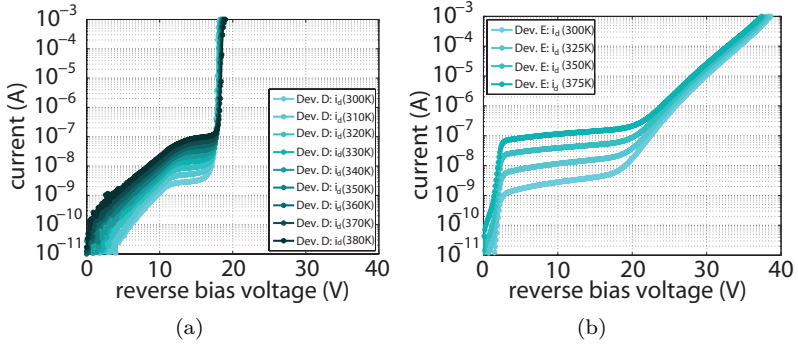


Figure 4.5: Measured dark current vs. reverse bias voltage: (a) device D, (b) device E.

device	$0.9 \cdot V_{br}$ (V)	$i_{d,op}$ (nA)
A	29.9	20.0
B	22.4	16.6
C	24.3	11.4

Table 4.1: Dark current in the typical operation regime  $i_{d,op}$  at  $0.9 \cdot V_{br}$  at 300 K.

#### 4.2.4 Photo Current

Photo current measurements for device A, B and C are shown in Fig. 4.6. In the measurement setup it is difficult to define the exact amount of optical input power which is coupled into the APD device. Therefore, the photo current value differs slightly for each measurements. Using the definition in Sec. 4.2.1 the punch-through voltage  $V_{pt}$  and the unity gain voltage  $V_{m1}$  are extracted. The corresponding values are shown in Tab. 4.2.

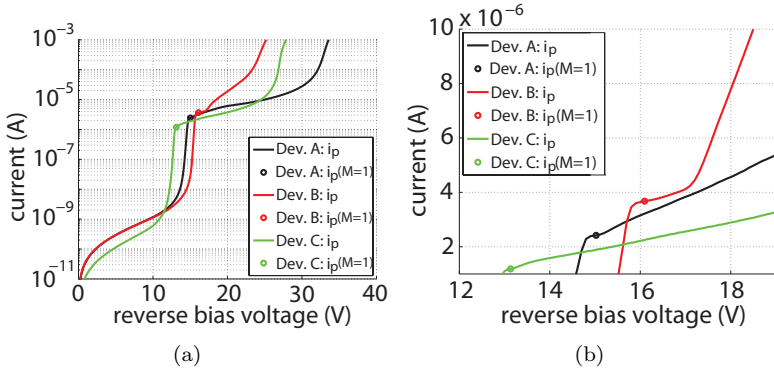


Figure 4.6: Device A, B and C: (a) photo current measurement, (b) close-up of photo current measurement around  $V_{m1}$ .

device	$V_{pt}$ (V)	$V_{m1}$ (V)
A	14.5	15.0
B	15.5	16.1
C	12.85	13.13

Table 4.2: Punch-through voltage  $V_{pt}$  and unity gain voltage  $V_{m1}$  for device A, B and C at 300 K.

## 4.2.5 Responsivity

Responsivity measurements performed by Enableness, Switzerland estimate a responsivity of approximately  $0.8 \text{ A/w}$  for device A and B. The exact calibration of the responsivity measurement is difficult. First, because the amount of light coupled into the device needs to be known. Second, it is possible that a small multiplication gain is present at punch-through which is difficult to distinguish from the responsivity increase.

### 4.2.6 Multiplication Gain

Based on the photo current measurements (cf. Sec. 4.2.4) and the definition for  $V_{m1}$  the multiplication gain for device A, B and C can be calculated (see Fig. 4.7 and Fig. 4.8).

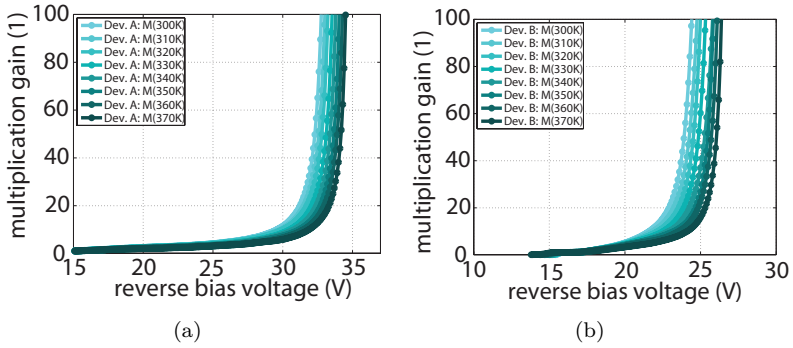


Figure 4.7: Multiplication gain for various temperatures: (a) device A, (b) device B

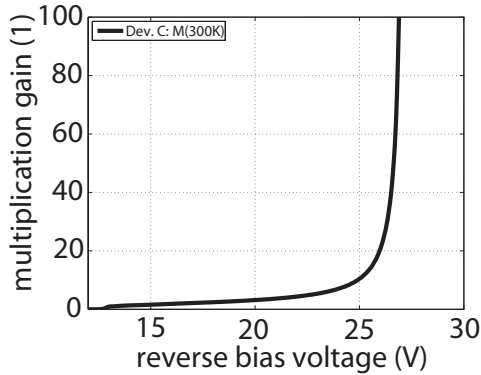


Figure 4.8: Multiplication gain of device C at 300 K

### 4.2.7 Breakdown Voltage Temperature Dependence

According to definition in Sec. 4.2.1 the temperature dependent breakdown voltage is extracted from the dark current measurements. The breakdown voltage vs. temperature is shown in Fig. 4.9. Device A and B behave as expected. The breakdown voltage is a linear function of the temperature (see Sec. 2.6.4). For device C, the points at 300 K and 320 K are outliers that do not match the linear relationship. However, control measurement on other sample show that these measurement points result from a bad contact of the probe needle with the sample.

The corresponding temperature coefficient  $\rho$  is tabulated in Tab. 4.3. The values for  $\rho$  in device A and B are close to the expected values of  $21 - 25 \text{ mV/K}$  (see Sec. 2.6.4).  $\rho$  decreases as expected for the thinner multiplication region in device C. The temperature coefficient for device C has been extracted for three different samples. The variation of the breakdown voltage is very small and the temperature coefficient  $\rho$  varies between  $12.8 \text{ mV/K}$  to  $16.8 \text{ mV/K}$ . The expected value for a slightly thinner multiplication region of  $130 \text{ nm}$  is  $\rho = 15 \text{ mV/K}$  [16] (see Sec. 2.6.4).

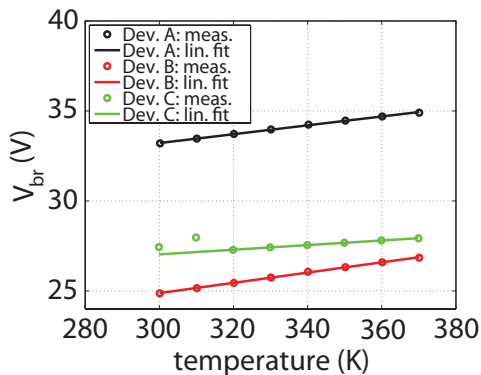


Figure 4.9:  $V_{br}$  vs. temperature.

device	#5 thickness (nm)	$V_{\text{br}}(300\text{ K})$ (V)	$\rho$ (mV/K)
A	200	33.2	24.6
B	200	24.9	28.5
C	150	27.0 / 26.93 / 26.96	12.8 / 16.8 / 14.9

Table 4.3: Temperature coefficient of  $V_{\text{br}}$ .

### 4.2.8 Dark Current Temperature Dependence

In Sec. 2.6.2 the main dark current contributions have been summarized. By investigating the temperature dependence of the dark current, we are able to understand the mechanisms causing it. The dark current vs. inverse temperature for device A at various reverse bias points is shown in Fig. 4.10. The circles represent the measurement values. The line represents a least mean square fit for a fitting function [33]

$$i_{\text{d}}(T) = i_{\text{d}0} e^{\left(\frac{-E_{\text{a}}}{kT}\right)} \quad (4.1)$$

with dark current at 300 K  $i_{\text{d}0}$  and the activation energy  $E_{\text{a}}$  being the fit parameters. The values of the dark current at any measured voltage is close to the fit. This procedure can now be applied to any DUT. The resulting activation energy vs. applied reverse bias voltage is shown in Fig. 4.11.

The increase of the depletion region width with respect to the applied voltage is slightly temperature dependent. Analyzing the activation energy for a fixed voltage does include the varying depletion layer width. This variation is rather small. But due to this mechanism, it is assumed that the activation energies in Fig. 4.11 are overestimated with respect to the underlying dark current generation mechanism.

Nevertheless, some interesting observations can be made by comparing activation energies in different regimes. For all devices the activation energy peaks at punch-through which is to some extent caused by the varying depletion region width, which results in a decrease of  $V_{\text{pt}}$  for increasing temperature. Above  $V_{\text{pt}}$  the activation energy decreases which is a result of the lower band-gap material (InGaAs) in the absorber region (#8) compared to the InAlAs of

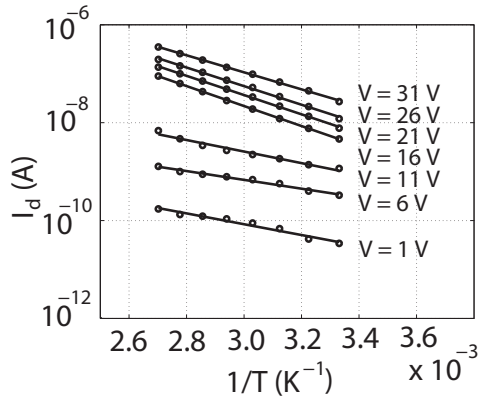


Figure 4.10: Measured dark current vs. inverse temperature.

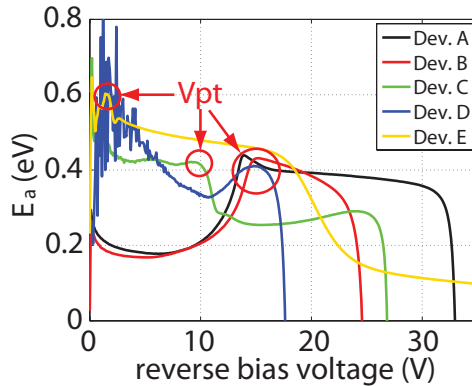


Figure 4.11: Activation energy of dark current mechanisms vs. applied reverse bias voltage.

the multiplication (#5), the field control (#6) and the InAlGaAs in the grading layer (#7). The value of the activation energy after punch-through of roughly 0.4 eV is close to half the band gap of InGaAs. This suggests that the dominating dark current mechanism in the operation regime is due to generation-recombination within the

absorber layer, in the grading layers or at the interfaces between these regions. At high reverse bias voltages the activation energy drops steeply for device A, B, C and D. In general, the dark current can be written as

$$i_d(T, V) = i_{du}(T, V) + M(T, V)i_{dm}(T, V). \quad (4.2)$$

While the dark current contribution  $i_{du}(T, V)$  and  $i_{dm}(T, V)$  for a fixed bias voltage increases for higher temperature, the multiplication gain  $M(T, V)$  decreases. Near the breakdown voltage the temperature dependence of the multiplication gain dominates which results in a very small or even negative effective activation energy. In contrast, device E does not show this distinctive behavior. The dark current in this particular device is dominated by band-to-band tunneling (see Sec. 2.6.2).

Another interesting observation is that device A and B do have a very small activation energy below punch-through while all other devices have an increased activation energy. There is no conclusive explanation for this behavior as will be pointed out in Sec. 4.2.9. Since the dark current in the operation regime is clearly dominated by generation-recombination in the low band gap absorber, the dark current caused below punch-through is negligible for the performance of the APD.

### 4.2.9 Dark Current Dependence on Diameter

The measured dark current of device B, B' and B'' vs. the estimated device radius is shown in Fig. 4.12(a). All devices are based on the same epitaxial specification but different fabrication runs. There is a small variation in  $V_{br}$ , which influence the following analysis in the high gain regime. However, in the low gain regime, multiplication gain should not significantly influence the relative relationship of the dark current between device B, B' and B''.

The dependence of the dark current vs. device radius in the low voltage regime above  $V_{pt}$  is quite linear which suggest that the dark current mechanisms are proportional to the device circumference and not to the device area. This observation leads to the conclusion that dark current in this devices is dominated by the surface between the

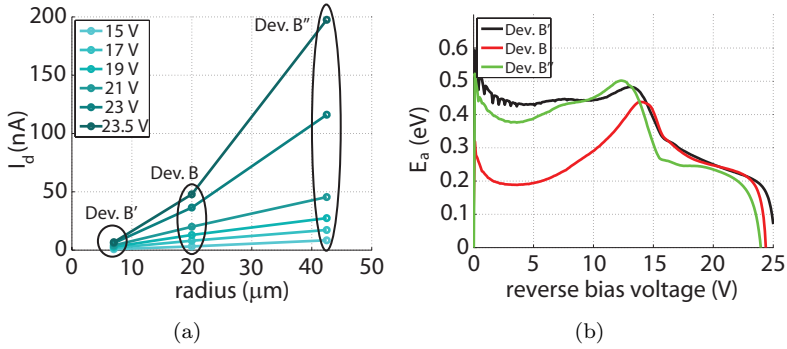


Figure 4.12: dark current analysis of device B, B' and B'': (a) dark current vs. device radius above  $V_{pt}$ , (b) activation energy of the dark current mechanism.

epitaxial structure and the passivation layer [52]. As mentioned in Sec. 4.2.8, the dark current originates in particular from within the absorber layer, the grading layer or at their interfaces, due to the observed lowering of the activation energy after  $V_{pt}$ .

At higher reverse bias voltages the linear relationship between dark current and radius goes towards a non-linear relationship which indicates an increased multiplication of bulk dark current. However, in this regime the data is compromised by varying multiplication gain due to run-to-run variation.

The activation energy vs. applied reverse bias voltage in Fig. 4.12(b) shows that device B is special compared to device B' and B''. While above punch-through the activation energy of all devices is very similar, below punch-through a significantly lower activation energy in device B can be observed. This means that the dominating dark current mechanism in device B is different. At the current state of analysis no explanation for the particularly high dark current with a low activation energy can be given.

## 4.3 Dynamic Characteristics

### 4.3.1 Frequency Domain Measurement Setup

The measurement setup for the frequency domain measurement is shown in Fig. 4.13.  $S_{11}$  and  $S_{12}$  are measured using an Agilent 86030A lightwave component analyzer (LCA). The bias voltage is applied using a Keithley 2601 source meter connected to the internal bias-T of the LCA. The source meter current compliance has been set to 1 mA to avoid damaging of the APD. It allows to sweep the bias point up to a reverse bias voltage of 40 V.

The APDs are connected by 1 m long high frequency cables and a Cascade Microprobe 150 GSG probe needle. The optical signal is fed into the APD using a fiber optic lens. The fiber provides good coupling efficiency if properly aligned. Optionally, the optical signal is attenuated using a JDS Fitel HA9 Optical Attenuator.

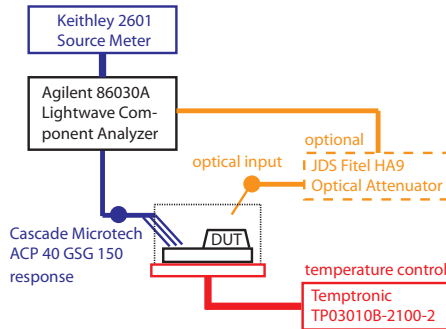


Figure 4.13: Setup for bandwidth measurement in frequency domain.

For the  $S_{11}$  measurement the setup is calibrated using a LRM ISS (GSG) PN 101190 S/N 567 impedance substrate, using a response-match calibration (short, open, load) procedure including the high frequency cable and probe needle.

For the  $S_{12}$  measurement a response-isolation calibration has been performed. The influence of the high frequency cable is taken into account for the calibration. However, the probe needle is not included

in the calibration. Mainly because no calibrated on-chip photodiode for response calibration is available. The probe needle is specified for DC to 40 GHz usage. The probe should not significantly influence the measurement in the frequency range of (0 – 15 GHz). However, mismatch ripples will occur, with which we will deal with in post-processing of the data.

### 4.3.2 S11 Results

Fig. 4.14 shows the S11 measurement result for device B at various bias voltages. The measurements are performed from 45 MHz to 50 GHz with 801 points and an averaging factor of 32. For low reverse bias voltages the capacitance of the APD is quite large, due to the thin multiplication layer thickness. As the reverse bias voltage increases, the capacitance decreases and the corresponding  $-3$  dB bandwidth increases which results as well in a shift in the Smith Chart to lower capacitance values. The characteristic is found to be nearly independent of temperature.

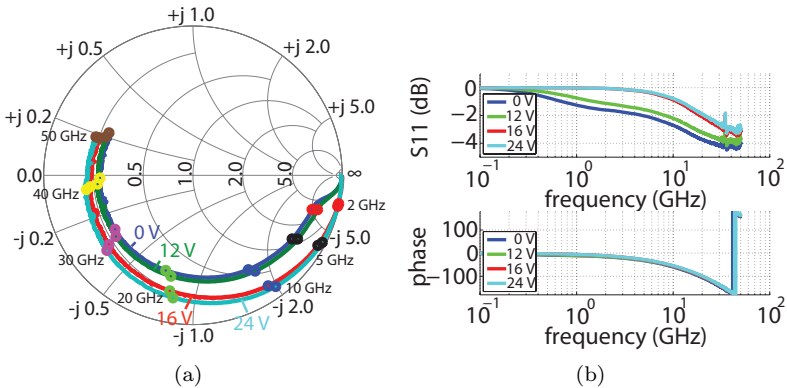


Figure 4.14: S11 measurement result of device B: (a) Smith Chart, (b) magnitude and phase.

Fig. 4.15 shows the S11 measurement results in the operation regime for device A (at 28 V), device B (at 22 V) and device C (at 22 V). The measurements are performed from 45 MHz to 50 GHz with

201 points and an averaging factor of 512. For the S11-magnitude measurement two samples of each device have been measured for two different GSG-needles of the same type and independent calibrations. As expected device A and B show nearly identical characteristics. Device C shows an unexpected drop in the S11 magnitude below 20 GHz.

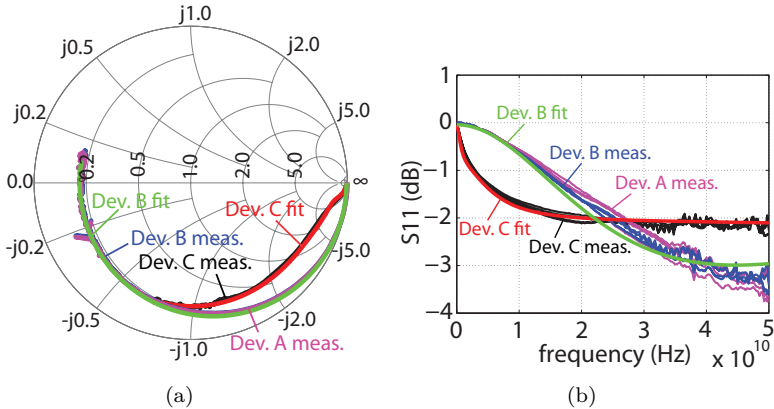


Figure 4.15: S11 measurement result and fit for device A, B and C: (a) Smith Chart, (b) magnitude with phase.

Small signal equivalent circuits for device A and B are extracted by manually fitting the circuit parameter to the measured Smith Chart characteristic (see Fig. 4.16, Sec. 2.9.1). For this purpose the Qucs circuit simulator [61] is used. One possible parameter configuration is shown in Tab. 4.4. The circuit parameter values are all within expectations.

Some irregularities in the fabrication of device C have been reported which result in a high device capacitance (see Sec. 4.1). From test structure analysis we know that a parasitic current path exists, which connects the cathode pad through the semi-conductive substrate with the anode of the diode. To estimate the impact of the substrate conductance on device performance an additional parasitic current path has been included in the small signal equivalent circuit model of device C (see Fig. 4.17). The capacitance between the

cathode pad and the substrate beneath has been estimated to be  $C_{\text{su}1} = 180 \text{ fF}$ . The capacitance between the cathode contact metallization and the substrate has been estimated to be  $C_{\text{su}2} = 100 \text{ fF}$ . The simulated S11 characteristic does fit the measured characteristic quite well, as shown in Fig. 4.15. The circuit parameter values shown in Tab. 4.4.

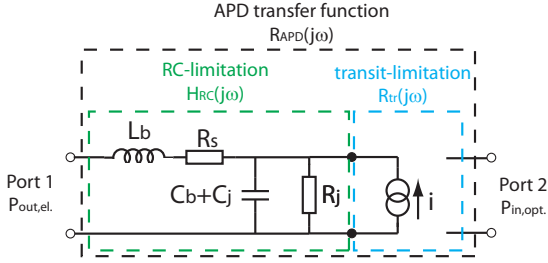


Figure 4.16: Small signal equivalent electrical circuit model for device A and B.

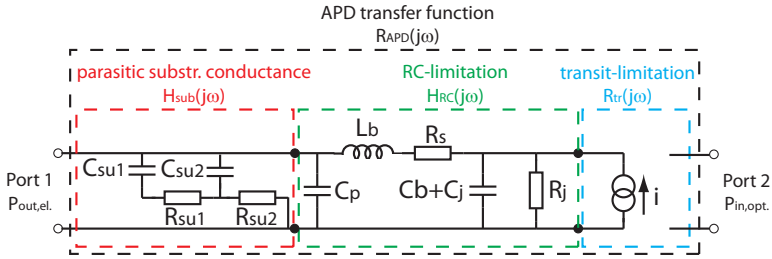


Figure 4.17: Small signal equivalent electrical circuit model for device C.

The magnitude of the transfer function  $|H_{\text{RC}}(j\omega)|$  and  $|H_{\text{sub}}(j\omega)|$  of the electrical circuit is computed using the circuit simulator by setting the transit time transfer function  $|R_{\text{tr}}(j\omega)| = 1$ . The resulting normalized electrical transfer function  $|H_{\text{RC}}(j\omega)|$  for device A and B is shown in Fig. 4.18. The  $-3 \text{ dB}$  RC-limited bandwidth is approximately  $f_{-3 \text{ dB}, \text{RC}} \simeq 20 \text{ GHz}$ . For device C, the transfer function with

parameter	device A, B	device C
$R_j$	20 k $\Omega$	20 k $\Omega$
$C_j + C_b$	157 fF	68 fF
$R_s$	8.5 $\Omega$	9 $\Omega$
$L_b$	0.08 nH	0.01 nH
$C_p$	-	15 fF
$C_{su1}$	-	180 fF
$C_{su2}$	-	100 fF
$R_{su1}$	-	0.9 k $\Omega$
$R_{su2}$	-	0.42 k $\Omega$

Table 4.4: Parameter values of small signal equivalent electrical circuit model for device B.

and without parasitic substrate conductance is presented. Without substrate conductance the bandwidth is  $f_{-3\text{ dBe,RC}} > 30$  GHz. With substrate conductance  $f_{-3\text{ dBe,RC}} \simeq 30$  GHz. However, the transferred signal power at 10 GHz is already attenuated more than  $-1$  dB. Therefore, we expect an impact on the overall APD bandwidth due to the substrate conductance.

### 4.3.3 S12 Results

The S12 results have been obtained for a frequency range of 45 MHz to 15 GHz, using 201 equidistant frequency points and an averaging factor of 512. For each device the measurement has been performed three times at various optical input power. The setup for the optical input power of the LCA laser source is shown in Tab. 4.5. Measurements #1 and #2 are performed for an identical setup but with separated calibration. Measurement #3 is performed with the same calibration as measurement #2, but the modulated laser output is damped by  $-9$  dB.

The modulator has been auto-biased to the quadrature point and the resulting power measurements are shown in Tab. 4.6. The mean optical input power  $P_{\text{out,mean}}$  has been measured in front of the fiber

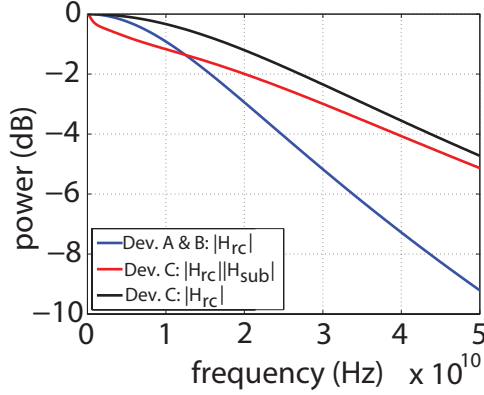


Figure 4.18: Electrical S12 characteristic extracted from electrical equivalent circuit model.

meas.	$P_{\text{out,set,laser}}$ (dBm)	attenuation (dB)
#1	-10	0
#2	-10	0
#3	-10	-9

Table 4.5: Setup for optical input signal.

optical lens. This value represents the maximal mean light power which could be coupled into the device for perfect alignment. The S12 measurement results for measurement #1 are shown in Fig. 4.19(a), Fig. 4.20(a) and Fig. 4.21(a), for device A, B and C, respectively.

As described in Sec. 4.3.1 the probe needles are not included in the calibration which leads to distinctive reflection ripples in the black measurement curves. For analysis purposes the frequency response is smoothed by a polynomial of fifth order which is illustrated by the red curves. Using this fit the major features of the frequency response are maintained for all measurements as well as for all applied bias voltages. During the measurement at the various bias points the mean optical input power remains constant which allows to extract the relative

meas.	$P_{\text{out,max,LCA}}$ (dBm)	$P_{\text{out,min,LCA}}$ (dBm)	$P_{\text{out,mean}}$ (dBm)
#1	-8.1	-22.2	-10.4
#2	-8.1	-19.4	-10.5
#3	-8.1	-19.4	-21.2

Table 4.6: Measured optical input power.  $P_{\text{out,max,LCA}}$  and  $P_{\text{out,min,LCA}}$  are internal reading of the LCA.  $P_{\text{out,mean}}$  is the mean optical power prior to the fiber optical lens. The optical power coupled into the APD can be considerable lower than this value.

multiplication gain at every bias point by the responsivity increase at 45 MHz. The gain for the lowest bias voltage is extracted from the corresponding DC gain from VI-measurement. Based on the fitted frequency characteristic the  $-3$  dB bandwidth is extracted. The resulting gain-bandwidth characteristics are shown in Fig. 4.19(b), Fig. 4.20(b) and Fig. 4.21(b), for device A, B and C respectively.

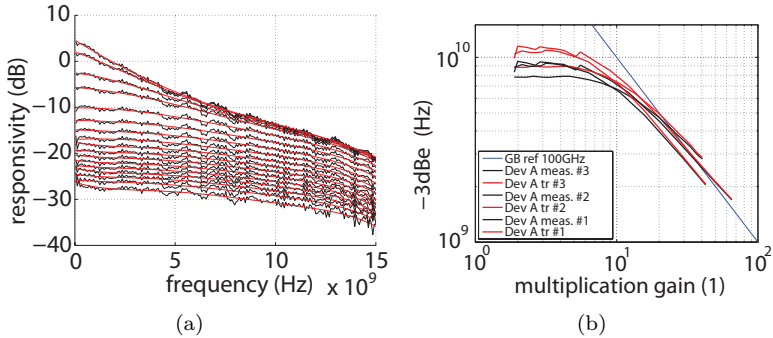


Figure 4.19: S12 measurement results: (a) frequency response at various bias voltages (black) and corresponding fit using a polynomial of fifth order (red), (b)  $-3$  dB bandwidth vs. multiplication gain.

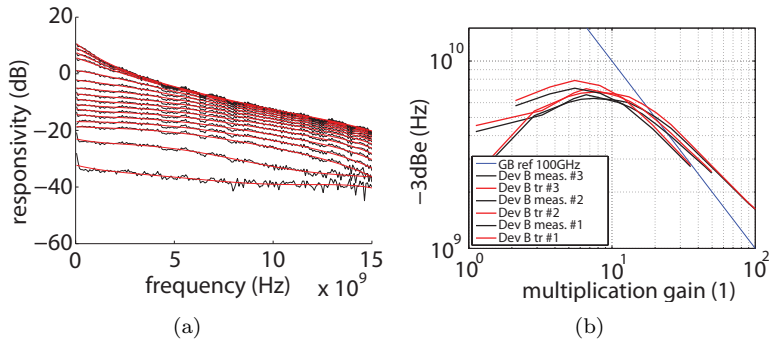


Figure 4.20: S12 measurement results: (a) frequency response at various bias voltages (black) and corresponding fit using a polynomial of fifth order (red), (b)  $-3$  dBe bandwidth vs. multiplication gain.

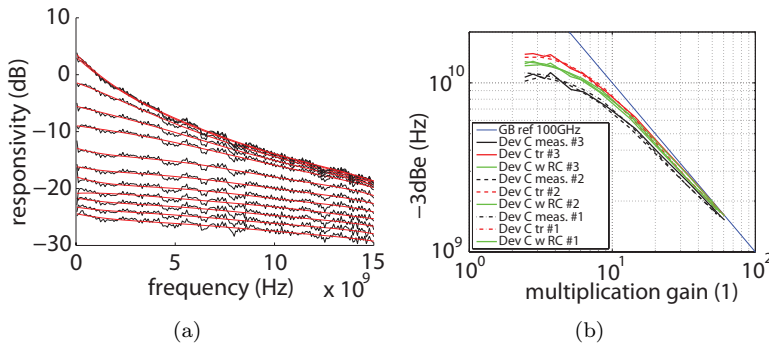


Figure 4.21: S12 measurement results: (a) frequency response at various bias voltages (black) and corresponding fit using a polynomial of fifth order (red), (b)  $-3$  dBe bandwidth vs. multiplication gain.

### Low $-3$ dBe of Device B

The maximal  $-3$  dBe bandwidth is tabulated in Tab. 4.7. It is interesting to note the significant difference of  $f_{-3\text{dBe,max}}$  between device A and B. Both devices are identical with the exception of the field control

layer (#6) doping and hence the field separation between multiplication layer (#5) and grading (#7) and absorber (#8) layer. Electrons and holes in both structures have the same traveling distance. Furthermore, the  $-3$  dBe decreases for device B at lower multiplication gain, while the bandwidth of device A is high even for low gain.

In the presence of high electric fields we can neglect the influence of the doping concentration on the saturation velocity [62] in the rather thin field control layer (#6). The RC-limitations are similar in both devices as seen in Sec. 4.3.2. Therefore, the reduction of the maximal bandwidth is either caused by avalanche multiplication or low velocity carriers. The reduction of the  $-3$  dBe bandwidth for decreasing multiplication gain is a strong argument against avalanche multiplication effects. Therefore, we contribute the reduction of the maximal bandwidth to low velocity hole transport in the absorber layer. The high field control layer (#6) doping in device B results in a significantly lower electric field in the absorber layer (#8) compared to device A. Depending on the exact electric field profile in the absorber, some holes in the absorber region of device B travel below their saturation velocity. This is consistent with a lower  $f_{-3\text{dBe,max}}$  as well as the decrease of the bandwidth for lower multiplication gain which corresponds to a lower bias voltage and hence a lower electric field. In device A the electric field in the absorber is high enough for hole transport at saturation velocity even at low multiplication gain. We will further investigate the behavior of device B in Sec. 4.3.6.

### Transit Time Limited Bandwidth

To analyze the contribution of RC and substrate conductance on the total device bandwidth, the frequency response is corrected by the contribution of the RC transfer function which has been determined in Sec. 4.3.2. This procedure is illustrated on the the measured frequency response and the corresponding corrected response of device C in Fig. 4.22. The transit time limited gain-bandwidth characteristics for device A, B and C are included in Fig. 4.19(b), 4.20(b) and 4.21(b), respectively. For device C, adding the contribution of the RC circuit without substrate conductance makes it possible to estimate the total regular device bandwidth. The values for the maximal bandwidth in either case are given in Tab. 4.7

device	measurement $f_{-3\text{dBe,max}}(\text{GHz})$			
	meas. #1	meas. #2	meas. #3	mean
A	9.29	7.91	9.51	8.90
B	7.16	6.31	6.61	6.70
C	13.43	10.83	11.50	11.8
	transit time limited $f_{-3\text{dBe,max,tr}}(\text{GHz})$			
	meas. #1	meas. #2	meas. #3	mean
A	11.5	8.99	10.9	10.48
B	7.12	6.83	7.88	7.28
C	14.9	14.2	14.6	14.6
	transit time+RC $f_{-3\text{dBe,max}}(\text{GHz})$			
	meas. #1	meas. #2	meas. #3	mean
C	13.4	12.8	13.3	13.1

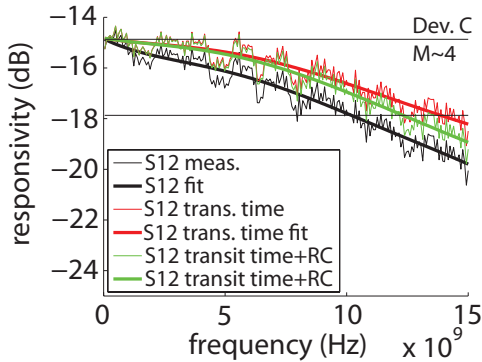
Table 4.7: Maximal  $-3$  dB bandwidth extracted from measurement.

Figure 4.22: Measured and corrected frequency response of device C.

For device A and B the maximal transit time limited bandwidth is only slightly higher than the maximal total device bandwidth (see Tab. 4.7). Therefore, the device is mainly transit time limited. As

expected the RC-contribution effects device A slightly more than device B.

Due to the substrate conductance, device C is strongly limited by the RC time constant. The estimated maximal transit time bandwidth is approximately 14.6 GHz. Assuming a device without substrate conductance, but taking into account the expected RC-limitations, a total device bandwidth of approximately 13.1 GHz is estimated.

#### 4.3.4 Time Domain Measurement Setup

Here, we will further investigate the reduced maximal bandwidth of device B observed in Sec. 4.3.3. For that purpose, time domain measurements are performed using the setup shown in Fig. 4.23. We apply a step like signal using the signal generator and we measure rise and fall times of the APD response. This measurement is influenced by the limited rise and fall-time of the pattern generator. Nevertheless, some interesting effects can be observed by analyzing the relative change of the step response at various bias points or temperatures. These observations can not be made in the frequency domain.

#### 4.3.5 Rise- and Fall-Time

In general, the rise and fall times are associated with the time constant between 10 – 90% of the signal amplitude,  $\tau_{10-90\%}$ . For the analysis in this work we introduce additional time constants for the fast component of the signal slope 10 – 70%,  $\tau_{10-70\%}$  and 10 – 80%,  $\tau_{10-80\%}$ . This allows us to analyze fast and slow components of the signal under various circumstances.

#### 4.3.6 Rise- and Fall-Time Measurement

In this analysis we limit ourselves to bias points above 20 V, far above the punch-through which is  $V_{pt} = 15.5$  V. At lower bias voltages the analysis is compromised by noise due to the small signal amplitude which makes it difficult to reliably determine the corresponding signal amplitude for the rise- and fall time analysis. The rising and falling signal slopes for device B at various bias points are shown in Fig. 4.24.

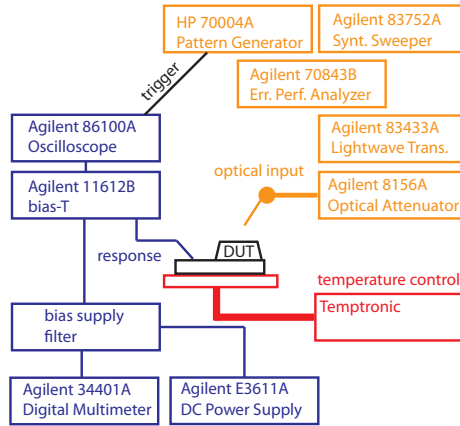


Figure 4.23: Setup for rise- and fall-time measurement and eye diagram.

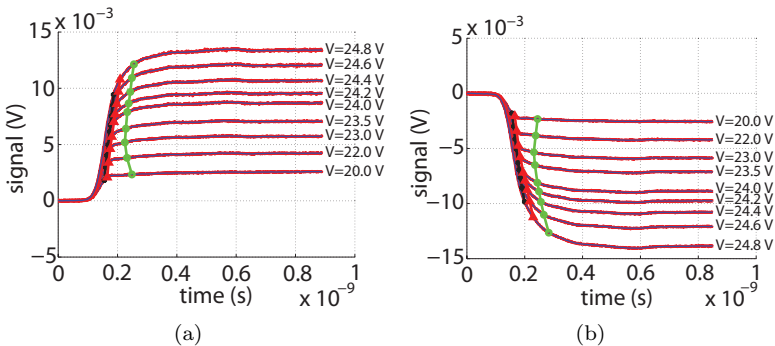


Figure 4.24: Signal slope for various applied bias voltage in device B (a) rising slope, (b) falling slope

A higher bias voltage leads to higher multiplication gain which results in a larger signal amplitude. For the analysis the noise has been smoothed out without changing the features of the signal itself. Both time constants for fast and slow components increase for

higher multiplication gain due to avalanche build-up time as shown in Fig. 4.25. For low bias voltages, corresponding to a lower electric field, the time constants of the slow component increases while the fast component remains nearly constant. Due to that different behavior, we conclude that the slow component and fast component are the result of a different transport mechanism or carrier types.

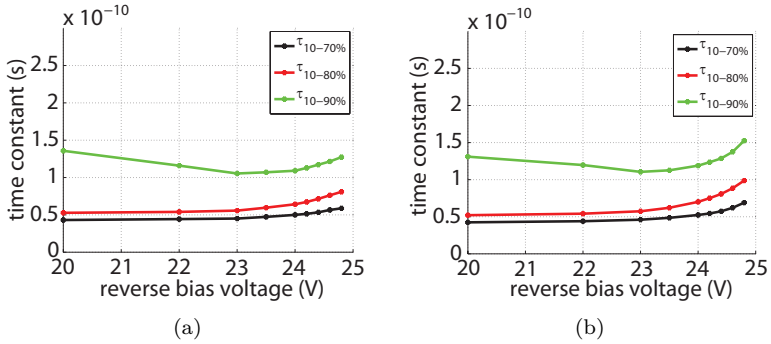


Figure 4.25: Time constant  $\tau$  of signal slope vs. reverse bias voltages (a) rising slope, (b) falling slope

For further investigation, the temperature dependence of the rise time constants at high voltage  $V = 24.4$  V in Fig. 4.26(a) and low voltage  $V = 20.0$  V in Fig. 4.26(b) are analyzed. At high voltage the time constants decrease due to a decreased impact ionization rate at higher temperature for a fixed bias voltage. This results in smaller gain and hence a smaller avalanche build-up time. This mechanism affects slow and fast components in a similar way.

At low bias voltage the slow and fast component behave different from each other with respect to changing temperature. While the fast component remains nearly constant with temperature the slow component increases with temperature. We attribute this effect to a decreased mobility of charge carriers. However, such an effect only influences carrier transported by a moderate electric field or by diffusion. We expect that the saturation velocity itself is only very slightly temperature dependent [62]. Therefore, we conclude that at a bias voltage  $\leq 20$  V which corresponds to a multiplication gain of

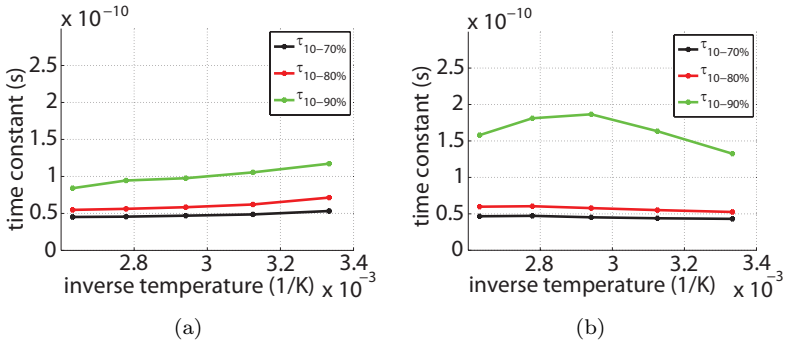


Figure 4.26: Rise time constant  $\tau$  of signal slope vs. inverse temperature at a bias voltage of (a) 24.4 V, (b) 20.0 V

roughly  $M \leq 5.4$  the electric field in the absorber is not high enough to guarantee drift of charge carriers at their saturation velocity. Due to the existence of the fast slope and due to the fact that the saturation velocity for holes is achieved at higher electric fields, we conclude that the slow part of the response is caused by holes. At very high temperature the rise time constant decreases again, because of the effect of reduced avalanche multiplication.

We do not observe an effect of pile-up of charge carriers at hetero-interfaces. This pile-up effect would lead to a distinctive decrease of the slow time constant at higher temperature [31]. This reduction would result from an increased transfer of carriers over the barrier by thermionic emission at higher temperatures.

### Effect of Optical Generation around $V_{pt}$

Since the electric field in the absorber just above  $V_{pt}$  is very low, optical generated carriers may have considerable effect on the electric field. The rise- and fall-time measurements have been taken for a photo current of  $6 \mu A$  at a reverse bias voltage of 20 V. This photo current corresponds to less than  $-22$  dBm optical input power. Using drift-diffusion simulation we notice that the electric field is slightly reduced by the optical generated carriers. In the dark current case,

the minimal electric field in the absorber at 20 V reverse bias voltage is roughly  $23 \text{ kV/cm}$ . For the photo current case the electric field is  $19 \text{ kV/cm}$ . This small difference may amplify the effect of slow hole transport. At 23 V reverse bias voltage, the minimal electric field with illumination is  $43.7 \text{ kV/cm}$  compared to  $44.1 \text{ kV/cm}$  without illumination. The electric field is only 1 % smaller.

### 4.3.7 Sensitivity

To validate the APD structure for use in PON applications, the sensitivity of a prototype receiver is measured. Fig. 4.27 [30] presents the sensitivity for a BER of  $10^{-9}$  at  $10 \text{ Gbit/s}$  of device B. The measured sensitivity of  $-27 \text{ dBm}$  make this device eligible for use in 10G-PON networks (see Sec. 2.1.1).

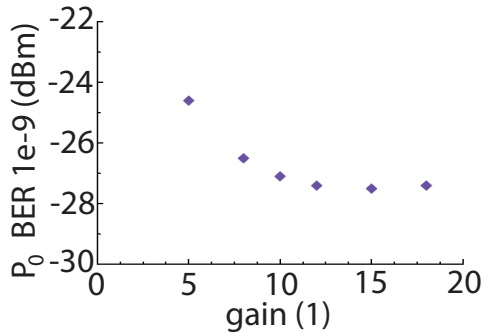


Figure 4.27: Sensitivity measurement of prototype APD receiver for a BER of  $10^{-9}$  at  $10 \text{ GHz}$  [30].

### 4.3.8 Eye Diagram

The eye diagram is a qualitative measure for the capability of an optical detector to recover a random signal pattern of given length. The height of the eye gives information about the SNR and the capabilities to distinguish between different symbols. The eye width is important with respect to timing jitter [3].

The eye diagram for a 10 GHz,  $2^{31}$  non-return-to-zero (NRZ) pseudorandom binary sequence (PRBS) for device B for a reverse bias voltage of 20.0 V is given in Fig. 4.28(a), for 23.0 V in Fig. 4.28(b) and for 24.8 V in Fig. 4.28(c). The extinction ratio is 14 dB. The mean optical input power remains the same for all bias points. For increasing voltage and hence increasing multiplication gain, the signal amplitude increases, which results in an eye with a larger opening. This translates into a sensitivity increase. To analyze this behavior the eye width and the eye height are directly extracted from the oscilloscope and plotted against the applied bias voltage in Fig. 4.28(d). First, both eye height and width increase due to the increased signal gain. Around 24 V the width of the eye starts to decrease as result of the avalanche build-time. This can be observed in Fig. 4.28(c) as well. For even higher voltages the slow component due to avalanche multiplication starts to influence the height of the eye. The increased excess noise leads to an additional closing of the eye as well.

The  $-3$  dB bandwidth of the device is around 6.7 GHz (see Sec. 4.3.3). In Sec. 4.3.6 we observed slow tails with time constants  $\tau_{10-90\%}$  of over 100 ps. Nevertheless, an open eye can be achieved for the similar device design at 10 GHz which is mainly the result of the internal signal gain rising the signal amplitude sufficiently.

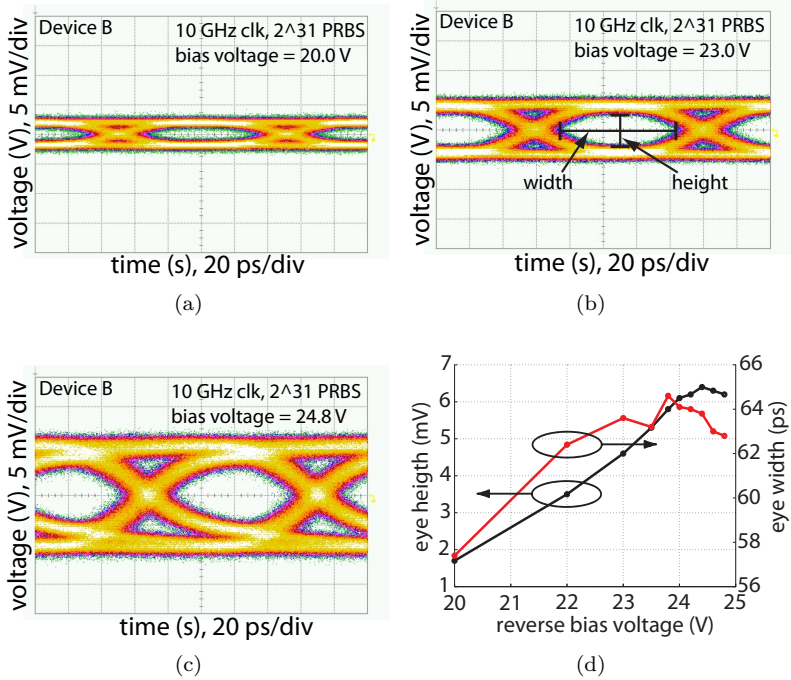


Figure 4.28: Eye diagram for device B at 10 GHz (a) bias voltage of 20.0 V, (b) bias voltage of 23.0 V, (c) bias voltage of 24.8 V, (d) eye width and eye height with respect to the applied reverse bias voltage.

## 4.4 Summary

### 4.4.1 Design

Five epitaxial structures have been developed. The epitaxial structures I, II and III perform as expected. The main achievements with respect to performance of the APD device fabricated from this epitaxial structures are:

- Device A and B are  $10^{\text{G}}\text{Bit/s}$  detectors with a gain-bandwidth product above 80 GHz. The large active diameter of  $32\ \mu\text{m}$  allows cost efficient coupling to optical fibers. The dark current is reasonably low for commercial applications. Device B, with a  $-3\ \text{dBe}$  bandwidth of 6.7 GHz, shows a sensitivity of  $-27\ \text{dBm}$  at  $10^{\text{G}}\text{Bit/s}$  using a prototype receiver circuit. This makes device B eligible for use in future 10G-PON networks. The eye diagram and therefore the sensitivity is influenced by slow tails observed in device B. The higher  $-3\ \text{dBe}$  bandwidth of device A of 8.9 GHz promises higher sensitivity operation.
- Device C shows a 14.6 GHz transit time limited  $-3\ \text{dBe}$  bandwidth and a gain-bandwidth product above 80 GHz for an active diameter of  $12\ \mu\text{m}$ . The device bandwidth including RC is estimated to be 13.1 GHz which is too low for 25G operation. Prototype receiver circuits need to be implemented to reveal the potential of this structure for future fiber optical networks.
- Device B and C have a very competitive low breakdown voltage  $V_{\text{br}}$ . This simplifies biasing and reduces their power consumption.
- All three devices show a low temperature dependence  $\rho$ . In particular, the temperature dependence of device C is within one of the lowest reported for SACM APDs.

### 4.4.2 Analysis

Analysis results for a multitude of APD structures are presented. Not only intended effects but also unintended characteristics are analyzed.

The comparative study goes beyond what is usually reported in literature and therefore improves current knowledge of APD devices. The novelties are:

- The comparative analysis of dark current activation energies vs. reverse bias voltage in SACM APDs with various breakdown mechanisms. The result of this analysis is that dark current in the operation regime is caused by generation-recombination in the absorber and grading region at the interface between APD and passivation layer.
- Comparative analysis of temperature dependent breakdown voltage  $V_{br}$  for three different APD devices. The device with the thinnest multiplication layer shows the smallest temperature dependence which is an effect of non-local impact ionization.
- The S11 characteristics have been measured and small signal equivalent circuits, including parasitic substrate conductance, have been extracted. The estimation of RC-transfer function allows the determination of transit time limited bandwidth. The analysis shows that device C is RC-limited due to parasitic substrate conductance, while device A and B are not significantly influenced by RC.
- Slow and fast response of device B have been analyzed using time and frequency domain characterization techniques. The analysis shows that slow tails present in the time domain are caused by holes traveling below the saturation velocity.

## Part II

# Simulation of Avalanche Photodiodes



# Chapter 5

## Simulation of Avalanche Photodiodes

### 5.1 Simulation Model Requirements

The goal of a transport model for device optimization is to describe the reality as close as necessary using the smallest possible computational power. Due to this requirement, drift-diffusion based model have been very popular in the past few decades. However, for smaller device dimensions and fast changing electric fields, the description given by moment-based transport models are reaching their limits [63]. In this context, the following discussion defines the requirements for the accurate simulations of state-of-the-art SACM APD structures.

#### 5.1.1 Non-Equilibrium Transport

Electric fields up to  $700 - 900 \text{ kV/cm}$  are expected in the multiplication regions of SACM APDs. Fig. 2.6 shows a typical electric field profile at the operation point for a multiplication region thickness of  $200 \text{ nm}$ . The electric field increases by several hundreds of  $\text{kV/cm}$  within a small distance. Such sudden electric field changes give rise to non-equilibrium transport effects [63]. Furthermore, engineered multiplication regions (see Sec. 2.10.2) consist of several layers in the

orders of few tens of nm thickness. The sudden band diagram offsets at the material boundaries lead to a sudden change of the carrier kinetic energies. The carrier distribution function enters a non-equilibrium state which influences the impact ionization behavior.

The simulated inelastic mean free path distance  $l_{in}$  for  $\text{In}_{0.52}\text{Al}_{0.48}\text{As}$  (InAlAs) bulk electrons at equilibrium is shown in Fig. 5.1. The calculations have been performed using a MC simulator (see Sec. 5.4). The inelastic mechanisms under consideration are polar- and non-polar optical phonon scattering, phonon assisted intervalley scattering and impact ionization. In general, it is assumed that a carrier requires about three times  $l_{in}$  to thermalize with the lattice [63]. A peak in the extracted mean field distance between inelastic scattering events is found at an electric field corresponding to the velocity overshoot condition in bulk InAlAs. At this particular electric field the carriers are traveling fast and the scattering rate is still relative low. For higher electric field the distance strongly decreases mainly due to the overall increased scattering probability at higher energy.

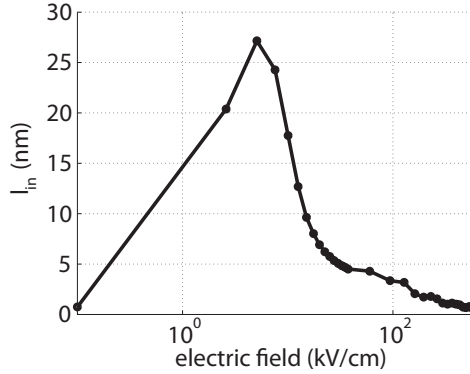


Figure 5.1: Mean distance covered between two inelastic scattering events for thermalized carriers in bulk InAlAs.

However, this analysis is based on a steady-state condition. More conclusive is the analysis of the dynamics to reach an equilibrium state. Fig. 5.2 shows the mean total energy and the mean velocity of the ensemble vs. simulation time. The carriers start at  $t = 0$  ps

with a thermal energy of  $kT = 25$  meV. At the beginning of the simulation the electric field is suddenly increased and the carriers are accelerated. Depending on the applied field it can take up to few ps until a local equilibrium condition is reached again. Long settling times are observed for electric field values corresponding to long mean inelastic free path distances (see Fig. 5.1). The corresponding mean distance which the ensemble travels before it reaches local equilibrium is shown in figure 5.3.

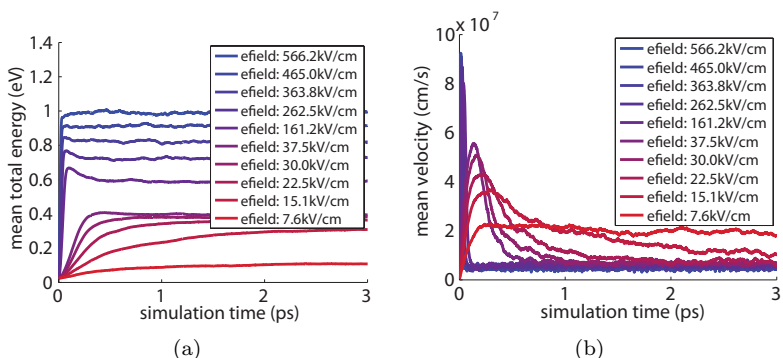


Figure 5.2: InAlAs bulk ensemble simulation at various electric fields with 2000 electrons starting with a mean energy of 25 meV: (a) mean total carrier energy vs. simulation time, (b) mean carrier velocity vs. simulation time

The mean distance strongly depends on the initial carrier distribution. In Fig. 5.4 the mean energies and mean velocities vs. mean displacement of the ensemble are shown for an experiment with a heated initial carrier distribution. The ensemble is heated by performing a bulk simulation of electrons at an electric field of 150 kV/cm. This is a realistic value for the electric field at the p-side of the field control layer. Once the ensemble is in local equilibrium the electric field is suddenly increased. The mean distance required to reach local equilibrium is approximately 25 nm. This distance is significant for thin APDs and in band gap engineered structures where performance critical physical effects happen on a scale of few tens of nanometers.

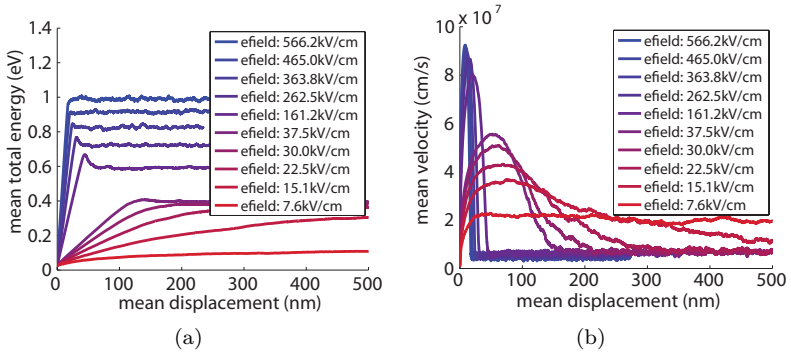


Figure 5.3: InAlAs bulk ensemble simulation at various electric fields with 2000 electrons starting with a mean energy of 25 meV: (a) mean total energy vs. mean displacement of the ensemble, (b) mean carrier velocity vs. mean displacement of the ensemble

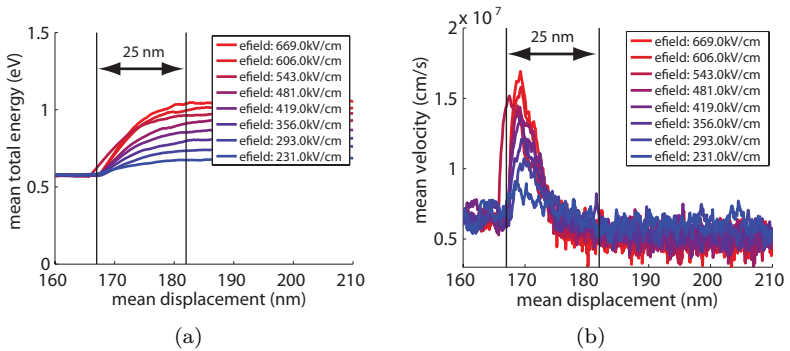


Figure 5.4: Bulk simulation of electrons in InAlAs. The initial electric field is 150 kV/cm. (a) Mean total carrier energy vs. mean displacement of the ensemble, (b) Mean carrier velocity vs. mean displacement of the ensemble.

### 5.1.2 Non-Local Impact Ionization

As described in Sec. 2.2, local impact ionization models relate the impact ionization rate with the local electric field and neglect the carrier acceleration profile prior to this point. They can not describe dead-space effects as well as the shape of the probability density function (PDF). The discrepancy in the shape of the PDF in Fig. 2.2 shows that we can expect local models to fail description in small structures as well as for high electric fields. Therefore, the change of multiplication gain and excess noise for varying multiplication layer thickness or band gap engineered structures can not be accurately described.

A local energy dependent model can improve the situation [63,64]. However, the accurate description of the impact ionization relies on the exact knowledge of the high energy tail of the carrier energy distribution as well as the correct modeling of the acceleration dynamics. In the case of small scale devices where electric fields or materials change within few tens of nanometers, non-equilibrium energy distribution functions have to be expected. This energy distributions are not a priori known.

### 5.1.3 Carrier Energy

The impact ionization process requires an initial carrier energy larger than the band gap energy to create a new electron-hole pair. In general high band gap materials, such as InAlAs with  $E_g = 1.45$  eV, are chosen for the impact ionization region to avoid dark current by band-to-band tunneling in thin multiplication regions. Therefore, a significant high energy tail far above the band gap energy is to be expected. The parabolic effective mass description fails to describe carrier dynamics at such energies. In general, this model is valid up to few tens of meV. Non-parabolic band structures have an extended validity. Fig. 5.5(a) shows a comparison of the density of states (DOS) for the InAlAs  $\Gamma_6$ -valley between a spherical parabolic and non-parabolic approximation as well as a full band (FB) reference. Above an energy of about 0.7 eV the DOS of the non-parabolic description differs significantly. Since many scattering rates are proportional to the DOS, dynamics above 0.7 eV are only approximately described.

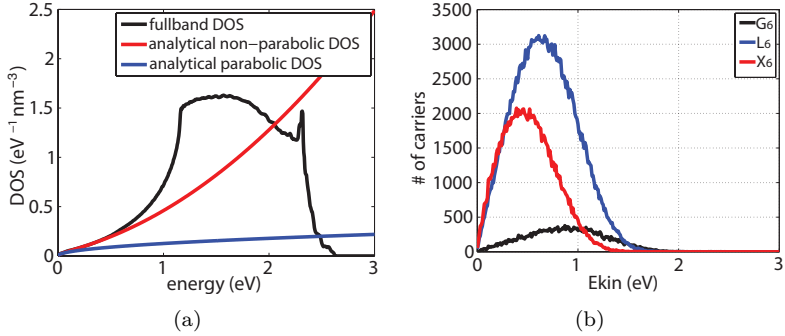


Figure 5.5: Validity of non-parabolic band structure approximation (a) Comparison of the density of states for an analytic spherical parabolic, non-parabolic and full band structure in the  $\Gamma_6$ -valley, (b) Electron energy distribution in the multiplication region of a typical SACM APD calculated using non-parabolic band structure approximation.

In Fig. 5.5(b) the kinetic energy of electrons at the n-side of an InAlAs multiplication layer is shown. According to our simulations, the majority of the carriers can be found below 1 eV. Therefore, transport of the majority of the carriers is pretty well described by a non-spherical band structure approximation [64]. However, the high energy tail is decisive for the avalanche multiplication process. FB-MC investigation in GaAs [65] show a mean carrier energy before impact ionization of more than 4 eV at 900 kV/cm. Therefore, the accurate description of the impact ionization process in InAlAs requires a FB model for carrier dynamics and scattering up to approximately 5 eV.

### 5.1.4 Summary

To conclude this assessment a summary of the main requirements for the simulation model is given:

- Non-local and non-equilibrium effects dominate device performance in high-speed, small scale APDs and ask for an accurate description of non-equilibrium carrier transport.
- Accurate description of the high energy tails in the distribution function is necessary. The simulation model should allow an extension to FB.
- In the long term, extraction of material properties from ab-initio band structure calculations are required to investigate more advanced material combinations and grading structures.
- A fast and highly parallelizable algorithm is needed for the simulation of large photodetector structure in a time efficient way.

The simulation framework should allow time efficient design optimization of state-of-the-art APD devices. Figure of merits are

- multiplication gain vs. applied reverse bias voltage,
- device bandwidth vs. multiplication gain,
- excess noise.

Furthermore, it would be interesting to investigate

- saturation effects due to overload,
- temperature dependence of multiplication gain and excess noise.

## 5.2 Boltzmann Transport Equation

### Introduction

To accurately describe the non-equilibrium carrier transport and non-local impact ionization, the carrier distribution function  $f(\mathbf{r}, \mathbf{k}, t)$  needs to be found. This distribution function can be obtained by solving the Boltzmann transport equation (BTE) [66]. The semi-classical BTE is a balance equation for the number of particles  $f(\mathbf{r}, \mathbf{k}, t)d\mathbf{r}d\mathbf{k}$  which can be found in a phase volume element  $d\mathbf{r}d\mathbf{k}$  at time  $t$ . For

scattering from and into the volume element, temporal and spatial locality is assumed [67]. The semi-classical BTE treats carriers as classical particles with well known position and momentum [68, 69] which propagate according to Newton's law. Quantum mechanics is used to describe collisions.

The BTE is an integro-differential equation in the six-dimensional phase space  $(\mathbf{r}, \mathbf{k})$  and in  $t$  [63, 67]:

$$\left\{ \frac{\partial}{\partial t} + \mathbf{v}_g \cdot \nabla_{\mathbf{r}} + \frac{q\mathbf{F}}{\hbar} \cdot \nabla_{\mathbf{k}} \right\} f(\mathbf{r}, \mathbf{k}, t) = \sum_{\mathbf{k}'} \{ S(\mathbf{k}, \mathbf{k}') f(\mathbf{r}, \mathbf{k}', t) [1 - f(\mathbf{r}, \mathbf{k}, t)] - S(\mathbf{k}', \mathbf{k}) f(\mathbf{r}, \mathbf{k}, t) [1 - f(\mathbf{r}, \mathbf{k}', t)] \}. \quad (5.1)$$

$f(\mathbf{r}, \mathbf{k}, t)$  represents the carrier distribution function,  $\mathbf{F}$  is the electric field strength,  $S(\mathbf{k}', \mathbf{k})$  and  $S(\mathbf{k}, \mathbf{k}')$  are the in- and out-scattering probabilities, respectively.  $\mathbf{v}_g(\mathbf{k}, \mathbf{r}) = \nabla_{\mathbf{k}} E(\mathbf{k}, \mathbf{r})/\hbar$  is the group velocity.

### Validity

The BTE can be used to describe transport in inhomogeneous materials with arbitrary band structures [63, 70]. The basic assumptions are the adiabatic approximation and the validity of the perturbation theory [71]. For the adiabatic approximation the carrier wave function answers instantaneously to the change of the ionic motion. This can be described by the condition [71]

$$l \geq \frac{1}{q} \quad (5.2)$$

with  $l$  being the mean free path length and  $q$  being the magnitude of the phonon wave vector.

The perturbation theory is valid if the perturbation is small and the unperturbed electron remains in an eigenstate for sufficiently long time [71]. Using the Heisenberg uncertainty principle [69], the requirement on the energy relaxation  $\tau_e$  time can be written as [72]

$$\tau_e \gg \Delta t = \frac{\hbar}{\Delta E}. \quad (5.3)$$

In terms of mean free path length this condition can be written as [71]

$$l \geq \lambda_{br} = \frac{1}{k} \quad (5.4)$$

with  $\lambda_{br}$  the de Broglie wavelength and  $k$  the magnitude of the electron wave vector. This condition is not necessarily fulfilled at very high energies for which the time and distance between scattering events becomes very small.

### Collisional Broadening

In the standard approach, the scattering probability is assumed to be proportional to a delta function  $\delta(E_f - E_i \pm \hbar\omega)$ .  $E_i$  is the initial energy of the carrier,  $E_f$  is the final energy of the carrier and  $\hbar\omega$  is the energy change related to the scattering mechanism. However, at high energies the small time between two scattering events results in a broadening of the final energy states of the scattering process [68, 71]. The possible final energy state of the carrier is broadened by [68]

$$\Delta E \simeq \frac{2\hbar}{\tau} \quad (5.5)$$

with  $\tau$  being the mean time between collisions. Therefore, the number of possible final states is increased which alters the scattering probability [71] as well as the emission thresholds [73].

## 5.3 State-of-the-art APD Simulations

Since McIntyre's initial work on the local-field avalanche theory [20] in the year 1972 many different models have been suggested to describe the transport and the avalanche multiplication process in APDs. This research has been driven by the improved capabilities to artificially modify the impact ionization behavior of APDs by means of confinement of the impact ionization in thin multiplication regions and band diagram engineering (see Sec. 2.10). Taking advantage of non-local impact ionization effects, the sensitivity and gain-bandwidth product can be improved further than bulk material would allow for. In this section we present some recent examples for the simulation of

performance critical physical effects such as impact ionization dead-space and non-equilibrium carrier transport.

An analytical simulation using history dependent impact ionization coefficients has been proposed by [74, 75]. A system of coupled integral equations has been used by [76, 77]. A method to calculate the probability density function for the impact ionization distance using a Fokker-Planck model has been proposed by [78]. A numerical solution to a so called dead-space model is given by [79]. All models allow to analyze the effect of dead-space on the multiplication gain and the excess noise. Since, telecommunication APDs are operated in a regime where the bandwidth is limited by an interplay of transit time and impact ionization related build-up time, accurate modeling of non-equilibrium carrier transport through the device structure should be included for a thorough analysis. Accounting for non-equilibrium effects allows to describe the impact ionization process more exactly.

A common method to account for non-equilibrium transport effects is to solve the BTE (see Sec. 5.2). The MC method is a popular, well established numerical solution method of the BTE [66, 80]. MC is well suited for the analysis of non-equilibrium transport effects and can be employed as reference solution for other transport models [81]. The particle nature of the simulation allows an intuitive analysis of non-equilibrium dynamics as well as non-local impact ionization. An extension to FB is possible and is a solved problem for many popular materials [82]. MC simulations based on an analytical band structure approximation have an advantage in terms of computation time compared to the FB implementation.

A simple MC approach using one single valley with one single effective parabolic band for electrons and holes is used by [83–85]. This effective valley represents the mass of the carriers at high energies. MC based on non-parabolic band structure approximation can give good agreement with measurement and FB-MC calculations. This has been shown for multiplication gain in GaAs [86] and InP [87] PIN diodes. In both cases three conduction band and three valence band valleys have been used. Based on four conduction band valleys, a good agreement for electron impact ionization PDF in GaAs compared to FB is presented by [64]. Using three conduction and valence band valleys, InAlAs-InGaAs superlattice [60], AlGaAs-GaAs engineered multiplication regions [88] and InAlAs-InGaAs SACM APD structures

have been investigated [89]. FB-MC simulations of avalanche multiplication in GaAs PIN diodes are presented by [65,90]. In [91] FB-MC has been used to investigate impact ionization in SACM APDs based on a InP multiplication region.

## 5.4 Monte Carlo Method

### 5.4.1 Introduction

The presented work is a step towards a MC simulation for self consistent (SC), FB description of hetero-structured InAlAs/InGaAs APDs. At present, the simulator employs a symmetric, non-parabolic band structure approximation (see Sec. 5.4.2), but allows a future expansion to FB. We are aware in the limitations of the band structure approximation with respect to the description of high energy transport and impact ionization, as discussed in Sec. 5.1.3. We follow the approach by Dunn et al. [86] for GaAs which considers the parameters of the impact ionization model as variable parameters to fit bulk characteristics. Doing so, this results in a very good agreement with numerical FB simulations and measurements [86].

The theory of MC simulations have been extensively covered in literature [80,82,92–96]. We will limit ourselves to an overview as well to some device simulation specific implementations and algorithms.

### 5.4.2 Physical Models

#### Band Structure

The simulator employs a spherical, non-parabolic band structure approximation with three conduction ( $\Gamma_6, L_6$  and  $X_6$ ) and three valence band (HH, LH and SO) valleys. The carrier energy  $E$  and its  $k$ -vector are related by following relationship [97]

$$\frac{\hbar^2 k^2}{2m^*} = \gamma(E) = E(1 + \alpha E) \quad (5.6)$$

with  $m^*$  the effective carrier mass and  $\alpha$  the non-parabolicity of the valley. This band structure accurately describes electron scattering and carrier dynamics to about 0.7 eV (see Sec. 5.1.3). For electrons

good agreement with FB calculations in GaAs can be found [86]. The use of a fourth conduction band valley ( $X_7$ ) would improve the validity of this model for the description of impact ionization [64].

The band structure model is quite approximative for hole valleys which show strong warping of the band structure. We follow Dunn et. al. [86] and consider the non-parabolicity of the valence band valleys to be a variable parameter to fit the bulk saturation velocity.

### Carrier Dynamics

The carrier dynamics during free flight is computed according to Newton dynamics with the approximation of a constant effective mass during the free flight time. The  $k$ -vector of the carrier after the free flight  $\mathbf{k}'$  is computed according to [94]

$$\mathbf{k}' = \mathbf{k}_0 + \frac{q\mathbf{F}}{\hbar}t. \quad (5.7)$$

$\mathbf{F}$  is the electric field,  $q$  is the carrier charge,  $t$  is the free flight time and  $\mathbf{k}_0$  the  $k$ -vector before the free flight. The position of the carrier after the free flight  $\mathbf{r}'$  is computed using [94]

$$\mathbf{r}' = \mathbf{r}_0 + \frac{\hbar\mathbf{k}_0}{m_c}t + \frac{1}{2}\frac{q\mathbf{F}}{m_c}t^2. \quad (5.8)$$

$\mathbf{r}_0$  is the initial carrier position and  $m_c = m^*\sqrt{1 + 4\alpha\gamma(E)}$  is the conductivity mass of the carrier at the start of its free flight. In this work, we use a three dimensional  $k$ -space and a one dimensional real space ( $z$ -direction).

### Scattering Mechanisms

The implemented scattering mechanisms are shown in Tab. 5.1. The formulas for the scattering rates used in our simulations are summarized in App. B. The corresponding material parameters can be found in App. C. The bulk scattering rates vs. carrier energy for InGaAs and InAlAs are shown for reference in App. D.

The Wiley overlap factor [98] and the Fawcett overlap integral [97] are implemented, but neglected in our simulations. We do not include impurity scattering for our device simulations which mainly plays a

role at low carrier energies. Furthermore, our simulation domain is mostly intrinsic. Collisional broadening is neglected (see Sec. 5.2). Impact ionization is implemented using a Keldysh approach with a

scatt. mech.	electron		hole	
	intra	inter	intra	inter
polar optical phonon	$\sqrt{[92, 97]}$	-	$\sqrt{[92, 97-99]}$	
non-polar optical phonon	$\sqrt{[80]}$	-	$\sqrt{[80, 98, 99]}$	
elastic acoustic phonon	$\sqrt{[80, 97]}$	-	$\sqrt{[80, 97, 99]}$	
alloy	$\sqrt{[62, 100]}$	-	$\sqrt{[101]}$	
ionized impurity	$\sqrt{[80, 93]}$	-	$\sqrt{[80, 99]}$	
impact ionization	$\sqrt{[86]}$	-	$\sqrt{[86]}$	-
intervalley	-	$\sqrt{[80]}$	-	-

Table 5.1: Implemented intravalley and intervalley scattering mechanisms.

hard-threshold at very high energies [86]. During an impact ionization event the band gap energy is subtracted from the initial carrier energy. The remaining energy is randomly distributed between the initial carrier, which remains in the initial valley, and the new electron and hole which start in the  $\Gamma_6^-$ - and HH-valley respectively.

## Hetero-Interface

Transport across hetero-interfaces in  $z$ -direction is treated classically by conserving energy and the moment parallel to the interface [102]. The transport across the hetero-junction is schematically shown in Fig. 5.6. During the transition from one material to the other carriers remain in their original valley. The kinetic energy of the electrons is increased or decreased by  $\Delta E_C$  and for holes by  $\Delta E_V$ . The energy  $\Delta E_{C,V}$  corresponds to the energy differences between the corresponding valley of the two materials ( $\Delta E_{C,\Gamma} = 0.504$  eV [11, 103, 104] for InAlAs/InGaAs). In case of reflection, the carrier is elastically scattered with a new  $k'_z = -k_z$ . Carrier-carrier scattering and carrier-plasmon scattering influence the transfer of carriers across the hetero-junction [102]. Our simulations are performed without this two mechanisms.

Therefore, the transfer of charge across the hetero-junction is slightly underestimated by our model, in particular at low electric fields. Device A, B and C have two double junction of the type shown in

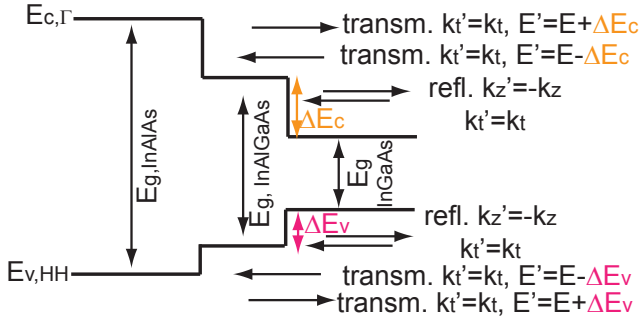


Figure 5.6: Schematic band diagram of double hetero-interface around the grading layers.

Fig. 5.6. The first one is between field control (#6, InAlAs), grading (#7, InGaAs) and absorber (#8, InGaAs). The second one can be found between absorber (#8, InGaAs), grading (#9, InGaAs) and p-buffer (#10, InAlAs). The first double junction forms a barrier for optical generated electrons traveling towards the n-side of the depletion layer. The second double junction acts as barrier for primary and secondary holes traveling towards the p-buffer.

We use a Wentzel-Kramers-Brillouin (WKB) tunneling model [105, 106] for tunneling through hetero-interfaces barriers. The model is implemented for all six valleys. We assume a triangular potential barrier. During the tunneling process the carriers remain in their original valleys.

### 5.4.3 Statistical Enhancement

#### Problem Description

Using the standard approach, MC simulations of APDs face following main statistic related problems:

1. The carrier concentration within the APD differs several orders of magnitude. The majority carrier concentration on the p- and the n-side of the diode are in orders of the doping concentration ( $10^{17} - 10^{19} \text{ 1/cm}^3$ ). In the depletion region carriers are created by thermal generation, optical absorption or tunneling. Drift-diffusion simulation for an optical input power of  $-20 \text{ dBm}$  in absence of multiplication gain result in carrier concentrations in orders of  $10^{11} \text{ 1/cm}^3$  within the depletion region. The interesting device physics, such as impact ionization or velocity overshoots, happen in this low density regions. Using a fixed super-particle size [92] for the entire device results in problems in terms of resolution of the low density region and computation time.
2. Impact ionization events are statistically very rare. To obtain sufficient statistics long simulation times are required.
3. The very large simulation domain of few  $\mu\text{m}$  increases the computation time.

### Limitation of Simulation Domain

The statistical problems can partially be resolved by limiting the simulation domain to the depletion region and only simulating optical generated carriers. However, this approach does not allow self-consistent electric field updates.

### Multiple Refresh Method

If an electric field update needs to be included, e.g. for rigorous hetero-interfaces treatment or overload analysis, the high doped regions need to be included to the simulation domain. The resulting carrier concentration gradient asks for statistical enhancement or variation reduction technique. Various statistical enhancement methods exist in literature [107, 108]. For the self-consistent MC simulator a simplified multiple refresh method [93] is used to improve the statistics in the low density region. The method is simplified in the sense that it is limited to the r-space and does not enhance rare k-values which would be a possible extension. Using this approach it is possible

to improve statistics in the low density region for steady-state while including the high doped region in the transport simulation.

Starting the MC simulation the device is discretized in  $r$ -space into several bins. In our case the bins represent at the same time the boundaries of the charge assignment for the Poisson update (see Sec. 5.4.5). Therefore, the width of the bin is limited by the convergence criteria for stable Poisson update procedure. The multiple refresh method acts on each single bin independently. Therefore, we limit ourself to a single bin for the following explanations. Each bin is assigned a desired amount of electron and holes  $N_{\text{des}}$ . In our simulation electrons and holes interact only during optical generation, impact ionization or by influencing the solution of the Poisson update. In a second step, each carrier is assigned an initial statistical weight  $w_j$ . In our case the initial statistical weight is proportional to the electron and hole charge  $Q$  in the corresponding bin divided by the amount of electron and holes in this particular bin  $w_j = Q/N_{\text{des}}$ .

The simulation starts and carriers are transported through the structure. During the simulation the actual number of carriers  $N^{\text{b}}$  varies. Those carriers may carry different statistical weights  $w_j^{\text{b}}$ . Each carrier contributes according to its statistical weight to the mean value and total carrier density. The number of carriers  $N^{\text{b}}$  is regularly verified. If the  $N^{\text{b}}$  is either too high or too low a multiple refresh event takes place. This criterium can be written as [93]

$$\frac{N^{\text{b}}}{N_{\text{des}}} < \frac{1}{r_p} \quad \text{and} \quad \frac{N^{\text{b}}}{N_{\text{des}}} > \frac{1}{r_p} \quad (5.9)$$

with  $r_p = 2$  being a predefined ratio. Furthermore, an additional criterium is used which avoids that few carriers with high statistical weight dominate the statistics in one bin [93]

$$\frac{\sum_{k=1}^{N^{\text{b}}} w_k^{\text{b}}}{\frac{1}{N_{\text{des}}}} > r_s \quad (5.10)$$

with  $r_s = 2$  being a predefined ratio and  $w_k^{\text{b}}$  are the statistical weights of the carriers which are found in the bin.

If statistical refresh is triggered a new sub-ensemble of  $N_{\text{des}}$  equally weighted carriers created. The total weight and therefore carrier

density is conserved. The new statistical weight after refresh  $w_j^a$  of the carriers is given by [93]

$$w_j^a = \frac{\sum_{k=1}^N w_k^b}{N_{\text{des}}}. \quad (5.11)$$

The new states of the carriers  $(\mathbf{r}_j^a, \mathbf{k}_j^a)$  are selected from the states of the old carriers  $(\mathbf{r}_j^b, \mathbf{k}_j^b)$ . This choice is random and weighted according to the  $w_k^b$ . In this procedure the expected mean value is conserved [93]. The variance is reduced and some information of the ensemble is lost. For a discussion of the error introduced by this procedure refer to [93, 109].

In case of an impact ionization event a new electron hole pair is created. Their statistical weight represent the same charge as the carrier causing the impact ionization event.

## 5.4.4 Self-Scattering Reduction

### Problem Description

At high electric fields carriers are present in the entire energy range from zero up to the hard-threshold energy of the impact ionization. The scattering rate increases several orders of magnitude for increasing energy (see Fig. 5.7(a)). Furthermore, the total scattering rate differs significantly between electron and hole valleys (see App. D). Using a single upper limit for the total scattering rate including self-scattering  $\Gamma$  results in a overhead in computation time because of many unnecessary self-scattering events in the low energy regime.

### Energy Dependent Total Scattering Rates

To reduce the amount of self-scattering, the simulation domain is divided into energy bins of constant width. The total scattering rates including self-scattering  $\Gamma_i$  are constant within this energy bin [93, 110, 111]. A step-wise constant total scattering rate results as can be seen in Fig. 5.7(b).

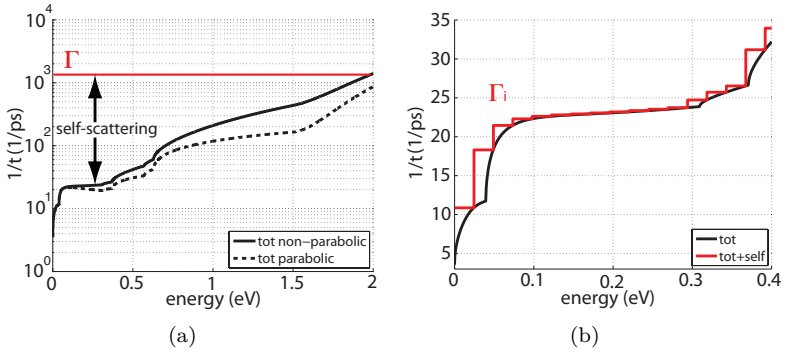


Figure 5.7: Difference between constant  $\Gamma$  and piecewise constant  $\Gamma_i$  total scattering rate including self-scattering for the  $\Gamma_6$ -valley of InAlAs (a) constant  $\Gamma$ , (b) piecewise constant  $\Gamma_i$ .

### Pre-Computation of Scattering Rates

Furthermore, the scattering rates of each mechanism and the total scattering rate are precomputed for each valley and region of the device on a fine energy grid. By doing so, the time required to treat a scattering event is reduced at the cost of the time for pre-computation and increased memory usage. Even though the scattering mechanism are given in analytical form, a significant speed up can be observed for long MC simulations. We did not find any significant difference between the simulation results with and without pre-computation of the scattering rates.

#### 5.4.5 Poisson Equation

For the SCMC simulation the non-linear PE is solved regularly in time to reflect the change in the electrostatic potential due to moving charges in the device. The electric field is extracted by the gradient of the electro-static potential. The non-linear PE [112] is solved in an iterative Newton scheme. Stability of the PE asks for a time step criterion. For an analysis of stability criteria of the PE refer to [112, 113]. Charge assignment is done on the mesh provided by

the multiple refresh method. This correspond to a nearest-grid-point (NGP) approach on a non-regular grid [96]. Ohmic boundary conditions are achieved by enforcing equilibrium carrier density at the contact. Carriers at the contact are injecting according to a velocity weighted Maxwellian approach [114].

### 5.4.6 Carrier Propagation

#### Main Propagation Loop

The flow chart for the propagation during one time step of length  $T$  of a single carrier  $n$  is shown in Fig. 5.8. Starting from an initial carrier at position  $\mathbf{r}_0$ , with an energy  $E(\mathbf{k}_0)$  at  $t = t_0$  the next free flight is terminated either by a scattering event, arrival at an energy interface, real space interface or by the end of the time step itself. Therefore, the next free flight time is determined by the minimum of

- the time to the next scattering event  $\tau_s = -\ln(1-r)/\Gamma_i$  with  $r$  being a random number,
- the time to reach a boundary in energy space  $\tau_E$ ,
- the time to reach a boundary in real space  $\tau_r$ ,
- the time to reach the time step boundary  $\tau_T = mT - t_0$  with  $m$  being the time step counter.

At the end of each free flight step, the carrier is treated according to the chosen mechanism interrupting the free flight. Then a new random number  $r$  is drawn and the next free flight time is determined. The validity of such a propagation scheme is shown by [115].

In case of scattering, a scattering event is stochastically chosen and the k-vector after scattering  $\mathbf{k}$  is determined. For a carrier arriving at an energy interface the value of  $\Gamma_i$  for the next time step is updated. If the carrier reaches a real space interface a special treatment of material boundaries can be required. If the carrier reaches a time step boundary the propagation of carrier  $n$  for this time step is terminated.

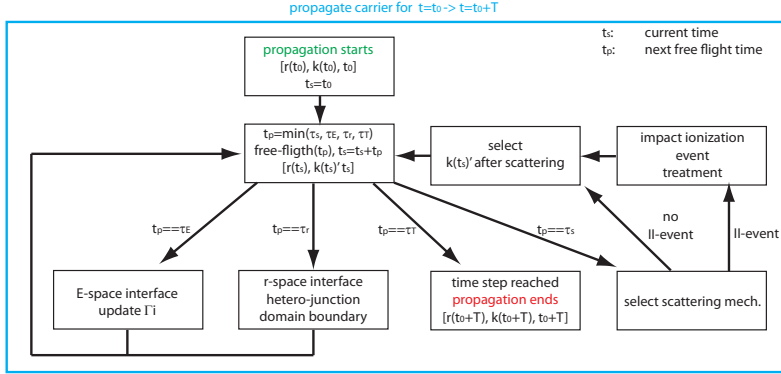


Figure 5.8: Flowchart for the propagation of a carrier from  $t = t_0$  to  $t = t_0 + T$ .

### Simulation Time Optimization

The computation time can be reduced if the number of free flight steps in a simulation is minimized. The determination of the next free flight time as well as the treatment of the carrier after the free flight is not negligible in terms of computation time. The duration of the free flight time itself does not influence the simulation time due to the analytic formulation of the carrier dynamics. Therefore, for a fixed simulation time the free flight time in each simulation step should be maximized.

There exists a trade-off between the number of energy bins and the free flight time. More energy bins reduce the amount of self-scattering and therefore increase  $\tau_s$  for each energy bin. On the other hand  $\tau_E$  decreases because of the smaller width of the energy bins. This trade-off between  $\tau_s$  and  $\tau_E$  depend on the total scattering rates, the electric field and the energy distribution function of the simulated ensemble. The time required to assign a carrier to an energy bin and therefore  $\Gamma_i$ -value of the next free flight can be neglected in the case of constant energy bin width. It is difficult to determine in beforehand the optimal number of energy bins for each individual valley and each material for an arbitrary simulation setup [111]. We found by

numerical experiments with various bin numbers that approximately 100 energy bins with constant width for an energy range from 0 eV to 2.45 eV result in a good trade-off for various electric field values.

### 5.4.7 Simulator Overview

The simulator has been developed for three main operation modes:

- Bulk MC simulation (BMC) which provides the framework to calibrate the simulation parameters to known bulk characteristics.
- Frozen field device MC simulation (FFMC) which is a non-self-consistent (NSC) simulation framework for gain, excess noise and bandwidth simulations.
- Self-consistent device MC simulation (SCMC) with PE update to extract steady-state velocity and carrier energy profiles. The term self-consistent in MC is used for an iterative approach for which carrier propagation and field update are calculated in separated steps.

#### BMC

Bulk simulations provide the framework to accurately tune the simulation parameters, such as deformation potentials, to obtain accurate bulk material characteristics. The simulation flow is shown in App. A. We are mainly interested in the physics at high electric fields present in the depletion region of the APD structure. The main calibration procedure is targeted at this high electric field values. In a series of ensemble simulations of equally weighted carriers, bulk properties such as carrier velocity vs. electric field and impact ionization rates are calibrated on either measured values or comparable simulations from literature.

#### FFMC

In this approach, we assume that the electric field does not change due to generation of carriers by optical generation and impact ionization.

Fig. 5.9 shows the electro static potential in steady-state within device A at 24 V which corresponds to a multiplication gain of approximately  $M = 3.7$ . The potential has been calculated using a drift-diffusion simulator without impact ionization [116]. Up to  $-10$  dBm optical input power the potential does not change due to the optical generated carriers. For 0 dBm the electric field in the absorber is significantly smaller while the field is increased in the multiplication region. Device C has a thinner multiplication layer. Hence the field required to achieve same multiplication gain as device A is increased. Since device C has a the same field control separation layer as device A, the electric field in the absorber is higher for the same multiplication gain. The effect of optically generated carriers on the electric field is less significant than for device A. The typical operation regime of our APD is between  $-20$  dBm and  $-30$  dBm. We consider our approximation to be valid in this regime. In Sec. 4.3.6 we notice that the electric field

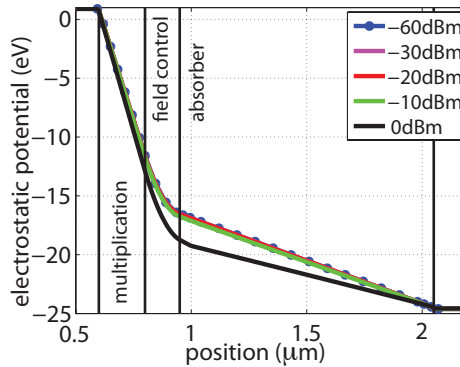


Figure 5.9: Electrostatic potential at reverse bias voltage of 24 V, computed using drift-diffusion simulator for various optical input power.

is influenced by optical generation at low bias voltage just above  $V_{pt}$  in device B. Our approach leads to an overestimation of the electric field in the absorber for device B at  $V = 20$  V and  $-22$  dBm optical input power. This bias voltage corresponds to a multiplication gain of approximately  $M = 5$ . The electric field value in the absorber is

23 kV/cm for dark condition and 19 kV/cm for optical generation. In comparison, the difference in the electric field for device A at 20 V reverse bias voltage ( $M = 2.5$ ) is less than 1%. Nevertheless, the simulations of device B are valid in the very low optical input power regime.

It has been mentioned that the NSC-MC method is not suited for the determination of drain and collector terminal currents in MOSFETs [117]. Coulomb effects which can influence device physics in highly doped regions can not be described [118]. However, our FFMC simulations are strictly limited to the depletion region for which the carrier densities are very low and applied electric field is high.

For the frozen field device simulation we only include optically generated carriers and their children created by impact ionization. We neglect any minority carriers entering the depletion region and any optical generation outside the depletion region which may cause diffusion tails. We assume that carriers leaving the device will not re-enter the depletion region. This does introduce a small error if carriers leave the depletion region to a region where they represent minority carriers. However, the amount of carriers leaving the depletion region on their corresponding minority side is negligible compared to those leaving the depletion region on their corresponding majority side. The electric fields in the depletion region are so strong that the carriers are forced towards their corresponding majority region. Once a carrier leaves the depletion region as majority carrier the assumption that the carriers do not enter the depletion region again is justified because the electric field created by the space charge [3]. This limits our simulation domain to the depletion region which does not change significantly once punch-through is achieved because the doping concentration on the n- and p-side buffers are in the order of  $10^{18}$  1/cm<sup>3</sup>.

Optically generated electron-hole pairs are created within the absorber region weighted according to the optical generation profile. This allows to differ between top- and bottom-illuminated devices. This generation profile has been computed using a transfer matrix method (TMM) [116] which allows to take into account transmission and reflection on the material boundaries. The first experiment starts with a single electron-hole pair which propagates through the device. In case of impact ionization an additional electron-hole pair is created (see App. A). The simulation continues until all carriers leave the

device. This procedure is repeated until sufficient statistics are obtained. Every one of those experiments is statistically independent of each other. The main disadvantage of this approach is the increasing simulation time with increasing multiplication gain. The higher the multiplication gain, the larger the amount of carriers to be simulated.

### SCMC

The simulation flow of SCMC is given in App. A. Compared to the FFMC simulation additional procedures for statistical enhancement (see Sec. 5.4.3), for electrical field update and ohmic boundary conditions (see Sec. 5.4.5) are included. An initial solution for the electric field is precomputed using a drift-diffusion simulator in absence of optical generation and impact ionization [116].

In each time step, new electron and holes are created according to the optical generation rate. The multiple refresh method sustains the approximative numbers of carriers in each real space bin. Therefore, the simulation time does not depend on the multiplication gain as well as the optical generation rate which is an advantage of this procedure compared to FFMC. Furthermore, due to the Poisson update the hetero-interfaces are more accurately included in the simulation. Simulations of transient responses including Poisson update are not stable. We apply this simulation scheme to extract steady-state energy and velocity profiles.

# Chapter 6

## Monte Carlo Calibration Results

This chapter presents bulk simulation results for  $\text{In}_{0.52}\text{Al}_{0.48}\text{As}$  (InAlAs) and  $\text{In}_{0.53}\text{Ga}_{0.47}\text{As}$  (InGaAs). The drift velocity and valley occupation vs. the electric field, the saturation velocity and the impact ionization rates are shown. To verify the correct description of non-local impact ionization simulations on InAlAs-PIN diodes are performed which are compared with measurement data from literature. Multiplication gain and excess noise factors in this diodes are analyzed.

### 6.1 Bulk Properties

Simulator parameters are taken from literature for similar simulation models. This will make the simulation results comparable. The parameters for InAlAs and InGaAs are listed in App. C. For the linear graded material InAlGaAs no reference data exist. We apply linear interpolation between InAlAs and InGaAs for the band structure parameters. The Keldysh impact ionization parameters are assumed to be free parameters to fit bulk impact ionization rates [86].

### 6.1.1 Simulation Procedure

Bulk properties are extracted by simulation of an ensemble of 2000 statistically independent carriers. After a settling time of 5 ps the mean values are extracted in time intervals of 1 ps. The time should be large enough to assume statistical independent sub-ensembles [93]. The simulation continues until the relative error of the time averaged mean velocity and energy is smaller than 1%.

To compute the impact ionization rate a single particle is simulated for  $10^4$  ps. After a settling time of 5 ps the distance between each impact ionization event is saved. During the impact ionization event a new electron-hole pair is created. The new electron starts in the  $\Gamma_6$ -valley and a new hole starts in the HH-valley. The initial carrier remains in its current valley [86]. The remaining energy is randomly distributed between this three carriers. Finally, the initial carrier or the corresponding child of the same type is randomly selected to continue propagation while the other two carries are deleted. The inverse of the mean traveling distance between each impact ionization event corresponds to the impact ionization rate,  $\alpha$  for electrons and  $\beta$  for holes.

### 6.1.2 Bulk Mean Carrier Velocity and Energy

The InGaAs electron velocity in Fig. 6.1(a) shows good agreement with simulation results [119] and measurements [120]. A mismatch in the amplitude of the peak velocity can be observed. However, a large variance in peak velocity of InGaAs comparing various reference simulations and measurements can be observed in literature [119]. Particular good agreement is found for the saturation velocity. The transition of carriers from the  $\Gamma_6$ - to the  $L_6$ -valleys is illustrated in Fig. 6.2(b). The  $L_6$ -valley has a higher effective electron mass which results in the typical peak velocity and negative differential resistance characteristics. Furthermore, increased scattering in the  $L_6$ -valley reduces the mean velocity. The corresponding mean kinetic energies in each valley and the total mean carrier energy is shown in Fig. 6.2(a). The ensemble in the  $\Gamma$ -valley is strongly heated before first inter-valley scattering events to the  $L_6$ - and the  $X_6$ -valley take

place. The hole velocity is in good agreement with simulation results from literature [121] and measurements [122] (see Fig. 6.1(b)).

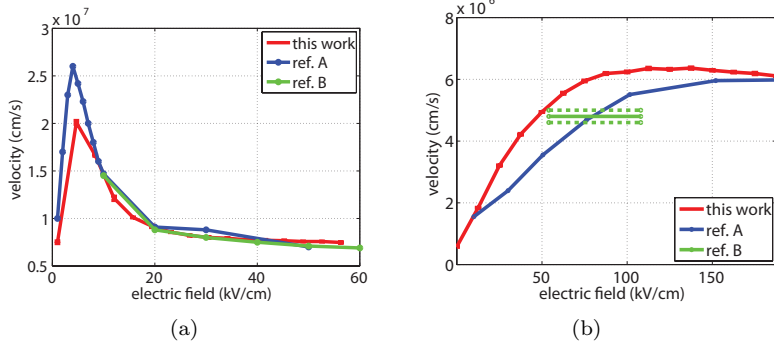


Figure 6.1: Bulk mean velocity vs. electric field for InGaAs: (a) electron velocity in comparison with simulation reference A [119] and measurement reference B [120], (b) hole velocity in comparison with simulation reference A [121] and measurement reference B [122]

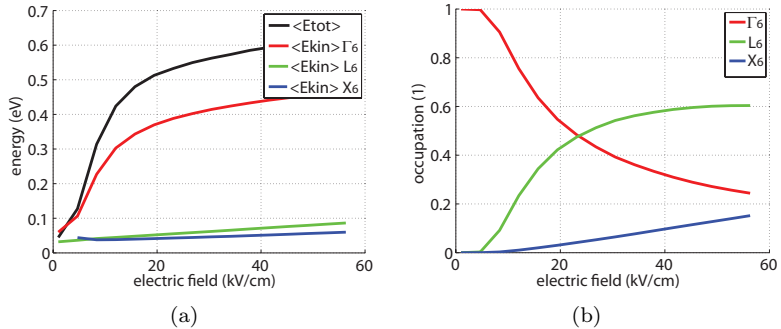


Figure 6.2: Bulk simulation results for electrons in InGaAs: (a) mean total energy and mean kinetic energy in each valley vs. electric field, (b) total occupation of conduction band valleys vs. electric field

The peak velocity of electrons in InAlAs in Fig. 6.3 corresponds to simulation data from Kim et al. [62]. Based on the measurement of transit time limited bandwidth in MODFETs [123] a saturation velocity of  $0.36 \cdot 10^7$  cm/s is extracted for a n-type doping concentration of  $1 \cdot 10^{18}$   $1/\text{cm}^3$ . From this result a saturation velocity of  $0.43 \cdot 10^7$  cm/s is extrapolated for undoped InAlAs [123]. Our simulated saturation velocity is approximately 50 % higher. The reason for the discrepancy between this simulation, the simulation results of Kim et al. [62] and the measured saturation velocity is not completely clarified. Our simulators and the simulator of Kim et al. [62] are using the same parameter set in order to make them comparable. Our simulator shows very good agreement for the velocity vs. field characteristics in InGaAs which assures a correct implementation of the major scattering mechanisms. It is assumed that the discrepancy results from different implementations, namely for the inter-valley scattering or the alloy scattering. The parameter set might not be entirely compatible, meaning the scattering models are not implemented in exact the same way. The mean energies and the valley occupation in Fig. 6.3(b) show similar behavior than InGaAs. However, the  $X_6$ -valley seems not to be occupied up to very high electric fields because of the large valley separation energy in InAlAs.

To our knowledge no measurement of saturation velocity or velocity vs. electric field profiles for holes in InAlAs exists. In this work an interpolation of the saturation velocities in InAs and AlAs stated in [124] is assumed. In general, a strong alloy scattering is expected by combining those two binary materials which leads to considerable lower saturation velocity compared to a linear interpolation. However, to our best knowledge no bowing parameter exists in literature. An estimation for the saturation velocity of  $0.3 \cdot 10^7$  cm/s to  $0.4 \cdot 10^7$  cm/s is given by [125]. The estimation is based on the observation that the hole saturation velocity in InGaAs is about 60 % smaller than the electron saturation velocity. It is assumed that InAlAs behaves similar to InGaAs. However, there is no proof of that matter. In doubt and due to missing reference data, a linear interpolation of the saturation velocity of the binaries is assumed. The corresponding non-parabolicity parameter have been chosen to fit this velocity. The saturation velocity value presented in this work is most probably

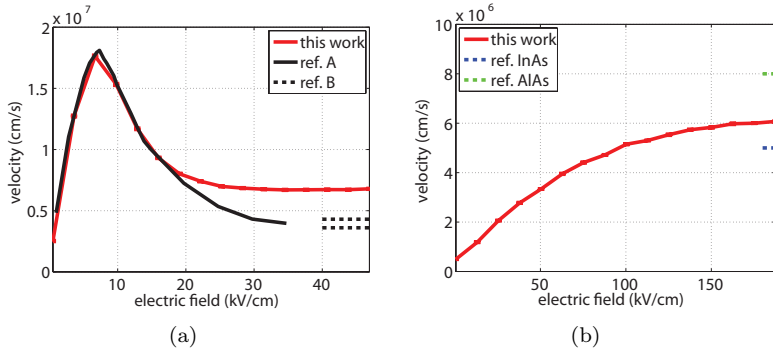


Figure 6.3: Bulk mean velocity vs. electric field for InAlAs: (a) electron velocity in comparison with simulation reference A [62] and measurement reference B [123], (b) hole velocity in comparison with the saturation velocity in InAs and AlAs according to [124].

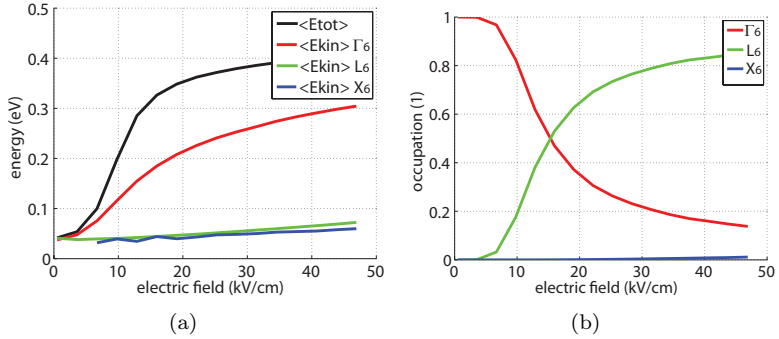


Figure 6.4: Bulk simulation results for electrons in InAlAs: (a) mean total energy and mean kinetic energy in each valley vs. electric field, (b) total occupation of conduction band valleys vs. electric field

overestimating the real hole saturation velocity. FB ab-initio simulations or time-of-flight measurements for holes in InAlAs measurements would be required to obtain more reliable reference values.

Nevertheless, it should be noted that even though saturation velocity for electrons and holes in InAlAs are overestimated the impact on the simulation of APDs should be limited. Primary electron and primary as well as secondary hole transport in InGaAs dominates the transit time limited bandwidth in SACM APDs. The correspondence of the saturation velocity in InGaAs with measured data is very good. Avalanche multiplication time includes carrier acceleration and transit time in the InAlAs multiplication layer. However, at high gain the scaling due to multiplication gain and k-ratio dominates the characteristics. We assume the simulated transit time limited bandwidth to be slightly overestimated compared to real devices.

### 6.1.3 Bulk Impact Ionization Rate

The pre-factor and the threshold energy of the Keldysh impact ionization model have been chosen to fit impact ionization rates from literature [18, 126]. For both materials a good correspondence to the measured data is found. The bulk impact ionization rate  $\alpha$  and  $\beta$  for electron and holes in InGaAs and InAlAs are shown in Fig. 6.5. The

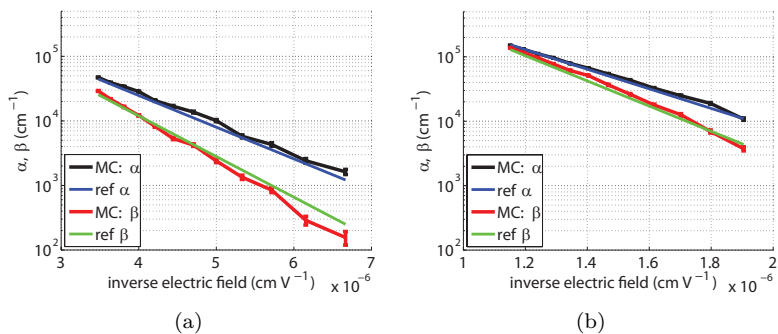


Figure 6.5: Bulk impact ionization rate  $\alpha$  and  $\beta$ : (a) MC results for InGaAs in comparison with measurements [126], (b) MC results for InAlAs in comparison with measurements [18]

SACM APD is designed to have an electric field below  $180 \text{ kV/cm}$  in the InGaAs layers to prevent band-to-band tunneling. Therefore, the

impact ionization rate of InGaAs has only been fitted up to an electric field value of  $300 \text{ kV/cm}$ .

## 6.2 PIN Diode

### 6.2.1 Simulation Procedure

Frozen field MC simulations of InAlAs-PIN diodes are performed to validate the bulk calibration. The reference structure and measurements are taken from [127]. It is not mentioned if the unintentional background doping of the intrinsic layer is n- or p-type. First, we are going to assume n-type background doping. The layer thickness and doping of the devices are summarized in Tab. 6.1. The p- and the n-side of the PIN structure are doped with  $N_d = N_a = 2 \cdot 10^{18} \text{ 1/cm}^3$ .

The exact electric field profile is precomputed using a drift-diffusion simulator [116]. This is in contrast to the work of Goh et al. [127] where it is assumed that the electric field in the intrinsic region is constant because of the relatively low unintentional background doping. In particular, for the device PIN-220 nm the electric field deviates considerably from a constant profile (see Fig. 6.6). The electric field at the p-side of the depletion layer is higher than on the n-side. To analyze the influence of the background doping in the intrinsic region two additional designs are simulated. The device PIN-220 nm-B has a very low unintentional doping of the intrinsic region which results in a quasi constant electric field. PIN-220 nm-C has a small p-type background doping which results in a electric field peak at the n-side of the depletion layer.

Only carriers within the depletion layer are included in the analysis. It is assumed that carriers leaving the depletion region do not enter the depletion region again [3]. To extract electron induced multiplication gain  $M_e$  a single electron is injected from the p-side of the intrinsic region (see Fig. 6.7). We assume that the initial carrier is injected with zero kinetic energy. It can be argued that the initial energy should be chosen according to the equilibrium distribution. However, we do not expect a large influence on avalanche multiplication gain. The high electric fields in this structure make the small initial energy difference in those two cases negligible.

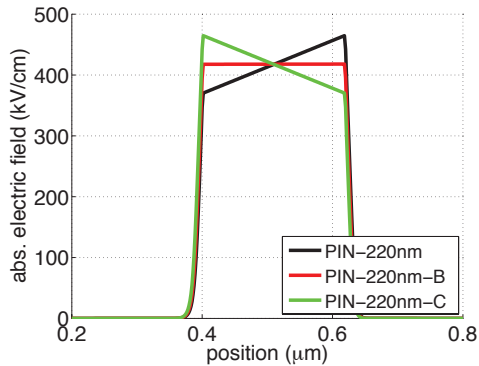


Figure 6.6: Absolute electric field in device PIN-220 nm, PIN-220 nm-B and PIN-220 nm-C for a reverse bias voltage of 8.4 V.

During an impact ionization event a new electron-hole pair is created. The new electron is found in the  $\Gamma_6$ -valley, the new hole in the HH-valley. The initial carrier remains in its current valley. The remaining energy after impact ionization is randomly distributed between the three carriers. The simulation continues until the initial carrier and all its children leave the intrinsic region. This procedure is repeated until sufficient statistics are obtained. Each experiment is statistically independent of the others and is therefore easy to parallelize. The presented results are based on 8000 statistically independent

device	$d_i$ (nm)	$N_i$ ( $1/\text{cm}^3$ )
PIN-108 nm	108	n-type $1 \cdot 10^{16}$
PIN-220 nm	220	n-type $3 \cdot 10^{16}$
PIN-505 nm	505	n-type $0.6 \cdot 10^{16}$
PIN-220 nm-B	220	n-type $1 \cdot 10^{14}$
PIN-220 nm-C	220	p-type $3 \cdot 10^{16}$

Table 6.1: Simulated PIN diodes: the structure corresponds to the PIN diodes used in [127].

experiments. The multiplication gain for this simulations is defined as the ratio between initial and final number of carriers

$$M_e = \frac{\text{final number of electrons} + \text{final number of holes}}{\text{initial number of electrons}}. \quad (6.1)$$

Furthermore, the excess noise factor

$$F_e = \frac{\langle M_e^2 \rangle}{\langle M_e \rangle^2} \quad (6.2)$$

is computed [65]. For hole induced multiplication gain  $M_h$  and hole induced multiplication excess noise the same procedure starts with a single hole injected from the n-side of the depletion layer (see Fig. 6.7(b)).

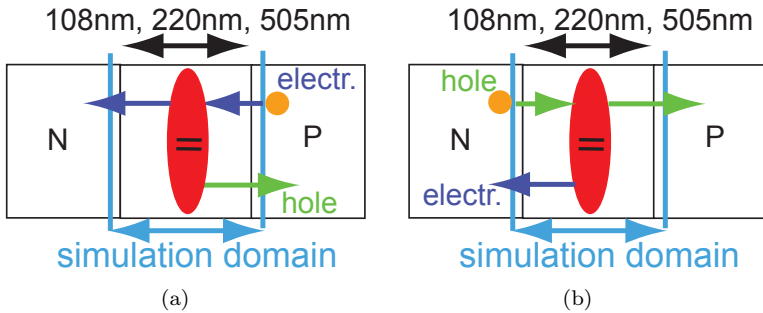


Figure 6.7: Schematic of PIN diode simulation (a) for electron induced gain, (b) for hole induced gain

## 6.2.2 Simulation Results

The electron and the hole induced multiplication gain is shown in Fig. 6.8.

The breakdown voltage for the PIN-110 nm is slightly underestimated by approximately 1 V or 10%  $V_{br}$  compared to measurements [127]. The agreement for PIN-220 nm is very good. For PIN-505 nm the multiplication gain is slightly underestimated. In all devices  $M_e$  is larger than  $M_h$  for the same bias voltage because  $\alpha > \beta$ . The correct

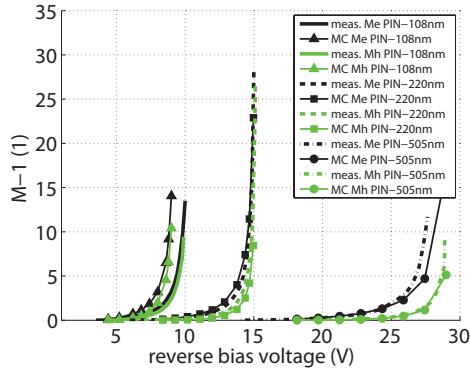


Figure 6.8: Simulated and measured gain vs. voltage characteristics for PIN-diodes of various thickness

scaling of the breakdown voltage for various thickness of the device is an indication for the accurate modeling of the non-local impact ionization. The spatial distribution of the impact ionization events within the depletion region is shown in Fig. 6.9 for the PIN-110 nm device. The position of the impact ionization events for electrons and holes are tracked on a 5 nm wide mesh. The number of impact ionization events in each mesh point is divided by the total number of impact ionization events for all bias points investigated. This allows to compare the spatial distribution and amount of electron and hole induced impact ionization events for various bias points. The simulation starting with an initial electron is shown in Fig. 6.9(a) and the result for an initial hole entering from the n-side is shown in Fig. 6.9(b). Following points should be noted:

1. Injected electrons and holes start with zero energy. The probability density function for the position of the initial impact ionization event is very narrow for both types of carriers. This leads to strong increase of impact ionization events once carriers traveled further than their dead-space.

2. The exact width of the dead-space can not directly be extracted from Fig. 6.9(a) due to impact ionization by secondary carriers. Nevertheless, its existence is clearly visible.
3. The ratio between electron and hole induced impact ionization rates depends on  $\alpha$  and  $\beta$  as well as on the initial carrier type. Only the combination of electron injection and  $\alpha \gg \beta$  allows for a low  $k$ -ratio.

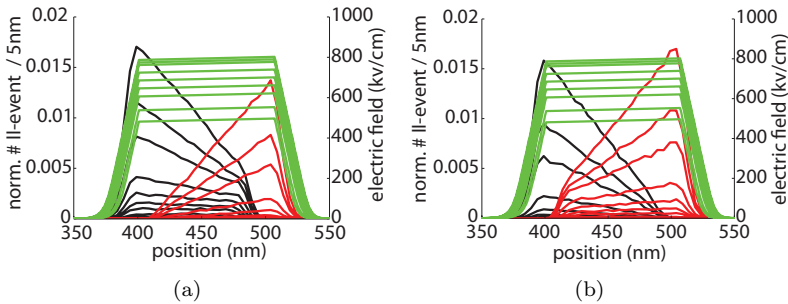


Figure 6.9: Electric field in the PIN-100nm (green), normalized number of electron induced impact ionization events (black), number of hole induced impact ionization event (red) for various multiplication gain (a) electron injection configuration with  $M_e=1.1, 1.3, 1.7, 2.1, 2.9, 4.2, 7.5, 10.2, 15.0$  from bottom to top, (b) hole injection configuration with  $M_h=1.0, 1.1, 1.2, 1.5, 2.0, 3.0, 5.6, 7.6, 11.4$  from bottom to top

Fig. 6.10 presents the simulated excess noise factor of the three devices in comparison with local theory [35]. It is possible to attribute an effective  $k$ -ratio from local theory to the extracted excess noise. The corresponding best fit values are PIN-110 nm  $k_{\text{eff}} = 0.19$ , PIN-220 nm  $k_{\text{eff}} = 0.23$ , PIN-505 nm  $k_{\text{eff}} = 0.22$ . Three main observations can be made:

1. The effective  $k$ -ratio extracted from the PIN simulations is significantly lower than the bulk  $k$ -ratio of InAlAs which is 0.29 – 0.5 [18].

2. The effective  $k$ -ratio of all three structures is slightly higher than measurements on SACM APDs with a multiplication layer thickness corresponding to the intrinsic layer thickness in the PIN diode case. For 200 nm thick InAlAs layer a  $k$ -ratio of 0.18 [44] is expected. For a 150 nm layer thickness the  $k$ -ratio drops down to 0.15 [45, 53].
3. PIN-110 nm has the smallest effective  $k$ -ratio of all three devices. This is consistent with our expectations that non-local impact ionization in thin multiplication regions improves the  $k$ -ratio.
4. PIN-220 nm has a higher  $k$ -ratio than PIN-505 nm which can be attributed to an increased  $k$ -ratio at low electric fields [55].

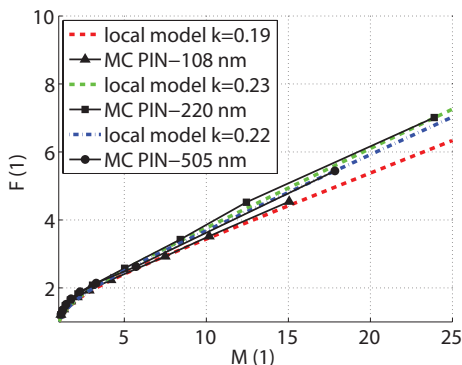


Figure 6.10: Simulated multiplication excess noise factor  $F$  for electron induced impact ionization.

The excess noise factor for a multiplication gain  $M = 10$  vs. the thickness of the depletion layer is presented in Fig. 6.11(a). The result is compared with measurement on InAlAs PIN-diodes from [55] with slightly different thickness. First of all, we note that the discrepancy in the excess noise factor with measurements is small ( $< 10\%$ ). The measurement shows that the excess noise factor indeed drops for thicker intrinsic regions. However, the MC simulations predict the maximal excess noise somewhere between 220 nm and 505 nm

while measurements show this drop between 550 nm and 1060 nm. The excess noise factor decreases for device PIN-220 nm-B and PIN-220 nm-C compared to PIN-220 nm. The multiplication gain is only slightly modified as shown in Fig. 6.11(b). In the PIN-220 nm device the electric field has its peak on the p-side of the depletion region (see Fig. 6.6). This peak coincides with a large amount of available secondary holes which leads to an amplification of the hole induced impact ionization events. On the other hand the electric field is lower on the n-side which reduces the amount of impact ionization by electrons. In contrast, the electric field in the PIN-220 nm-C diode is maximal on the n-side of the depletion layer. Therefore, electron induced impact ionization event at the n-side are amplified at the cost of hole impact ionization events on the p-side. According to our simulation the PIN-220 nm-C has a 5.8 % smaller excess noise factor than PIN-220 nm for a multiplication gain of  $M = 10$ .

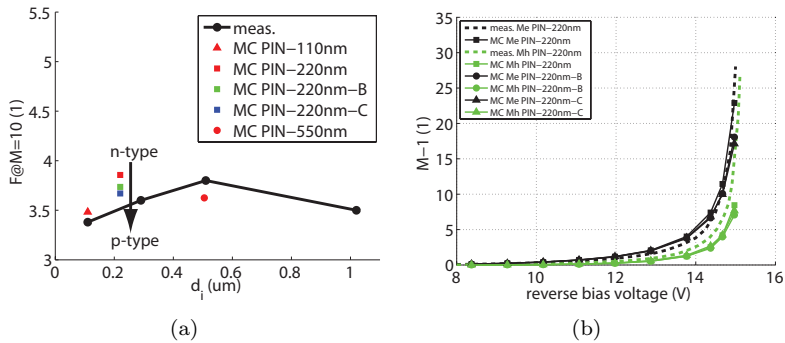


Figure 6.11: InAlAs PIN diode (a) simulated excess noise factor for a multiplication gain of ten for various thickness of the intrinsic region in comparison with measurements [55], (b) multiplication gain vs. reverse bias voltage for PIN diodes with different types of unintentional background doping of the intrinsic region.



# Chapter 7

## APD Simulation Results

This chapter presents simulation results for the APD structure presented in Sec. 3.1. Drift-diffusion (DD) simulations are performed to extract the fabricated doping profile from capacitance vs. voltage measurements. The electric field profile obtained by this simulation are used as initial condition for the following MC simulations. The frozen field MC (FFMC) approach is used to investigate two cases. In the first case, the hetero-junction band diagram energy offset is neglected ( $\Delta E_{C,V} = 0 \text{ eV}$ ). In the second case, the hetero-junction band diagram energy offset is included ( $\Delta E_{C,V} \neq 0 \text{ eV}$ ). The FFMC simulations are used to obtain the multiplication gain, the excess noise factor, the transit time and the impact ionization position. Finally, the self-consistent MC (SCMC) simulations are used to compute the carrier energy and velocity profiles.

### 7.1 Capacitance vs. Voltage

#### 7.1.1 Introduction

The capacitance is defined as the incremental increase in charge  $dQ$  upon an incremental change of the applied voltage  $dU$  [17],  $C = dQ/dU = A\epsilon/d$ , with  $A$ , the device diameter,  $\epsilon = \epsilon_s\epsilon_0$  the static dielectric constant and  $d$  the thickness of the depletion layer width. A common simplification is the assumption of sudden depletion layer

boundary and rectangular shaped space charge regions. The spatial resolution of the differential capacitance technique is in the orders of the Debye length [17,128]. In particular, the space charge in presence of hetero-junctions requires additional attention [129]. Without corrections, the doping profile resulting from CV-profiling appears to be heavily graded.

In this work we use a self-consistent drift-diffusion simulator [116] to compute the depletion layer width at each bias point. This allows to resolve the shape of the space charges on hetero-junctions, to compute the non-linear effect of space charge on the electric field and the growth of the depletion region width. A small signal AC-analysis [116] is performed to extract the device capacitance. In [130] an algorithm is presented which allows to extract the exact doping profile and hetero-junction offsets by means of inverse CV-simulations based on a drift-diffusion transport model.

### 7.1.2 CV-Fit

In the following we will investigate device A, B and C (see Sec. 3.1), based on two possible doping profiles, fit I (FI) and fit II (FII). Each doping profile is determined from CV-measurement of the corresponding device. A multitude of different configurations between layer thickness and doping exists for the same CV-measurement. We chose two configurations which are most probable from our point of view. Fabrication specifications allow a deviation of the layer thickness and doping of  $\pm 5\%$  during fabrication. Furthermore, diffusion of p-dopants from the field control layer can not be excluded. We have to deal with an uncertainty with respect to the value of the dielectric constant in literature which may significantly influence the fit of the CV-characteristic. Values found in literature are summarized in App. F. We use  $\epsilon_s = 12.46$  [62] for InAlAs and  $\epsilon_s = 13.1$  [119] for InGaAs.

The two configurations for layer thickness and doping which are investigated in this work are summarized in Tab. 7.1 and 7.2. The corresponding values for the fringe capacitance  $C_b$  are given in Tab. 7.3. Please note, that for the fit of device C the parasitic capacitance resulting from substrate conductance are included (see Sec. 4.3.2).

Additional information on the doping profile which could improve the precision of the device structure extraction can be obtained by other measurement methods such as secondary ion mass spectrometry (SIMS).

layer	thickness (nm)			doping ( $1/\text{cm}^3$ )		
	I	II	III	I	II	III
#3	400			n: $7 \cdot 10^{18}$		
#4	200			n: $5 \cdot 10^{18}$		
#5	188, -6 %	143, -4 %		p: $1 \cdot 10^{15}$		
#6	142, -4.6 %			p: $2.68 \cdot 10^{17}$ , +16.5 %	p: $3.08 \cdot 10^{17}$ , +23.2 %	p: $2.65 \cdot 10^{17}$ , +15.2 %
#7	50			p: $1 \cdot 10^{16}$		
#8	950, -5 %	520, -5.5 %		p: $6 \cdot 10^{14}$		
#9	50			p: $5 \cdot 10^{15}$		
#10	400			p: $3 \cdot 10^{18}$		
#11	100			p: $1.4 \cdot 10^{19}$		

Table 7.1: Epitaxial structure FI from CV-measurement and the variation with respect to the specified value.

### Structure FI

For device A and B the structure of FI assumes a diameter of  $41 \mu\text{m}$  and  $19.4 \mu\text{m}$  for device C. This is a good estimation based on light microscope images of the structure [30]. Due to the mesa shape of the structure the diameter of the initial junction is significantly larger than the active diameter of the APD which is  $32 \mu\text{m}$ . We neglect the decrease of the diameter on the p-side of the depletion region for increasing reverse bias voltage which results from the mesa shape of the APD. In order to fit the zero volt capacitance the effective thickness of the depletion layer must be smaller than specified. Under the assumption that the fabrication results in slightly thinner layers and diffusion of dopants into the multiplication layer a good fit for the zero volt capacitance can be achieved by preserving a realistic

layer	thickness (nm)			doping ( $1/\text{cm}^3$ )		
	I	II	III	I	II	III
#3	400			n: $7 \cdot 10^{18}$		
#4	200			n: $5 \cdot 10^{18}$		
#5	200		150	n: $1 \cdot 10^{14}$		
#6	150			p: $2.43 \cdot 10^{17}$ , +5.65 %	p: $2.8 \cdot 10^{17}$ , +12.0 %	p: $2.45 \cdot 10^{17}$ , +6.52 %
#7	50			n: $1 \cdot 10^{14}$		
#8	1000		550	n: $1 \cdot 10^{14}$		
#9	50			n: $1 \cdot 10^{14}$		
#10	400			p: $3 \cdot 10^{18}$		
#11	100			p: $1.4 \cdot 10^{19}$		

Table 7.2: Epitaxial structure FII from CV-measurement and the variation with respect to the specified value.

value of the capacitance for the fully depleted device. The doping concentration of the field control layer (#6) is selected to fit the slope of the CV-characteristic and the measured punch-through voltage (see Fig. 7.1(b)). The deviation of the doping concentration in the field control layer (#6) is in the orders of 15 % to 25 % compared to the specified value while the thickness of the layer is about 5 % thinner than specified. The specified deviation of the doping concentration is only 5 %. However, considering diffusion effects and the difficulty to produce a high doping layer in between two intrinsic regions, makes such a deviation reasonable.

### Structure FII

The structure of FII assumes fix layer thickness, according to the specifications and no diffusion. This assumption is based on the potentially high precision of MBE growth technology with respect to layer thickness. To fit the zero volt capacitance and preserve a realistic value for the fully depleted device the diameter needs to be slightly larger than FI, 42  $\mu\text{m}$  for device A and B. For device C a diameter of 19  $\mu\text{m}$  is selected. The doping of the field control layer is chosen to

device	$C_b$ for FI (fF)	$C_b$ for FII (fF)	$d$ FI ( $\mu\text{m}$ )	$d$ FII ( $\mu\text{m}$ )
A	47	49	41	42
B	47	47	41	42
C	30 / 255	49 / 255	19.4	19.0

Table 7.3: Values for fringe capacitance  $C_b$  and device diameter  $d$  for FI and FII. Device C includes the parasitic capacitance due to the substrate conductance.

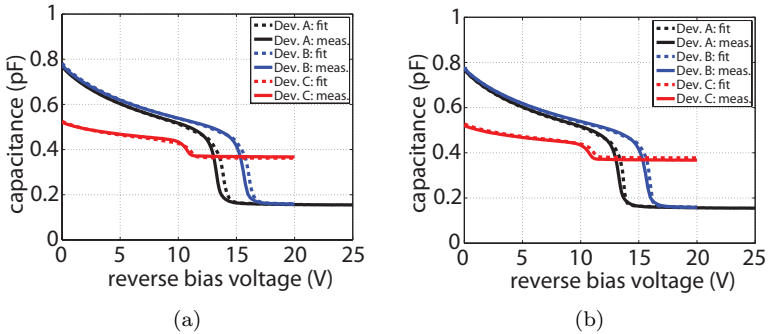


Figure 7.1: Capacitance vs. voltage fit for (a) FI, (b) FII.

fit the CV-characteristic and punch-through voltage (see Fig. 7.1(b)). The resulting doping concentration of the field control layer for FII is significantly smaller than FI. This results in a significantly smaller field separation between multiplication layer and absorber layer.

## 7.2 FFMC Computation Time

The computation time for the FFMC APD simulations strongly depends on the multiplication gain  $M$ . The simulation results presented in this work are obtained for  $N_{\text{initial}} = 2.4 \cdot 10^4$  initial electron-hole pairs for each bias point. The amount of final carriers is  $M$ -times larger. Each bias point is computed on 12 CPUs (2.3GHz AMD

Opteron) in parallel. In the high gain regime above  $M = 10$  the task is distributed on 24 CPUs. The time required for the simulation with  $\Delta E_{C,V} = 0 \text{ eV}$  is between 4h-14h depending on the multiplication gain. For the simulation with  $\Delta E_{C,V} \neq 0 \text{ eV}$  the simulation time can be considerable larger due to multiple reflection of carriers on the hetero-junction. For a  $M = 10$  the same simulation can take up to 21 h.

## 7.3 FFMC w/o Band Diagram Offset

In a first approximation, we neglect any band diagram offsets in the FFMC approach,  $\Delta E_{C,V} = 0 \text{ eV}$ . The mean time carriers require to cross the device is underestimated in this scheme because reflections on hetero-junctions occur very seldom. This approach does not influence the impact ionization in the current APD devices. The hetero-interface is far away from the high field region and does not alter the carrier energy distribution in the multiplication region. However, analysis of impact ionization engineered multiplication layers requires band diagram offset treatment. The FFMC simulation procedure is explained in Sec. 5.4.7. The presented results are for the case of front-side illumination of the APD.

### 7.3.1 Gain vs. Voltage

Fig. 7.2 presents multiplication gain vs. reverse bias voltage for device A, B and C for the two possible configurations FI and FII. The agreement in terms of breakdown voltage is good for FI. However, the multiplication gain below  $M = 10$  is slightly underestimated. For device B, the multiplication gain below 20 V is too large. The breakdown voltage for FII is up to 20% higher. This illustrates the very high sensitivity of the field control layer doping on the actual breakdown voltage.

### Effect of Field Control Layer Doping

After punch-through the difference in the electric field amplitude from the multiplication layer to the absorber layer remains constant (see

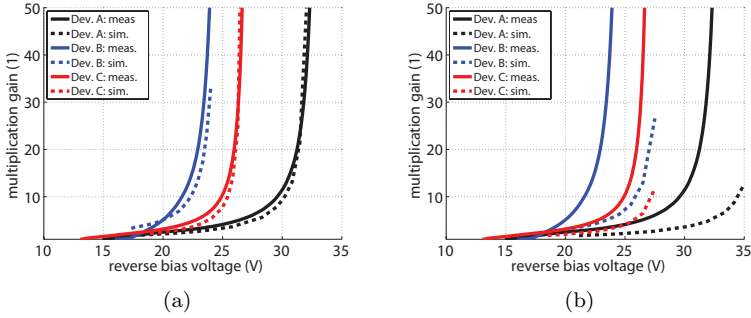


Figure 7.2: Multiplication gain vs. reverse bias voltage (a) FI, (b) FII.

Fig. 2.6). Any additional reverse bias voltage applied to the device is evenly distributed over the entire width of the depletion region. The slightly thinner multiplication layer thickness of FI and slightly higher field control layer doping result in a slightly higher electric field in the multiplication layer for the same applied voltage. Since the impact ionization rate has approximately an exponential dependence on the electric field (see Eq. 2.1 and Eq. 2.2), small changes in the electric field result in a strong leverage with respect to the breakdown voltage.

### Effect of Reduced Depletion Region Width

The electric field increases more significantly for FI compared to FII for increasing reverse bias voltage due to the approximately 5% thinner total depletion layer width of FI.

### Effect of Absorber Background Doping

Background doping of the absorber region has an impact on the electric field profile within the entire APD device. A p-type background doping confines the potential drop around the multiplication region. A n-type background doping results to an increased electric field on the p-side of the absorber region and results in a slightly lower electric field in the multiplication layer.

In both cases it is preferable to keep unintended impurities low. High p-type background doping results in a high electric field at the boundary between field control and absorber region which can result in increased band-to-band-tunneling and dark current. A high n-type background doping may result in undesired impact ionization on the p-side of the absorber region which can strongly reduce the device bandwidth [34]. An exception for which high p-type background doping is desired are NA-APD structures (see Sec. 2.9.3).

### 7.3.2 Multiplication Excess Noise

#### Effective $k$ -ratio

Fig. 7.3 presents the simulation results for the excess noise parameter  $F$  for FI and FII. Based on local theory (see Sec. 2.7) it is possible to attribute an effective  $k$ -ratio to the simulation results for each structure. The effective  $k$ -ratio is higher than expected from literature,  $k = 0.18$  for 200 nm [44] and  $k = 0.15$  for 150 nm [45]. The effective  $k$ -ratio is larger than the effective  $k$ -ratio obtained for PIN-diodes in Sec. 6.2.2.

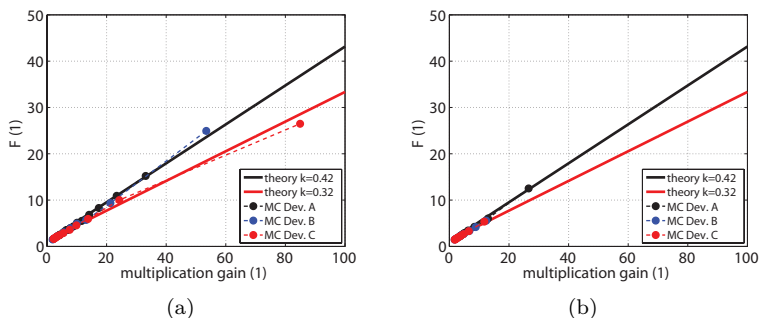


Figure 7.3: Excess noise factor vs. multiplication gain (a) FI, (b) FII.

### $k$ -ratio vs. Multiplication Region Thickness

First of all, device A and B show similar effective  $k$ -ratios since both have similar multiplication layer shape. Device C shows a smaller  $k$ -ratio which can be explained by non-local effects which amplifies electron impact ionization with respect to hole impact ionization. We will discuss this effect in Sec. 7.3.3. Both configurations, FI and FII, show nearly similar results.

## 7.3.3 Impact Ionization Profile

### Electron Injection Structure

The position of the impact ionization events are presented in Fig. 7.4(a) for device A (FI) and in Fig. 7.4(b) for device C (FI). The characteristic for device B is very much the same as for device A. Furthermore, the profile does not differ significantly between FI and FII. We observe that electron impact ionization events happen more often than hole induced impact ionization events. This illustrates the higher electron impact ionization rate of the InAlAs material (see Sec. 6.1.3) and the electron injection structure of this APD. Furthermore, the amount of electron induced impact ionization events increases towards the n-side of the multiplication region. This is due to the increased number of electrons available on the n-side.

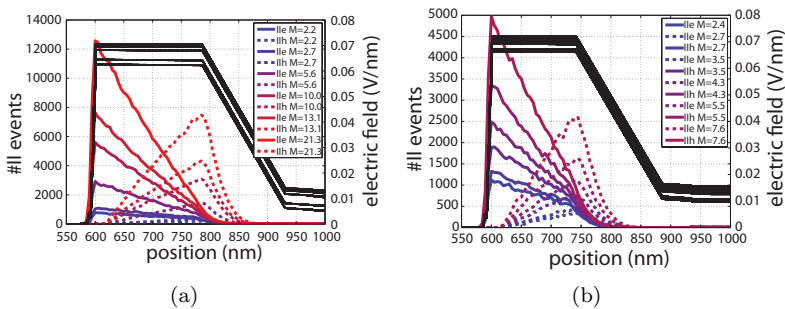


Figure 7.4: Number of impact ionization events (a) device A FI, (b) device C FI.

### Dead-Space Effects

For the hole induced impact ionization events the dead-space effect is clearly visible around 600 nm. The majority of the electron induced impact ionization events happen there, so a significant amount of holes is present. However, a distance of approximately 20 nm is required to create a first hole induced impact ionization event. Prior to that point, holes can not achieve enough energy. The dead-space decreases for increasing electric field. Furthermore, significant impact ionization outside the field control layer can be observed which is the result of a large amount of holes at high gain, significant electric field in the field control layer as well as an overheated hole energy distribution entering that region. This makes the effective multiplication region wider than the actual multiplication layer thickness. This non-local effects have considerable effect in particular for very thin multiplication regions.

### Dead-Space Effects vs. Excess Noise Factor

For device C in Fig. 7.4(b), the dead-space for holes is more important with respect to the thickness of the multiplication layer compared to device A and B. For the same multiplication gain, the position of the impact ionization events is more confined and therefore more deterministic which reduces the excess noise factor.

## 7.3.4 Carrier Arrival Time

### Impulse Response

The carrier arrival time refers to the time an initial optically generated electron-hole pair requires to travel across the entire depletion region and to enter its corresponding majority region. For that purpose each carrier is assigned a time since the optical generation event at  $t = 0$  ps. The time is updated in each simulation step. If one of the initial carrier is creating a new electron-hole pair by means of impact ionization this time is passed to its children. If any carrier leaves the depletion region, the time the carrier spend in the depletion region is recorded. As explained in Sec. 5.4.7 this experiment is repeated until sufficient statistics are acquired. The resulting histogram ( $\Delta t = 1$  ps) of the arrival times in all experiments corresponds to a number of carriers

crossing the depletion region boundary within a given unit time. This measure is proportional to a electron or hole current,  $J_n$  and  $J_p$  with an arbitrary unit (a.u.). The total current  $J = J_n + J_p$  (a.u.) over time corresponds to a response of the system to an ensemble of optical generation events at  $t = 0$  ps, distributed over the absorptive part of the device. Therefore, we interpreted this current being proportional to the impulse response to an optical generation pulse. The electron response at the n-side of the depletion region and hole response at the p-side of the depletion region are shown in Fig. 7.5 for device A, in Fig. 7.6 for device B and in Fig. 7.7 for device C.

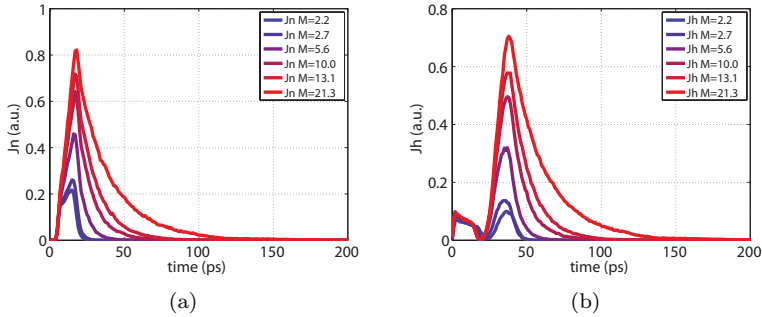


Figure 7.5: Arrival time distribution of carriers at the boundary of the depletion region for device A (FI) and  $\Delta E_{C,V} = 0$  eV (a) electrons on n-side of depletion region, (b) holes on p-side of the depletion region.

### Primary and Secondary Response

For the electron response we can see that the first carriers arrive after only a few ps. This corresponds to the minimal transit time of electrons created on the n-side of the absorber region. The optical generation profile is such that the majority of the optical generation events happen on the p-side of the absorber. Therefore, we see an increase of the electron response over time at low gain up to about 20 ps (see Fig. 7.5(a) and Fig. 7.6(a)). For device C in Fig. 7.7(a) this time is smaller due to the thinner layer thickness. For increasing

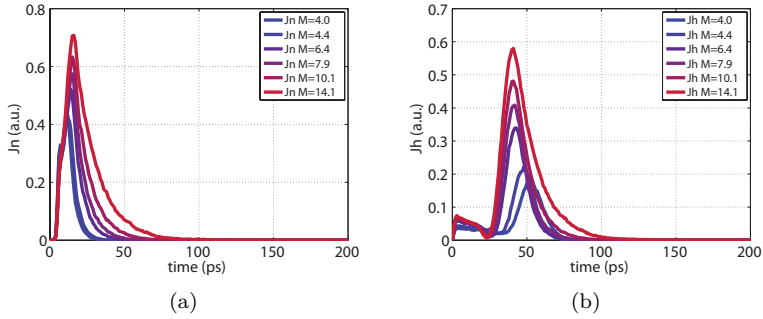


Figure 7.6: Arrival time distribution of carriers at the boundary of the depletion region for device B (FI) and  $\Delta E_{C,V} = 0$  eV (a) electrons on n-side of depletion region, (b) holes on p-side of the depletion region.

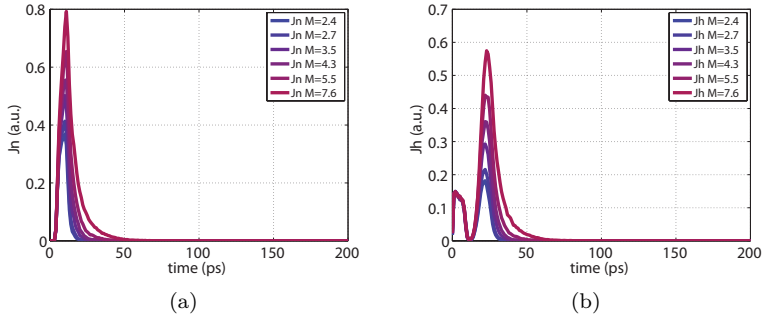


Figure 7.7: Arrival time distribution of carriers at the boundary of the depletion region for device C (FI) and  $\Delta E_{C,V} = 0$  eV (a) electrons on n-side of depletion region, (b) holes on p-side of the depletion region.

multiplication gain additional electrons are created within the multiplication region and leave this region with a time delay according to the avalanche-build up time. The amplitude of the electron response increases and the peak of the response is delayed. A characteristic tail in the impulse response appears which increases for higher gain.

The hole response is divided in a primary and secondary response (see Fig. 7.5(b), Fig. 7.6(b) and Fig. 7.7(b)). Primary holes are created due to optical absorption and secondary holes are created by means of impact ionization in the multiplication layer. The primary response is influenced by the optical generation profile. The secondary response shows response tails similar to the electron response. We can identify transport of secondary holes being the principle time limiting mechanism at low gain. At high gain, the secondary hole response is additionally delayed by the avalanche build-up time. This illustrates the transition from a transit time limit to an avalanche build-up time limit.

### Slow Response of Device B

Particularly interesting is the secondary hole response of device B in Fig. 7.6(b). At low gain a delayed response of the secondary holes can be observed compared to the response at higher gain. This is caused by a low electric field in the absorber region of device B at low gain. Due to that, holes travel below their saturation velocity. This simulation results confirm our analysis of the measurement presented in Sec. 4.3.3. The analysis related the low bandwidth of device B to the mobility of holes at low electric fields. Furthermore, we neglect the effect of optically generated carriers on the electric field. This effect may influence the characteristic of device B (see Sec. 4.3.6).

### 7.3.5 Gain-Bandwidth Characteristics

The total response  $J$  is used to extract the transit time limited  $-3$  dB bandwidth of the APD by transforming the signal into frequency space by means of a Fourier transform. The  $-3$  dB bandwidth corresponds to the frequency for which the signal power drops to half of its DC value. The bandwidth vs. multiplication is shown in Fig. 7.8 for device A, Fig. 7.9 for device B and Fig. 7.10 for device C, for both FI and FII. The simulations are compared to the measured gain-bandwidth characteristics obtain in Sec. 4.3.3. For the original as well as the RC-corrected gain-bandwidth characteristic an average of the three measurements is taken.

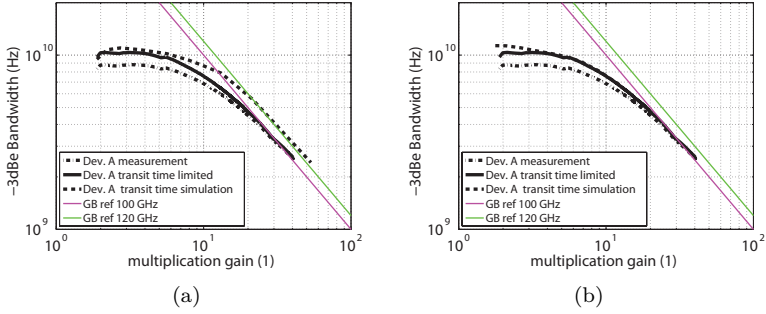


Figure 7.8: Bandwidth vs. gain for device A and  $\Delta E_{C,V} = 0$  eV (a) FI, (b) FII.

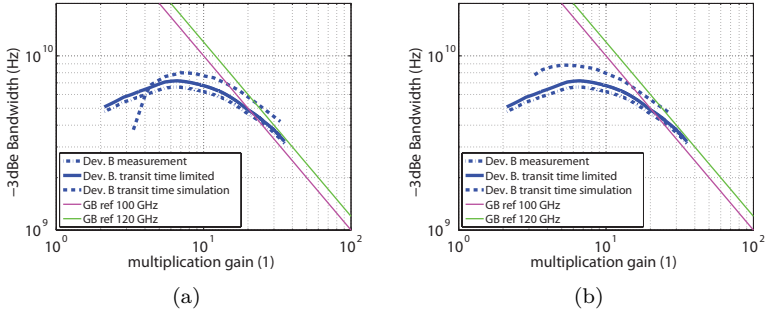


Figure 7.9: Bandwidth vs. gain for device B and  $\Delta E_{C,V} = 0$  eV (a) FI, (b) FII.

In general, the simulations describe accurately the transition from a transit time limited to an avalanche build-up time limited regime. We observe a tendency to overestimate the device bandwidth. We identify three possible reasons for that:

- The overestimation of the saturation velocity for electron and holes in InAlAs. This effect should be negligible in the transit time limit where secondary hole transport in InGaAs is the

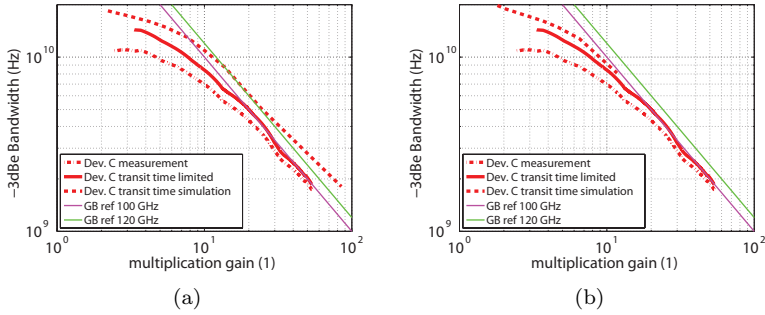


Figure 7.10: Bandwidth vs. gain for device A and  $\Delta E_{C,V} = 0$  eV (a) FI, (b) FII.

major bandwidth limiting mechanism. However, the avalanche build-up limit can be affected by this overestimation of the carrier velocities.

- In the presented simulation  $\Delta E_{C,V} = 0$  eV. Including the band diagram offsets, reflection of carriers at hetero-interfaces becomes more common which increases the overall transit time of this carriers. This mechanism affects mainly the low gain regime due to the overall lower carrier energies and should be negligible at high gain. We will investigate this effect in Sec. 7.4.
- For device B, the electric field within the absorber may be influenced by the optical generation rate which is ignored in the FFMC approach.

Nevertheless, the agreement between simulated and measured bandwidth for device A and C is quite good. The difference between FI and FII is small. In both cases carriers travel at their saturation velocity. Therefore, the transit time is nearly the same.

For device B the bandwidth decreases at low gain which corresponds quite well to measurement result. As shown for the impulse response, this effect is caused by hole transport below their saturation velocity. The effect is more pronounced for FI due to the larger field

separation compared to FII. Hence, the electric field in the absorber is smaller for the same multiplication gain.

## 7.4 FFMC with Band Diagram Offset

In this extended FFMC analysis, sudden band diagram offsets are included, meaning  $\Delta E_{C,V} \neq 0$  eV. Occasionally, carriers are reflected at a hetero-interface. In the FFMC a charge pile up at the hetero-interface does not influence the electric field. It has been claimed, that at high fields band distortion due to charge pile up are not significant [102].

At low electric fields, a small amount of carriers will remain at the hetero-junction. These carriers are mainly holes at the p-side of the absorber layer which may have a very small kinetic energy. The tunneling probability of holes is low due to their high effective carrier mass and the moderate electric field. In absence of carrier-carrier, carrier-plasmon scattering and electric field update, they require a series of phonon absorption events in absence of any phonon emission to overcome the hetero-junction. This is very unlikely to happen. We assume that they would recombine within the long time they remain on the interface. Therefore, we are artificially truncating the simulation time at 200 ps.

We only analyze device A, B and C for the FI structure. No significant difference in the impact ionization profile can be found compared to the FFMC results with  $\Delta E_{C,V} = 0$ . This is not surprising, since the hetero-interfaces between absorber, grading and field control layer are sufficiently far away from the multiplication layer. They do not influence the energy distribution within the multiplication layer.

### 7.4.1 Carrier Arrival Time

The carrier arrival time distribution is influenced by  $\Delta E_{C,V} \neq 0$ . The results are shown in Fig. 7.11 for device A, in Fig. 7.12 for device B and in Fig. 7.13 for device C. The response shows an additional time delay caused by multiple reflection of charge carriers on the hetero-junction energy barriers. The form of the electron and hole response is smoother.

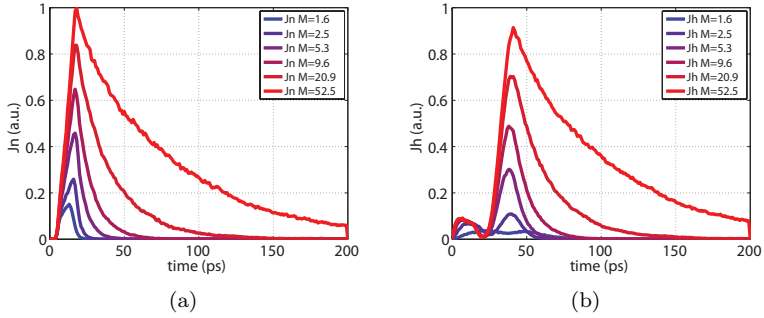


Figure 7.11: Arrival time distribution of carriers at the boundary of the depletion region for device A (FI) and  $\Delta E_{C,V} \neq 0$  eV (a) electrons on n-side of depletion region, (b) holes on p-side of the depletion region.

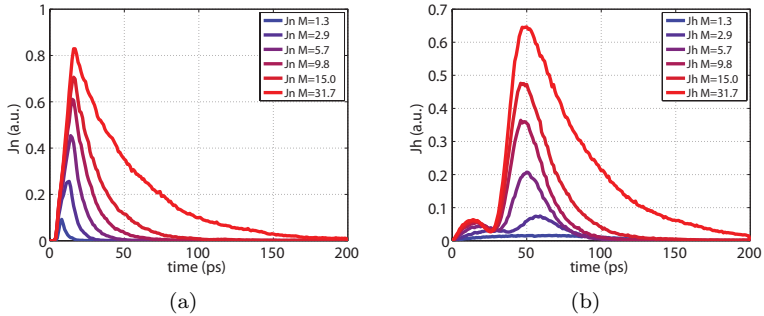


Figure 7.12: Arrival time distribution of carriers at the boundary of the depletion region for device B (FI) and  $\Delta E_{C,V} \neq 0$  eV (a) electrons on n-side of depletion region, (b) holes on p-side of the depletion region.

The effect is pronounced for holes at low gain in device B and to some extent for device A. At low multiplication gain, the amplitude of the electric field at the hetero-junction at the p-side of the absorber

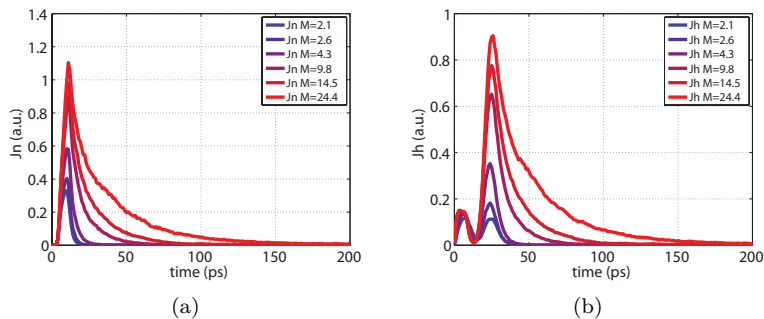


Figure 7.13: Arrival time distribution of carriers at the boundary of the depletion region for device C (FI) and  $\Delta E_{C,V} \neq 0$  eV (a) electrons on n-side of depletion region, (b) holes on p-side of the depletion region.

in device B is not very high. Some holes do not obtain sufficient kinetic energy to overcome the hetero-junction barrier. In contrast, electrons are not particularly delayed. This results suggest that special care needs to be taken for hetero-junctions, delaying hole transport. A mole fraction grading is a possible solution. However, we do not observe any indication from the measurements, that the hole pile-up is a time limiting factor in device B (see Sec. 4.3.6). We conclude that hole-pile up is overestimated in our simulations at low electric fields. This could partially be caused by missing carrier-carrier and carrier-plasmon interaction.

## 7.4.2 Gain-Bandwidth Characteristics

The delayed hole response translates into a lower device bandwidth at low multiplication gain for device A and B (see Fig. 7.14 and Fig. 7.15) compared to the simulation with  $\Delta E_{C,V} = 0$ .

However, the agreement with measurement is quite good. For device A in Fig. 7.14, the point for highest gain around  $M = 50$  deviates from measurement due to the artificial truncation of the simulation time at 200 ps, cutting some of the slow response tail (see

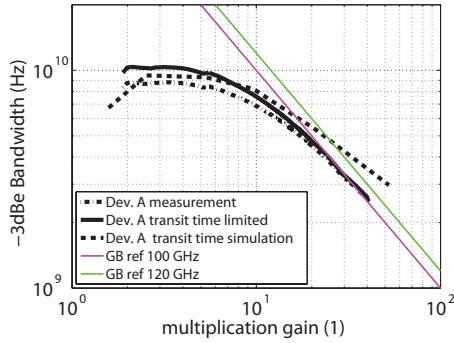


Figure 7.14: Bandwidth vs. gain with  $\Delta E_{C,V} \neq 0$  eV for device A (FI)

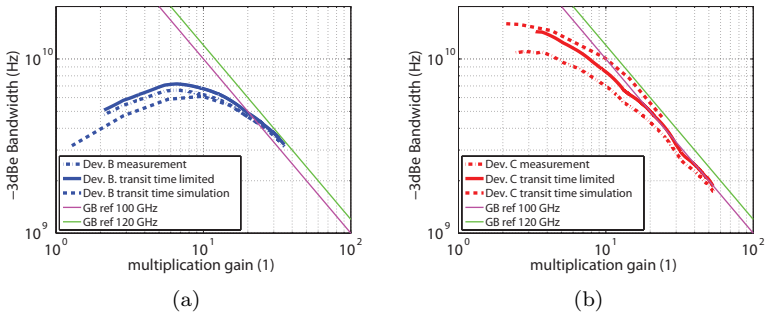


Figure 7.15: Bandwidth vs. gain with  $\Delta E_{C,V} \neq 0$  eV for (a) device B (FI), (b) device C (FI)

Fig. 7.11). For device B, the bandwidth is underestimated at low gain which we relate to an overestimated hole pile up at low electric fields.

## 7.5 SCMC

### 7.5.1 General Remarks

In the following we are going to discuss the simulation results for steady-state, SCMC for device A and B in the FI configuration. We limit ourself to two bias point each, one at low gain and one at high gain. We include results for  $\Delta E_{C,V} = 0\text{eV}$  (full line) and  $\Delta E_{C,V} \neq 0\text{eV}$  (dashed line). This makes it possible to interpret the difference between the FFMC results for this two cases. In general, the results with and without  $\Delta E_{C,V}$  differ mainly around the hetero-junction itself. The self-consistent electric field within the depletion region are in both cases the same.

We refer to the mean velocity of the carriers as the velocity in the main transport direction, which is in our case the left-to-right (or positive z-direction) for holes and right-to-left (or negative z-direction) for electrons.

The algorithm creates new electron-hole pairs according to the optical generation rate in each simulation step. The minority electron density entering the absorber region from the p-side buffer is overwhelmed by the optically generated electron density in the absorber. The electron mean values are dominated by this optically generated electrons. We assume that these electrons start with zero kinetic energy at the bottom of the  $\Gamma$ -valley. Holes start at the bottom of the HH-valley. However, the mean value for holes is dominated by the secondary holes created by impact ionization. In steady-state, for each primary hole in the absorber,  $M - 1$  secondary holes exist. This is an important aspect for the interpretation of the following mean value data.

### 7.5.2 Computation Time

One main advantage of the SCMC approach compared to the FFMC approach is the independence of the simulation time with respect to the multiplication gain  $M$ . A single bias point requires 8 h computation time on a single CPU (2.3GHz AMD Opteron). There is a huge potential in terms of parallization in future implementation of this simulator.

### 7.5.3 Device A

#### Electron Non-Equilibrium Transport on Hetero-Junctions

In Fig. 7.16 the mean kinetic energy and in Fig 7.17 the mean velocity of the electrons are shown. The mean kinetic energy of the electrons in the multiplication layer is around 0.6 eV (1). Therefore, the transport of the carriers is in the majority of the time well described by the non-parabolic band-structure approximation (see Sec. 5.1.3). We can identify non-equilibrium effects at the hetero-junction between absorber (#8), grading (#7) and field control (#6) (2). In presence of  $\Delta E_C$ , electrons lose a significant amount of kinetic energy by crossing the hetero-junction from layer #8 to layer #7 and from #7 to layer #6. Due to the high electric field, the carriers are accelerated and non-equilibrium velocity overshoot, similar to the characteristic shown in Fig. 5.3, can be observed. The velocity overshoot at the hetero-junction settles within few tens of nm due to the strong electric field in the field control layer. The mean electron velocity drops slightly in front of the hetero-junction which is the result of reflection of electrons at the hetero-junction contributing to the mean velocity with a negative sign.

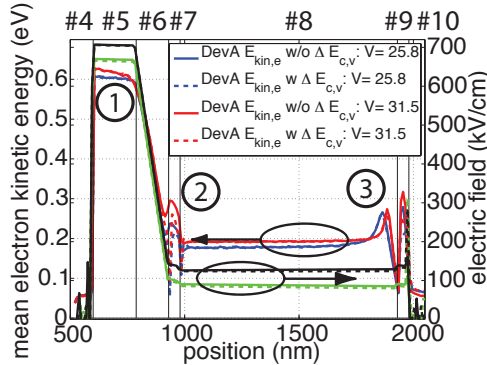


Figure 7.16: Steady-state electron mean kinetic energy for device A (FI). In green the electric field at  $V = 25.8$  V, in black the electric field at  $V = 31.5$  V

### Electron Non-Equilibrium Acceleration in Absorber

Non-equilibrium effects for electrons can be observed at the p-side of the absorber in Fig. 7.17 (3). Optically generated electrons starting at zero kinetic energy are accelerated by the electric field. These carriers show a significant velocity overshoot at the moment they start their journey, which exceeds the bulk velocity peak of approximately  $2 \cdot 10^7$  cm/s to  $3 \cdot 10^7$  cm/s (see Sec. 6.1.2). The mean electron velocity is elevated over several hundred of nanometers. The mean velocity settles to the saturation value as soon as the relaxed electrons are statistically overwhelming the newly generated electrons along the absorber region. Please note that the electron density on the n-side of the absorber is significantly higher than on the p-side side. Therefore, this velocity overshoot has only a small influence on the transient electron response in FFMC and is negligible in terms of total response because of the dominance of the secondary hole response. Similar to Fig. 5.3 the distance required to reach local equilibrium strongly depends on the electric field. At high electric field in the absorber the local equilibrium is reached over a smaller distance.

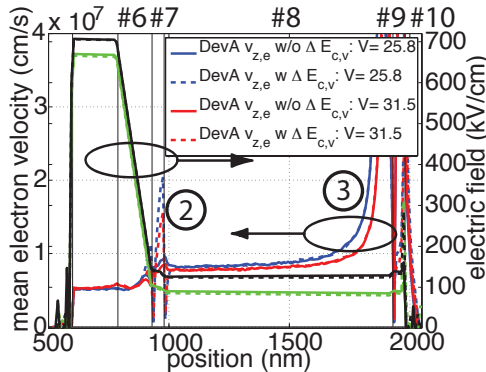


Figure 7.17: Steady-state electron mean kinetic velocity for device A (FI). In green the electric field at  $V = 25.8$  V, in black the electric field at  $V = 31.5$  V

## Hole Transport across Hetero-Junction

In Fig. 7.18 and Fig. 7.19 the mean kinetic energy of holes and the mean hole velocity are shown. As mentioned earlier, the mean values of holes is dominated by secondary holes. Therefore, no significant non-equilibrium effects, like for electrons, are observed in the absorber. At the hetero-junction between field control (#6), grading (#7) and absorber (#8) (4) an overshoot in the kinetic energy is observed which results from acceleration of holes by the energy gain at the band diagram offset.

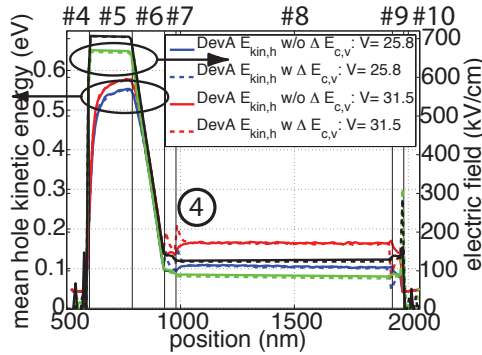


Figure 7.18: Steady-state hole mean kinetic energy for device A (FI). In green the electric field at  $V = 25.8$  V, in black the electric field at  $V = 31.5$  V

## Velocity Overshoot of Secondary Holes

At the p-side of the multiplication layer a velocity overshoot of holes can be observed (5). This overshoot results from secondary holes created by impact ionization which start at lower energy than the steady-state value for the same electric field. The hole velocity in the multiplication layer and the absorber settle to the bulk saturation velocity.

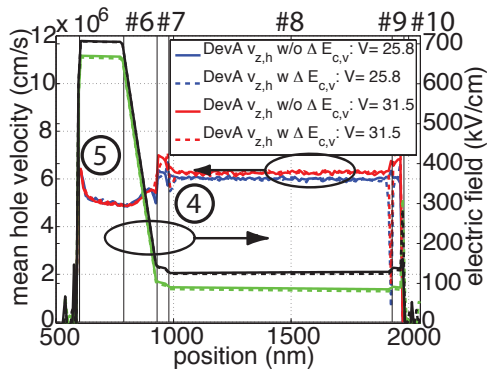


Figure 7.19: Steady-state hole mean kinetic velocity for device A (FI). In green the electric field at  $V = 25.8$  V, in black the electric field at  $V = 31.5$  V

### 7.5.4 Device B

The field separation in device B  $F(I)$  is much larger than for device A. This results in a significantly lower electric field in the absorber for the same multiplication gain which has already been subject to our analysis throughout this work. We will more deeply investigate how the low electric field modifies the mean velocities in device B. We can not directly compare the device A and B for the same multiplication gain. However, we choose a bias point with moderate and one with higher multiplication gain.

#### Low Field Acceleration in the Absorber

Due to the lower electric field in the absorber a significantly longer distance (6) is required for electron mean energy (see Fig. 7.20) and velocity (see Fig. 7.21) to settle to their saturation value compared to device A.

#### Electron Pile-up

A significant drop of the mean kinetic energy as well as of the mean electron velocity in front of the hetero-junction between absorber

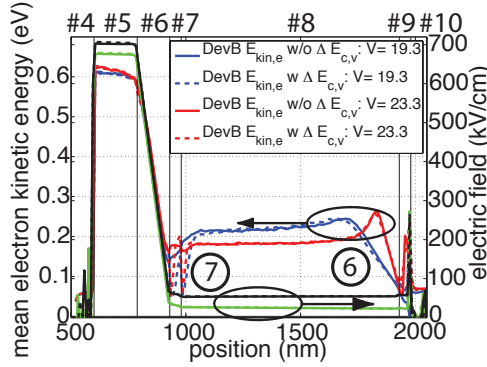


Figure 7.20: Steady-state electron mean kinetic energy for device B (FI). In green the electric field at  $V = 19.3\text{ V}$ , in black the electric field at  $V = 23.3\text{ V}$

(#8), grading (#7) and field control (#6) can be observed (7). This is due to amplified electron pile-up at this particular junction due to the lower electric field compare to device A.

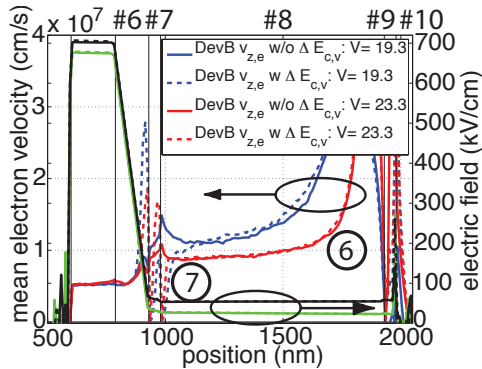


Figure 7.21: Steady-state electron mean kinetic velocity for device B (FI). In green the electric field at  $V = 19.3\text{ V}$ , in black the electric field at  $V = 23.3\text{ V}$

### Sub-Saturation Velocity Transport of Holes

At low bias, the holes in the absorber region (#8) of device B (8) are not at their saturation value with respect to the kinetic energy (see Fig. 7.22) and drift velocity (see Fig. 7.23). The hole velocity significantly increase for increasing bias voltage. This confirms our measurement results as well as our FFMC results.

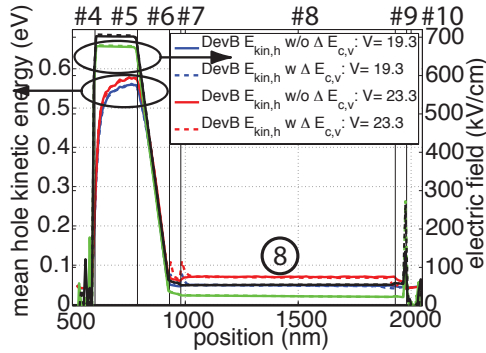


Figure 7.22: Steady-state hole mean kinetic energy for device B (FI). In green the electric field at  $V = 19.3$  V, in black the electric field at  $V = 23.3$  V

### Hole Pile-Up

Due to the hetero-junction on the p-side of the absorber (#8), grading (#9) and p-buffer (#10) hole pile-up can be observed which results in a significant drop of the mean velocity in this region.

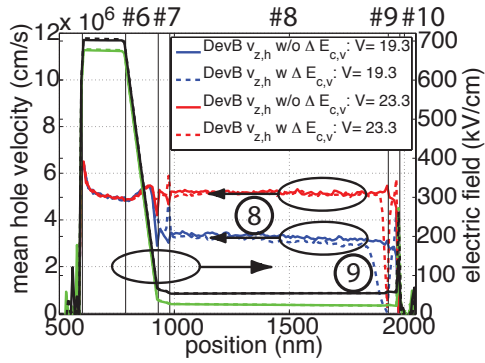


Figure 7.23: Steady-state hole mean kinetic velocity for device B (FI). In green the electric field at  $V = 19.3$  V, in black the electric field at  $V = 23.3$  V

## 7.6 Summary

A MC transport simulator for the analysis of non-equilibrium transport effects, such as velocity overshoots and non-local impact ionization has been implemented. The simulator is based on a spherical, non-parabolic band structure approximation. A future extension to full-band description is intended. This full-band extension is required to more accurately describe the high energy tail of the distribution function which is decisive for the physical description of the impact ionization process. In this work we modify the impact ionization model parameters to obtain a fit for the impact ionization rate in bulk between measurement and simulation. Doing so, we obtain good correspondence for the simulation of multiplication gain in PIN-diodes for various thickness of the intrinsic region.

Multiple techniques have been used to improve simulation speed to allow iterative design optimization of future APD, e.g. self-scattering reduction and multiple refresh. The FFMC approach allows analysis of multiplication gain, excess noise, impact ionization profile and impulse response. The SCMC simulator includes a Poisson update for self-consistent electric field computations and allows the analysis of steady-state carrier velocity and energy. The combination of this two methods allows to investigate performance critical physical effects within the APD structure.

The simulated structures have been obtained by fitting the measured CV-characteristic using a drift-diffusion simulator. The choice of the structure allows for some degree of freedom which can only be reduced by further measurements such as SIMS.

The correspondence of the gain-voltage characteristics with measurement is quite good. Excess noise is slightly overestimated compared to expectations. The simulated excess noise decreases for thinner multiplication layer which confirms the benefit of non-local impact ionization in thin structures. The simulated bandwidth vs. gain characteristic slightly overestimates the device bandwidth if heterojunction band diagram offsets are neglected. The device bandwidth is underestimated at low multiplication gain if these band diagram offsets are included.

Major findings with respect to the analysis of the device physics are

- A primary and secondary hole response can be observed. The simulation allows to quantify the influence of avalanche build-up time and transit time in the operation regime of the APD.
- Holes in the absorber of device B are not traveling at their saturation velocity. Compared to device A, which differs only in the field control layer doping, a lower maximal bandwidth results. This confirms previous measurement results.
- Simulations show that hetero-junction band diagram offsets are mainly influencing transit time of holes at low electric field. The offset leads to charge pile-up at the junction between absorber/grading and grading/buffer at the p-side of the absorber. This effect amplifies the bandwidth reduction in device B at low gain. However, our temperature dependent rise time measurements do not observe any effect which can be related to hole-pile up. Furthermore, the bandwidth reduction in our simulations is too large. This leads to the conclusion that hole-pile up at low electric fields is overestimated by our hetero-junction model. This discrepancy could be explained by missing carrier-carrier and carrier-plasmon scattering and requires further investigations.
- Simulations show the presence of impact ionization dead-space and non-local impact ionization effects. The effective width of the multiplication region is larger than the multiplication layer thickness.
- According to our simulation, transport of optically generated electrons in the InGaAs-absorber are influenced by non-equilibrium effects. The mean velocity on the p-side of the absorber exceeds the peak velocity for bulk material. This observation is made under the assumption that electrons created by optical generation start at the bottom of the  $\Gamma$ -valley with zero kinetic energy.
- Velocity overshoots are observed for electrons on hetero-junctions where they loose energy due to the band diagram offset. These overshoots do not influence the energy or velocity profile in the multiplication layer in our structure.



**Part III**

**Conclusion**



# Chapter 8

## Conclusion and Outlook

### 8.1 Conclusion

Two functional mesa InAlAs/InGaAs SACM APDs for 10 Gbit/s FTTH PON (device A and B) and one for 25 Gbit/s (device C) have been designed and characterized.

Device A and B have a breakdown voltage at  $T = 300$  K of  $V_{\text{br}} = 33.2$  V and  $V_{\text{br}} = 24.9$  V, respectively. The temperature coefficient of the breakdown voltage is  $\rho = 24.6$  mV/K for device A and  $\rho = 28.5$  mV/K for device B. Device C, with a thin multiplication layer of 150 nm, has a breakdown voltage of 27.0 V and a very small temperature coefficient of  $\rho = 12.8 - 16.8$  mV/K. The dark current in the operation regime is below 20 nA for an active diameter of 32  $\mu\text{m}$ . The activation energy of the dark current mechanism in the operation regime shows a strong impact of generation-recombination in the InGaAs absorber region. This dark current is created close to the surface of the mesa which is indicated by the linear relationship of the dark current with respect to the radius just after punch-through.

The maximal  $-3$  dB bandwidth is 8.9 GHz for device A and 6.7 GHz for device B. This bandwidth is mainly limited by the transit time of the carriers. The maximal bandwidth of device C is 11.8 GHz and is strongly influenced by a parasitic RC-component. The extracted transit time limited bandwidth of device C is 14.6 GHz. All three

devices show a gain-bandwidth product above 80 GHz. The high sensitivity of  $-27$  dBm at  $10$  GBit/s measured for a prototype receiver for device B, makes this APD eligible for the use in future  $10$  Gbit/s FTTH PON. Frequency and time domain measurements of device B show that the bandwidth is limited by holes in the absorber region which travel below their corresponding saturation velocity. This is a result of the high field separation between multiplication and absorber region.

A non-equilibrium transport simulator based on the MC method has been implemented. A spherical, non-parabolic band structure approximation with three conduction band and three valence band valleys is used. The FFMC approach allows the analysis of multiplication gain, excess noise, impact ionization profile and impulse response. The SCMC simulator includes a Poisson update for self-consistent electric field computation and allows the analysis of steady-state carrier velocity and energy profiles. The simulation results for multiplication gain and bandwidth show good agreement with measurements.

The impulse response quantifies the influence of the carrier transit time and the avalanche build-up time. The maximal bandwidth in the transit time regime is limited by secondary holes. The simulation results for device B confirm the effect of slow hole transport which has been observed in measurements. The simulations including the band diagram energy offsets at the hetero-junctions are slightly underestimating the device bandwidth, in particular at low electric fields. Non-equilibrium transport effects can be observed in proximity of the hetero-junctions where electrons and holes gain or lose energy by the band diagram energy offset. Electrons created by optical generation show significant velocity overshoot in the absorber region under the assumption that they start at the bottom of the  $\Gamma$ -valley.

This insight into device physics allows for quantitative optimization of future APD devices.

## 8.2 Outlook

Further work on the topic of design, characterization and simulation of APDs may include:

- An extension of the MC method using a full band structure for carrier dynamics and scattering is required. This is necessary for a more accurate description of the high energy tail of the distribution function which is important for the modeling of the impact ionization process.
- The effect of carrier-carrier and carrier-plasmon scattering on the transport across the hetero-junction band diagram offset needs to be investigated. This is motivated by the underestimated bandwidth in our simulation results, in particular at moderate electric fields.
- An extension to two dimensional real space transport would be interesting for the investigation of the electric field and impact ionization profile in lateral direction.
- Interesting topic of research is the analysis of the temperature dependence of avalanche multiplication gain.
- The SMC approach could be applied to the analysis of saturation effects in APD devices due to high optical input power or very high multiplication gain.
- From the design optimization point of view, the effect of super lattice and impact ionization engineered structures should be studied to improve the  $k$ -ratio of the avalanche multiplication process. The concept of NA-APDs should be investigated to achieve a 25 GHz transit time limited bandwidth.



# Appendix A

## MC Simulation Flow

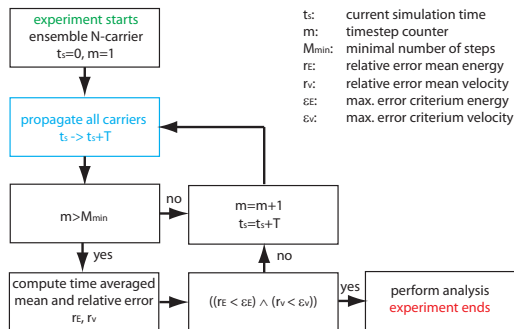


Figure A.1: Flowchart of a bulk MC simulation experiment.

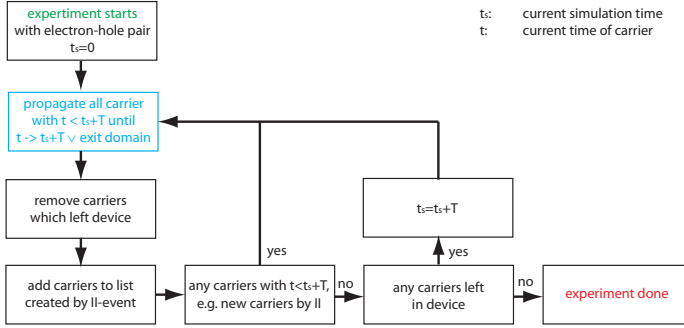


Figure A.2: Flowchart of a frozen field MC device simulation experiment.

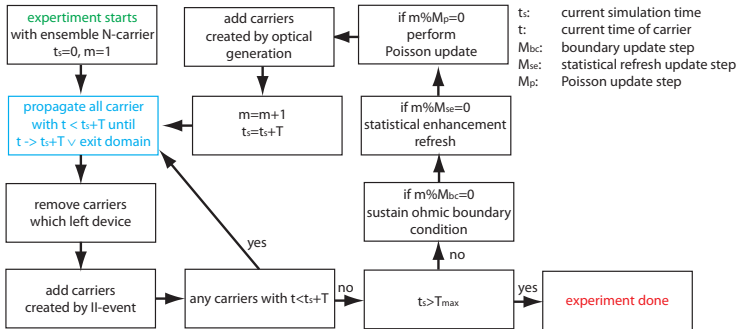


Figure A.3: Flowchart of a MC device simulation with Poisson update experiment.

# Appendix B

## Scattering Rate Formula

This chapter summarizes the scattering mechanism for the spherical non-parabolic band structure approximation.

### B.1 Polar Optical Phonon Scattering

The prefactor is given by [97]

$$P_{\text{pop}} = \frac{q^2 \sqrt{m^*} \omega_0}{4\pi \epsilon_0 \sqrt{2} \hbar} \left( \frac{1}{\epsilon_\infty} - \frac{1}{\epsilon_s} \right) \left( N_{\text{op}} + \frac{1}{2} \pm \frac{1}{2} \right). \quad (\text{B.1})$$

$q$  is the elementary charge.  $\omega_{\text{op}}$  is the optical phonon angular frequency.  $\epsilon_s$  and  $\epsilon_\infty$  are the static and high frequency dielectric constant of the material, respectively.  $N_{\text{op}}$  is the optical phonon occupation number. The scattering rate for electrons is [97]

$$\frac{1}{\tau_{\text{pop}}} = P_{\text{pop}} F_0(E, E') \frac{1 + 2\alpha E'}{\sqrt{\gamma}} \quad (\text{B.2})$$

with  $\gamma = E(1 + \alpha E)$ . The overlap factor  $F_0(E, E')$  is given in [97]. The final carrier energy for a intravalley absorption and emission process is  $E' = E \mp \hbar\omega_{\text{op}}$  with  $\hbar\omega_{\text{op}}$  being the optical phonon energy. For electrons this mechanisms acts as intravalley scattering mechanisms only. For holes the mechanisms acts as intra- and intervalley scattering mechanism. The overlap is computed according to [98].

## B.2 Non-Polar Optical Phonon Scattering

The prefactor is given by [80]

$$P_{\text{non-pop}} = \frac{D_{\text{non-pop}}^2 (m^*)^{\frac{3}{2}}}{\sqrt{2}\pi\hbar^3 \rho \omega_{\text{op}}} \left( N_{\text{op}} + \frac{1}{2} \pm \frac{1}{2} \right). \quad (\text{B.3})$$

$D_{\text{non-pop}}$  is the non-polar optical phonon scattering deformation potential.  $\rho$  is the mass density and  $\omega_{\text{op}}$  is the optical phonon angular frequency.  $N_{\text{op}}$  is the optical phonon occupation number. The scattering rate for absorption and emission is [80]

$$\frac{1}{\tau_{\text{non-pop}}} = P_{\text{non-pop}} \sqrt{\gamma'} (1 + 2\alpha E') \quad (\text{B.4})$$

with  $\gamma' = E'(1 + \alpha E')$ . The final carrier energy for intravalley absorption and emission process  $E' = E \mp \hbar\omega_{\text{op}}$  with  $\hbar\omega_{\text{op}}$  the optical phonon energy. For holes the mechanisms acts as intra- and intervalley scattering mechanism.

## B.3 Elastic Acoustic Phonon Scattering

The prefactor is given by [97]

$$P_{\text{el-ac}} = \frac{2 (m^*)^{\frac{3}{2}} k_{\text{B}} T D_{\text{acoustic}}^2}{2\pi\rho s_1^2 \hbar^4}. \quad (\text{B.5})$$

$D_{\text{acoustic}}$  is the acoustic deformation potential.  $m^*$  is the effective carrier effective mass.  $\rho$  is the mass density and  $s_1$  the longitudinal sound velocity. The scattering rate is [97]

$$\frac{1}{\tau_{\text{el-ac}}} = P_{\text{el-ac}} F_{\text{a}}(E) \sqrt{\gamma} (1 + 2\alpha E) \quad (\text{B.6})$$

with  $\gamma = E(1 + \alpha E)$ . We set  $F_{\text{a}}(E) = 1$ . For holes the mechanisms acts as intra- and intervalley scattering mechanism.

## B.4 Alloy Scattering

The prefactor for electrons is [62, 100]

$$P_{\text{alloy}} = \frac{3\pi}{8\sqrt{2}\hbar^4} (m^*)^{\frac{3}{2}} x(1-x)\Omega(D_{\text{alloy}})^2. \quad (\text{B.7})$$

$D_{\text{alloy}}$  is the interaction potential.  $m^*$  is the effective carrier effective mass.  $x$  is the molefraction and  $\Omega = a^3/4$  is the unit cell volume with  $a$  being the lattice constant. For holes the prefactor is implemented according to [101]

$$P_{\text{alloy}} = \frac{2^{\frac{3}{2}}}{2\pi\hbar^4} (m^*)^{\frac{3}{2}} x(1-x)\Omega(D_{\text{alloy}})^2. \quad (\text{B.8})$$

$m^*$  is the effective mass of the final valley. The scattering rate is [62, 100]

$$\frac{1}{\tau_{\text{alloy}}} = P_{\text{alloy}}\sqrt{E}(1+2\alpha E)S. \quad (\text{B.9})$$

$\alpha$  is the non-parabolicity of the valley and  $S$  being a parameter for the ordering of the alloy. We assume a completely random alloy  $S = 1$ . For holes the mechanisms acts as intra- and intervalley scattering mechanism.

## B.5 Impact Ionization

The impact ionization is implemented with a Keldysh model and a hard threshold condition [86]. For an carrier energy  $E$  smaller than the threshold energy  $E < E_{\text{th,Keldysh}}$  the scattering rate due to impact ionization is

$$\frac{1}{\tau_{\text{II}}} = 0. \quad (\text{B.10})$$

For an energy larger than the hard threshold energy  $E \geq E_{\text{hard,Keldysh}}$

$$\frac{1}{\tau_{\text{II}}} = \infty. \quad (\text{B.11})$$

For an energy larger than the threshold energy and smaller than the hard threshold energy  $E_{\text{th,Keldysh}} \leq E < E_{\text{hard,Keldysh}}$  the scattering rate is given by

$$\frac{1}{\tau_{\text{II}}} = S_{\text{Keldysh}} \left( \frac{E - E_{\text{th,Keldysh}}}{E_{\text{th,Keldysh}}} \right)^{C_{\text{Keldysh}}}. \quad (\text{B.12})$$

We use  $C_{\text{Keldysh}} = 2$ .

## B.6 Electron Intervalley Scattering

The pre-factor for electron intervalley scattering is [80]

$$P_{\text{intervalley}} = \frac{D_{\text{inter}}^2 (m^*)^{\frac{3}{2}} Z_{\text{f}}}{\sqrt{2\pi} \rho \hbar^3 \omega_{\text{i}}} \left( N_{\text{q}} + \frac{1}{2} \pm \frac{1}{2} \right). \quad (\text{B.13})$$

$D_{\text{inter}}$  is the intervalley deformation potential.  $m^*$  is the effective mass in the final valley.  $Z_{\text{f}}$  is the number of possible final valleys of the same type.  $\rho$  is the mass density and  $\omega_{\text{i}}$  is the phonon angular frequency of the phonon involved in the intervalley process.  $N_{\text{q}}$  is the phonon population. The scattering rate is [80]

$$\frac{1}{\tau_{\text{intervalley}}} = P_{\text{intervalley}} \sqrt{\gamma'} (1 + 2\alpha' E') \quad (\text{B.14})$$

with  $\gamma' = E'(1 + \alpha' E')$ .  $\alpha'$  is the non-parabolicity of the final valley. The final carrier energy for intravalley absorption and emission process is  $E' = E \mp \hbar\omega_{\text{op}} - \Delta E$  with  $\hbar\omega_{\text{op}}$  the optical phonon energy and  $\Delta E$  the energy difference between the valleys.

# Appendix C

## Monte Carlo Material Parameters

### C.1 $\text{In}_{0.53}\text{Ga}_{0.47}\text{As}$

parameter	this work	Brennan, Watanabe [59, 131]	Littlejohn [119]	Mateos [132]
$\rho$ ( $\text{kg}/\text{m}^3$ )	5480	5480	5482	5545
$\epsilon_s$ (1)	13.85	13.85	13.1	13.88
$\epsilon_\infty$ (1)	11.09	11.09	11.09	11.35
$v_l / v_t$ ( $\text{m}/\text{s}$ )	4550 / 3010	4550 / 3010	4101 / -	4756 / -
$a$ ( $10^{-10}$ m)	5.867	5.867	5.867	-
$E_{g,\Gamma_6}$ 300 K (eV)	0.743 [133]	0.77	0.77	0.70
$\hbar\omega_{opt}$ (meV)	32.7	32.7	32.71	32.8

Table C.1: General parameter for MC simulation of InGaAs.

	$\Gamma_6$	$L_6$	$X_6$	HH	LH	SO
$s_{\text{Keldysh}} (1/\text{ps})$	2100	2100	2100	25000	25000	25000
$E_{\text{th,Keldysh}} (\text{eV})$	1.125	1.125	1.125	0.95	0.95	0.95
$E_{\text{hard,Keldysh}} (\text{eV})$	1.8	1.8	1.8	1.2	1.2	1.2

Table C.2: Keldysh model parameter for electron and hole in InGaAs.

parameter	this work			Brennan, Watanabe [59, 131]		
	HH	LH	SO	HH	LH	SO
$D_{\text{alloy}} (\text{eV})$	0.2			0.2		
$\Delta E (\text{eV})$	0.0	0.0	0.325	0.0	0.0	0.325
$m_{\text{h}} (m^*/m_0)$	0.61	0.0588	0.123	0.61	0.588	0.123
$\alpha (1/\text{eV})$	0.85	1.0	0.01	-	-	-
$D_{\text{ac}} (\text{eV})$	5.0728 (accord. to [121])			-		
$C_{11} (10^{11} \text{ dynes/cm}^2)$	-			10.21		
$C_{12} (10^{11} \text{ dynes/cm}^2)$	-			4.98		
$C_{44} (10^{11} \text{ dynes/cm}^2)$	-			5.01		
$D_{\text{non-pop}} (10^{11} \text{ eV/m})$	1.1063 (accord. to [121])			-		
$a (\text{eV})$	-			2.607		
$b (\text{eV})$	-			-1.747		
$d (\text{eV})$	-			-4.104		

Table C.3: Hole parameter for MC simulation of InGaAs

parameter	this work			Brennan, Watanabe [59, 131]			Littlejohn [119]			Mateos [132]		
	$\Gamma_6$	L <sub>6</sub>	X <sub>6</sub>	$\Gamma_6$	L <sub>6</sub>	X <sub>6</sub>	$\Gamma_6$	L <sub>6</sub>	X <sub>6</sub>	$\Gamma_6$	L <sub>6</sub>	X <sub>6</sub>
$D_{\text{alloy}}$ (eV)		0.529			0.60			0.529			1.50	
$\Delta E$ (eV)	0.0	0.55	0.67	0.0	0.55	0.67	0.0	0.553	0.668	0.0	0.61	1.11
$m_e$ ( $m^*/m_0$ )	0.0463	0.256	0.529	0.0463	0.256	0.529	0.041	1.980 / 0.162	2.365 / 0.355	0.042	0.258	0.538
$\alpha$ (1/eV)	1.18	0.22	0.049	1.18	0.22	0.049	1.167	0.588	0.649	1.255	0.461	0.204
$D_{\text{acoustic}}$ (eV)	9.2	9.2	9.2	9.2	9.2	9.2	-	-	-	5.887	10.84	9.657
$D_{\text{non-pop}}$ ( $10^{10}$ eV)	0	3.0	0	-	-	-	-	-	-	0	3.0	0
$D_{\text{inter}}$ ( $10^8$ eV/cm)												
from $\Gamma_6$ -valley	0	10	10	0	10	10	0	7	7	0	7.83	11.32
from L <sub>6</sub> -valley	10	10	10	10	10	10	7	7	5	7.83	6.40	6.80
from X <sub>6</sub> -valley	10	10	10	10	10	10	7	5	5.8	11.32	6.80	8.54
$\hbar\omega_{\text{inter}}$ (meV)												
from $\Gamma_6$ -valley	-	29	29	-	29	29	-	22.76	23.84	-	25.4	25.7
from L <sub>6</sub> -valley	29	29	29	29	29	29	22.76	23.12	26.96	25.4	24.8	30.2
from X <sub>6</sub> -valley	29	29	29	29	29	29	23.84	26.96	22.76	25.7	30.2	28.4

Table C.4: Electron parameter for MC simulation of InGaAs.

## C.2 $\text{In}_{0.52}\text{Al}_{0.48}\text{As}$

parameter	this work	Brennan, Watanabe [59, 131]	Kim [62]	Mateos [132]
$\rho$ ( $\text{kg}/\text{m}^3$ )	4900	4750	4900	4878
$\epsilon_s$ (1)	12.46	12.42	12.46	12.42
$\epsilon_\infty$ (1)	9.84	10.28	9.84	10.23
$v_l / v_t$ ( $\text{m}/\text{s}$ )	4970 / 3270	4970 / 3270	-	4679 / -
$a$ ( $10^{-10}$ m)	5.867	5.867	-	-
$E_{g,\Gamma_6}$ 300 K (eV)	1.457 [133]	1.49	-	1.457
$\hbar\omega_{opt}$ (meV)	39.5	41	39.5	40.4

Table C.5: General parameter for MC simulation of InAlAs.

	$\Gamma_6$	$L_6$	$X_6$	HH	LH	SO
$s_{\text{Keldysh}}$ ( $1/\text{ps}$ )	6000	6000	6000	20000	20000	20000
$E_{\text{th,Keldysh}}$ (eV)	1.49	1.50	1.50	1.458	1.458	1.458
$E_{\text{hard,Keldysh}}$ (eV)	2.45	2.45	2.45	2.1	2.1	2.1

Table C.6: Keldish model parameter for electron and hole in InAlAs

parameter	this work			Brennan, Watanabe [59, 131]		
	HH	LH	SO	HH	LH	SO
$D_{\text{alloy}}$ (eV)	0.38			0.38		
$\Delta E$ (eV)	0.0	0.0	0.3325	0.0	0.0	0.3325
$m_{\text{h}}$ ( $m^*/m_0$ )	0.677	0.086	0.16	0.677	0.086	0.161
$\alpha$ ( $1/\text{eV}$ )	0.6	0.9	0.1	-	-	-
$D_{\text{ac}}$ (eV)	4.29372 (calc. accord. [121])			-		
$C_{11}$ ( $10^{11}$ dynes/cm <sup>2</sup> )	-			10.1		
$C_{12}$ ( $10^{11}$ dynes/cm <sup>2</sup> )	-			5.089		
$C_{44}$ ( $10^{11}$ dynes/cm <sup>2</sup> )	-			4.886		
$D_{\text{non-pop}}$ ( $10^{11}$ eV/m)	1.07975 (calc. accord. [121])			-		
$a$ (eV)	-			2.548		
$b$ (eV)	-			-1.656		
$d$ (eV)	-			-3.504		

Table C.7: Hole parameter for MC simulation of InAlAs

parameter	this work			Brennan, Watanabe [59,131]			Kim [62]			Mateos [132]		
	$\Gamma_6$	$L_6$	$X_6$	$\Gamma_6$	$L_6$	$X_6$	$\Gamma_6$	$L_6$	$X_6$	$\Gamma_6$	$L_6$	$X_6$
$D_{\text{alloy}}$ (eV)		0.47			0.46			0.47		0.47		
$\Delta E$ (eV)	0.0	0.34	0.6	0.0	0.16	0.22	0.0	0.34	0.6	0.0	0.50	0.60
$m_e$ ( $m^*/m_0$ )	0.07	0.390	0.602	0.084	0.274	0.496	0.07	0.390	0.602	0.083	0.304	0.496
$\alpha$ (1/eV)	0.843	0.552	0.588	0.571	0.204 / 0.25	0.204 / 0.147	0.843	0.552	0.588	0.543	0.415	0.204
$D_{\text{acoustic}}$ (eV)	8	8	8	8	8	8	-	-	-	5.93	7.23	9.02
$D_{\text{non-pop}}$ ( $10^{10}$ eV)	0	3.0	0	-	-	-	-	-	-	0	3.0	0
$D_{\text{inter}}$ ( $10^8$ eV/cm)												
from $\Gamma_6$ -valley	0	5	7.4	0	10	10	0	5	7.4	0	5.25	3.82
from $L_6$ -valley	5	5	5	10	10	10	5	5	5	5.25	6.55	8.60
from $X_6$ -valley	7.4	5	7.4	10	10	10	7.4	5	7.4	3.82	8.60	5.72
$h_{\text{inter}}$ (meV)												
from $\Gamma_{\text{ext}6}$ -valley	-	30.8	29.1	-	29	29	-	30.8	29.1	-	29.3	29.3
from $L_{\text{ext}6}$ -valley	30.8	31.1	36.0	29	29	29	30.8	31.1	36.0	29.3	30.3	32.2
from $X_{\text{ext}6}$ -valley	29.1	36.0	29.1	29	29	29	29.1	36.0	29.1	29.3	32.2	26.8

Table C.8: Electron parameter for MC simulation of InAlAs.

# Appendix D

## Scattering Rates

The scattering rates give insight into the major physical processes which determine dynamic and stationary characteristics. Fig. D.1 shows the electron scattering rates of InAlAs in the non-parabolic  $\Gamma$ -valley. At low energy combined polar optical phonon absorption and emission and impurity scattering are dominant. The impurity scattering in Fig. D.1 corresponds to a n-type doping of  $N_d = 10^{16} \text{ 1/cm}^3$  using the Ridley impurity scattering model [62]. Polar optical phonon emission is possible above the optical phonon energy of 39.5 meV which results in an increase in the combined scattering rate. At the valley separation energy between  $\Gamma$  to L and  $\Gamma$  to X, phonon assisted inter-valley scattering sets in. Elastic acoustic and alloy scattering rates are low in the  $\Gamma$ -valley which results from a low effective electron mass. Above impact ionization threshold, scattering due to impact ionization starts to increase and dominates the scattering in the high energy regime. The hard ionization threshold [86] at 2.45 eV results in an effective barrier for the carrier energy. Carriers above hard threshold are scatter by impact ionization which limits the maximal achievable energy in each valley. Only a small amount of impact ionization events are caused by the hard threshold condition for the electric fields present in our APDs. The total scattering rate for a parabolic conduction band approximation corresponds to the non-parabolic case up to an energy of approximately 100 meV as can be seen in Fig. 5.7(a). Above that energy the scattering rate for the

parabolic case is significantly lower which is due to the smaller density of states at higher energies. An increase of the scattering rate at high carrier energies for full band description is expected compared to the non-parabolic description.

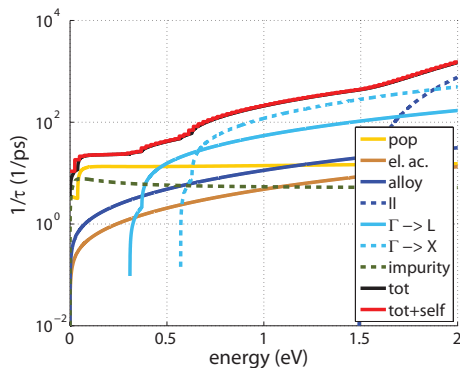


Figure D.1: Scattering rates for electrons in InAlAs:  $\Gamma$ -valley

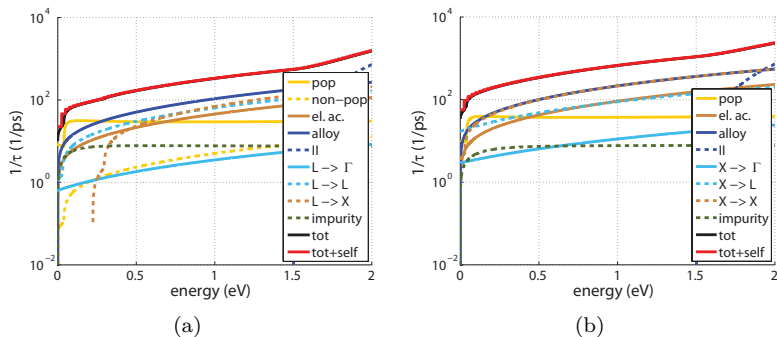


Figure D.2: Scattering rates for electrons in InAlAs: (a) L-valley, (b) X-valley.

The higher effective mass in the L-valley results in approximately 13 times higher alloy scattering rate compared to the  $\Gamma$ -valley (see

figure D.2). This is an important observation since the majority of the carriers will be found in the L-valley for high electric fields as shown in Fig. 6.4(b)). Therefore, the saturation velocity strongly depends on the electron effective mass in the L-valley and the alloy scattering rate.

Scattering rates for the HH- and LH-valley in InAlAs are shown in Fig. D.3. Intra- and inter-valley mechanisms are combined. A high alloy and non-polar optical phonon scattering can be observed.

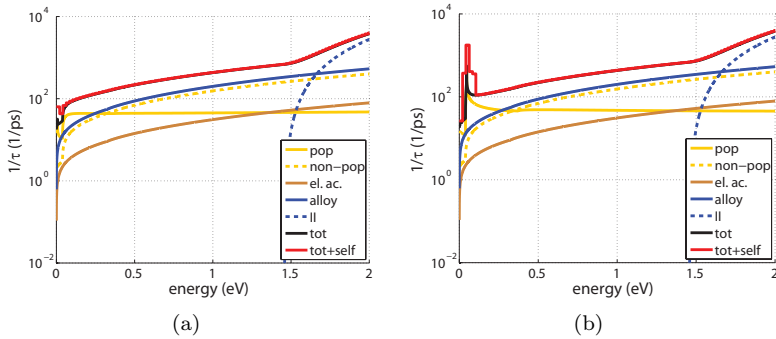


Figure D.3: Scattering rate for holes in InAlAs (a) HH-valley, (b) LH-valley.

In general a large variation of the total scattering rate between electron valleys, hole valleys and between low and high energy regime is observed. The amount of self-scattering is individually adjusted with respect to carrier type, valley, material properties such as doping and the energy interval (see Sec. 5.4.4).

The corresponding scattering rates for InGaAs are shown in Fig. D.4, Fig. D.5 and Fig. D.6

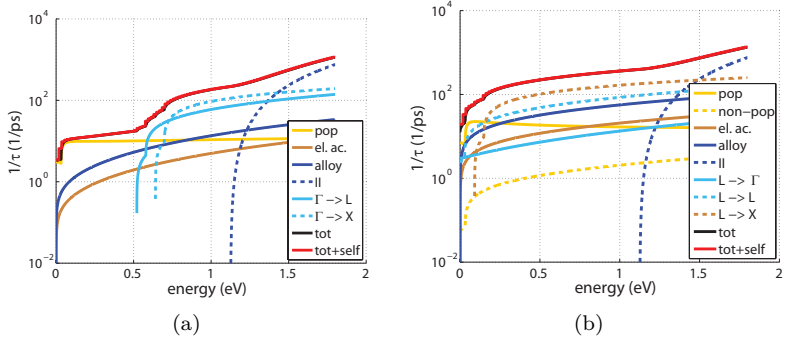
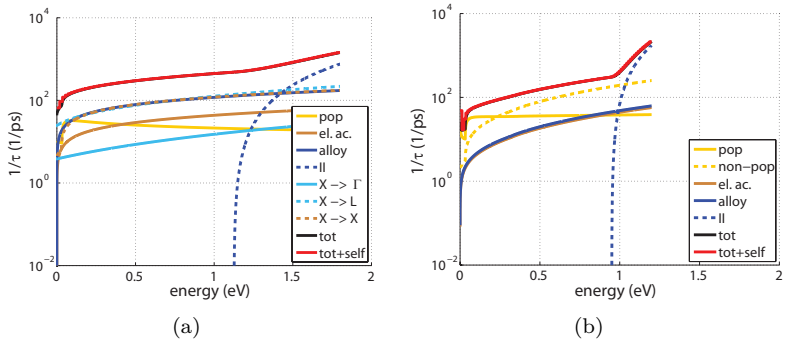
Figure D.4: InGaAs scattering rates: (a)  $\Gamma$ -valley, (b) L-valley

Figure D.5: InGaAs scattering rates: (a) X-valley, (b) HH-valley

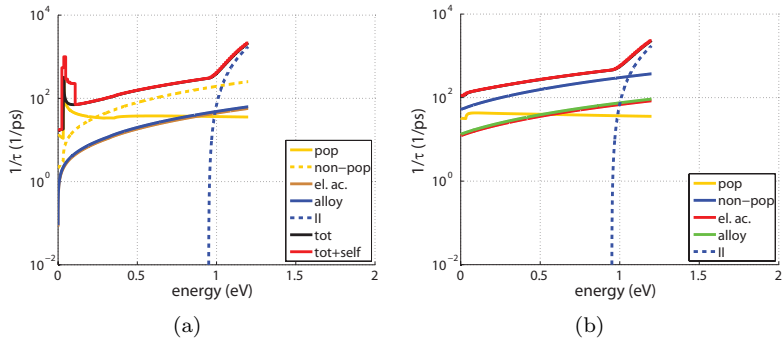


Figure D.6: InGaAs scattering rates: (a) LH-valley, (b) SO-valley



# Appendix E

## Drift-Diffusion Simulation Parameters

parameter	InAlAs	InGaAs	InAlGaAs
$\epsilon_s$ (1)	12.46 [62]	13.1 [119]	12.78
$E_g$ (eV)	1.47 [103]	0.75 [103]	1.12
$\Delta E_c$ (eV)	0	-0.504 [11, 103, 104]	-0.24

Table E.1: DD model parameter for CV simulation.

parameter	InAlAs		InGaAs	
	electron	hole	electron	hole
$m_{\text{DOS}}$ (1)	0.75 [134]	0.47 [134]	0.041 [134]	0.47 [134]
$\mu_0$ ( $\text{cm}^2/\text{Vs}$ )	4800 [135]	75 [134]	14000 [135]	320 [135]
$\mu_{\text{min}}$ ( $\text{cm}^2/\text{Vs}$ )	800 [135]	40 [134]	300 [135]	10 [135]
$C_r$ ( $1/\text{cm}^3$ )	$0.3 \cdot 10^{17}$ [135]	$0.3 \cdot 10^{17}$ [134]	$1.3 \cdot 10^{17}$ [135]	$4.9 \cdot 10^{17}$ [135]
$\alpha$ (1)	1.1 [135]	0.79 [134]	0.48 [135]	0.403 [135]
$v_{\text{sat}}$ (m/s)	$0.8e7$ [125]	$0.3e7$ [125]	$0.6e7$ [134]	$0.45e7$ [134]
$T_{\text{inj,SRH}}$ (s)	0	0	0	0
$T_{\text{max,SRH}}$ (s)	$1 \cdot 10^{-6}$	$1 \cdot 10^{-6}$	$1 \cdot 10^{-6}$	$1 \cdot 10^{-6}$
$N_{\text{ref,SRH}}$ ( $1/\text{cm}^3$ )	$1 \cdot 10^{16}$	$1 \cdot 10^{16}$	$1 \cdot 10^{16}$	$1 \cdot 10^{16}$
$a_{\text{II}}$ ( $1/\text{cm}$ )	$8.6 \cdot 10^6$ [18]	$2.3 \cdot 10^7$ [18]	$2.27 \cdot 10^6$ [126]	$3.95 \cdot 10^6$ [126]
$b_{\text{II}}$ ( $\text{V}/\text{cm}$ )	$3.5 \cdot 10^6$ [18]	$4.5 \cdot 10^6$ [18]	$1.13 \cdot 10^6$ [126]	$1.45 \cdot 10^6$ [126]

Table E.2: DD simulation parameter.

# Appendix F

## Static Dielectric Constant

Tab. F.1 summarizes possible values for the dielectric constant of the binary materials AlAs, InAs and GaAs obtained by measurements. In Tab. F.2 a summary of binary parameters used in other simulation work are shown. In general, the value for the ternary material is obtained by linear interpolation. Data found in literature for the use in simulation are summarized in Tab. F.3.

reference	$\epsilon_{s,AlAs}$	$\epsilon_{s,InAs}$	$\epsilon_{s,GaAs}$	remark
Guyaux et al. [136]	10.16	-	-	meas. 300 K
Fern et al. [137]	10.06	-	12.9	meas. 300 K
Lorimor et al. [138]	-	14.55	-	-
Hass et al. [139]	-	15.15	12.9	$\Delta\epsilon_{InAs} = 2.9$ , $\Delta\epsilon_{GaAs} = 2.0$
Seeger et al. [140]	-	-	12.8	meas. 300 K
Samara et al. [141]	-	-	13.18	meas. 300 K
Landolt-Boernstein	10.06-10.16	12.92-15.1	-	with $\Delta\epsilon_{InAs} = 2.9$ [139]

Table F.1: Values for the static dielectric constant of binary materials from measurements.

reference	$\epsilon_{s,\text{AlAs}}$	$\epsilon_{s,\text{InAs}}$	$\epsilon_{s,\text{GaAs}}$
Adachi et al. [142]	-	14.6	13.1
Brennan et al. [143]	-	14.55	12.9
Fischetti et al. [82]	10.06	15.15	12.9
Sotoodeh et al. [135]	10.06	15.15	12.9

Table F.2: Values for the static dielectric constant of binary materials found in secondary literature.

reference	$\epsilon_{s,\text{InAlAs}}$	$\epsilon_{s,\text{InGaAs}}$
Kim et al. [62]	12.46	-
Littlejohn et al. [119]	-	13.1
Watanabe et al. [59]	12.42	13.85
Mateos et al. [132]	12.42	13.88

Table F.3: Values for the static dielectric constant found in secondary literature.

# Bibliography

- [1] C.-H. Lee, W. V. Sorin, and B. Y. Kim, “Fiber to the home using a PON infrastructure,” *J. Lightwave Technol.*, vol. 24, no. 12, Dec. 2006.
- [2] K. Tanaka, A. Agata, and Y. Horiuchi, “IEEE 802.3av 10G-EPON standardization and its research and development status,” *J. Lightwave Technol.*, vol. 28, no. 4, pp. 651–661, 2010.
- [3] S. Alexander, *Optical Communication Receiver Design*. SPIE, 1997.
- [4] T. S. S. of ITU, *ITU-T G.984.1, Gigabit-capable passive optical networks (GPON): General Characteristics*, ITU.
- [5] “DARPA IPTO, exascale computing study report,” Sept. 2008.
- [6] S. Assefa, F. Xia, and Y. A. Vlasov, “Reinventing germanium avalanche photodetector for nanophotonic on-chip optical interconnects,” *Nature Letter*, vol. 464, pp. 80–84, Mar. 2010.
- [7] Y. Kang, H. Liu, M. Morse, M. J. Paniccia, M. Zadka, S. Litski, G. Sarid, A. Pauchard, Y. Kuo, H. Chen, W. S. Zaoui, J. E. Bowers, A. Beling, D. C. McIntosh, X. Zheng, and J. C. Campbell, “Monolithic germanium/silicon avalanche photodiodes with 340 GHz gain-bandwidth product,” *Nature Photonics*, vol. 3, pp. 59–63, Jan. 2009.
- [8] B. Saleh and M. Teich, *Fundamentals of Photonics*. Wiley, 1994.

- [9] C. N. Harrison, J. P. R. David, M. Hopkinson, and G. J. Rees, "Temperature dependence of avalanche multiplication in submicron  $\text{Al}_{0.6}\text{Ga}_{0.4}\text{As}$  diodes," *J. Appl. Phys.*, vol. 92, no. 12, pp. 7684–7686, 2002.
- [10] A. G. Chynoweth, "Ionization rates for electrons and holes in Silicon," *Phys. Rev.*, vol. 109, no. 5, pp. 1537–1540, Mar. 1958.
- [11] S. Chuang, *Physics of Optoelectronic Devices*. Wiley, 1995.
- [12] J. C. Campbell, "Recent advances in telecommunications avalanche photodiodes," *J. Lightwave Technol.*, vol. 25, no. 1, pp. 109–121, 2007.
- [13] S. G. E. and W. C. M., *Avalanche Photodiodes*, ser. Semiconductors and Semimetals. Academic, New York, 1977, vol. 12.
- [14] H. Ando, H. Kanbe, M. Ito, and T. Kaneda, "Tunneling current in InGaAs and optimum design for InGaAs/InP avalanche photodiode," *Jap. J. Appl. Phys.*, vol. 19, no. 6, pp. L277–L280, 1980.
- [15] K. A. Jackson, *Compound Semiconductor Devices*. Wiley-VCH, 1998.
- [16] B. Levine, R. Sacks, J. Ko, M. Jazwiecki, J. Valdmanis, D. Gunther, and J. Meier, "A new planar InGaAs/InAlAs avalanche photodiode," *IEEE Photon. Technol. Lett.*, vol. 18, no. 18, pp. 1898–1900, Sept. 2006.
- [17] S. Sze, *Physics of Semiconductor Devices*. Wiley, 1981.
- [18] I. Watanabe, T. Torikai, K. Makita, K. Fukushima, and T. Uji, "Impact ionization rates in (100)  $\text{Al}_{0.48}\text{In}_{0.52}\text{As}$ ," *IEEE Electron Device Lett.*, vol. 11, no. 10, pp. 437–438, Oct. 1990.
- [19] B. Ng, J. David, S. Plimmer, M. Hopkinson, R. Tozer, and G. Rees, "Impact ionization coefficients of  $\text{Al}_{0.8}\text{Ga}_{0.2}\text{As}$ ," *Appl. Phys. Lett.*, vol. 77, no. 26, pp. 4274–4376, Dec. 2000.

- [20] R. McIntyre, "The distribution of gains in uniformly multiplying avalanche photodiodes: Theory," *IEEE Trans. Electron Devices*, vol. 19, no. 6, pp. 703 – 713, June 1972.
- [21] A. R. Hawkins, T. E. Reynolds, D. R. England, D. I. Babic, M. J. Mondry, K. Streubel, and J. E. Bowers, "Silicon heterointerface photodetector," *Appl. Phys. Lett.*, vol. 68, no. 26, pp. 3692–3694, 1996.
- [22] J. D. Beck, C.-F. Wan, M. A. Kinch, and J. E. Robinson, "MWIR HgCdTe avalanche photodiodes," R. E. Longshore, Ed., vol. 4454, no. 1. SPIE, 2001, pp. 188–197.
- [23] F. Ma, X. Li, J. C. Campbell, J. D. Beck, C.-F. Wan, and M. A. Kinch, "Monte Carlo simulations of Hg<sub>0.7</sub>Cd<sub>0.3</sub>Te avalanche photodiodes and resonance phenomenon in the multiplication noise," *Appl. Phys. Lett.*, vol. 83, no. 4, pp. 785–787, 2003.
- [24] C. Skrimshire, J. Farr, D. Sloan, M. Robertson, P. Putland, J. Stokoe, and R. Sutherland, "Reliability of mesa and planar InGaAs PIN photodiodes," *IEE Proceedings J Optoelectron.*, vol. 137, no. 1, pp. 74 –78, Feb. 1990.
- [25] K. Taguchi, T. Torikai, Y. Sugimoto, K. Makita, and H. Ishihara, "Planar-structure InP/InGaAsP/InGaAs avalanche photodiodes with preferential lateral extended guard ring for 1.0–1.6  $\mu\text{m}$  wavelength optical communication use," *J. Lightwave Technol.*, vol. 6, no. 11, pp. 1643 –1655, Nov. 1988.
- [26] E. Ishimura, E. Yagyū, M. Nakaji, S. Ihara, K. Yoshiara, T. Aoyagi, Y. Tokuda, and T. Ishikawa, "Degradation mode analysis on highly reliable guardring-free planar InAlAs avalanche photodiodes," *J. Lightwave Technol.*, vol. 25, no. 12, pp. 3686 –3693, Dec. 2007.
- [27] R. Wei, J. Dries, H. Wang, M. Lange, G. Olsen, and S. Forrest, "Optimization of 10-gb/s long-wavelength floating guard ring InGaAs-InP avalanche photodiodes," *IEEE Photon. Technol. Lett.*, vol. 14, no. 7, pp. 977 –979, July 2002.

- [28] L. E. Tarof, D. G. Knight, K. E. Fox, C. J. Miner, N. Puetz, and H. B. Kim, “Planar InP/InGaAs avalanche photodetectors with partial charge sheet in device periphery,” *Appl. Phys. Lett.*, vol. 57, no. 7, pp. 670–672, 1990.
- [29] L. Tarof, R. Bruce, D. Knight, J. Yu, H. Kim, and T. Baird, “Planar InP-InGaAs single-growth avalanche photodiodes with no guard rings,” *IEEE Photon. Technol. Lett.*, vol. 7, no. 11, pp. 1330–1332, Nov. 1995.
- [30] “Internal communication with Enablence, Switzerland.”
- [31] S. Forrest, “Performance of InGaAsP photodiodes with dark current limited by diffusion, generation recombination, and tunneling,” *IEEE J. Quantum Electron.*, vol. 17, no. 2, pp. 217–226, Feb. 1981.
- [32] L. Tan, D. Ong, J. S. Ng, C. H. Tan, S. Jones, Y. Qian, and J. David, “Temperature dependence of avalanche breakdown in InP and InAlAs,” *IEEE J. Quantum Electron.*, vol. 46, no. 8, pp. 1153–1157, Aug. 2010.
- [33] A. Rouvie, D. Carpentier, N. Lagay, J. Decobert, F. Pomereau, and M. Achouche, “High gain times; bandwidth product over 140-GHz planar junction AlInAs avalanche photodiodes,” *IEEE Photon. Technol. Lett.*, vol. 20, no. 6, pp. 455–457, Mar. 2008.
- [34] N. Duan, S. Wang, X. Zheng, X. Li, J. C. Campbell, C. Wang, and L. A. Coldren, “Detrimental effect of impact ionization in the absorption region on the frequency response and excess noise performance of InGaAs-InAlAs SACM avalanche photodiodes,” *IEEE J. Quantum Electron.*, vol. 41, no. 4, pp. 568–572, 2005.
- [35] R. McIntyre, “Multiplication noise in uniform avalanche diodes,” *IEEE Trans. Electron Devices*, vol. 13, no. 1, pp. 164–168, Jan. 1966.
- [36] G. P. Agrawal, *Encyclopedia of Laser Physics and Technology*. Wiley-VCH, 2008, vol. 1.

- [37] R. Paschotta, *Fiber-Optical Communication Systems*, ser. Series in Microwave and Optical Engineering. Wiley-Interscience, 2002.
- [38] G. Valley, *Vacuum Tube Amplifiers*. McGraw-Hill, 1948.
- [39] G. Ghione, *Semiconductor Devices for High-Speed Optoelectronics*. Cambridge University Press, 2009.
- [40] T. Tille, *Mikroelektronik*. Springer, 2005.
- [41] H. Meier and B. Witzigmann, “Investigation of bandwidth limitations in separate absorption, charge and multiplication (SACM) avalanche photodiodes (APD),” in *Conference on Lasers and Electro-Optics/Quantum Electronics and Laser Science Conference and Photonic Applications Systems Technologies*. Optical Society of America, 2008, p. CWF5.
- [42] I. Watanabe, S. Sogou, H. Ishikawa, T. Anan, K. Makita, M. Tsuji, and K. Taguchi, “High-speed and low-dark-current flip-chip InAlAs/InAlGaAs quaternary well superlattice APD’s with 120 GHz gain-bandwidth product,” *IEEE Photon. Technol. Lett.*, vol. 5, no. 6, pp. 675–677, June 1993.
- [43] Y. Hirota, S. Ando, and T. Ishibashi, “High-speed avalanche photodiode with a neutral absorber laser for 1.55  $\mu\text{m}$  wavelength,” *Jap. J. Appl. Phys.*, vol. 43, no. 3A, pp. 375–377, 2004.
- [44] C. Lenox, H. Nie, P. Yuan, G. Kinsey, A. Holmes, B. Streetman, and J. Campbell, “Resonant-cavity InGaAs-InAlAs avalanche photodiodes with gain-bandwidth product of 290 GHz,” *IEEE Photon. Technol. Lett.*, vol. 11, no. 9, pp. 1162–1164, Sept. 1999.
- [45] N. Li, R. Sidhu, X. Li, F. Ma, X. Zheng, S. Wang, G. Karve, S. Demiguel, A. L. Holmes, and J. C. Campbell, “In-GaAs/InAlAs avalanche photodiode with undepleted absorber,” *Appl. Phys. Lett.*, vol. 82, no. 13, pp. 2175–2177, Mar. 2003.
- [46] S. Shimizu, K. Shiba, T. Nakata, K. Kasahara, and K. Makita, “40 Gbit/s waveguide avalanche photodiode with p-type absorption layer and thin InAlAs multiplication layer,” *Electronics Letters*, vol. 43, no. 8, Apr. 2007.

- [47] H. Ito, S. Kodoma, Y. Muramoto, T. Furuta, T. Nagatsuma, and T. Ishibashi, "High-speed and high-output InP-InGaAs unitraveling-carrier photodiodes," *IEEE J. Sel. Top. Quantum Electron.*, vol. 10, no. 4, pp. 709–727, July 2004.
- [48] E. Harmon, M. Lovejoy, M. Melloch, M. Lundstrom, D. Ritter, and R. Hamm, "Minority-carrier mobility enhancement in p+ InGaAs lattice matched to InP," *Appl. Phys. Lett.*, vol. 63, no. 2, pp. 636–638, Aug. 1993.
- [49] N. Shimizu, N. Watanabe, T. Furuta, and T. Ishibashi, "InP-InGaAs uni-traveling-carrier photodiode with improved 3-dB bandwidth over 150 GHz," *IEEE Photon. Technol. Lett.*, vol. 10, no. 3, pp. 412–414, Mar. 1998.
- [50] S. Forrest, O. Kim, and R. Smith, "Optical response time of In<sub>0.53</sub>Ga<sub>0.47</sub>As/InP avalanche photodiodes," *Appl. Phys. Lett.*, vol. 31, no. 1, pp. 95–98, July 1982.
- [51] R. Emmons, "Avalanche-photodiode frequency response," *J. Appl. Phys.*, vol. 38, no. 9, pp. 3705–3714, Aug. 1967.
- [52] J. C. Campbell, S. Demiguel, F. Ma, A. Beck, X. Guo, S. Wang, X. Zheng, X. Li, J. D. Beck, M. A. Kinch, A. Huntington, L. A. Coldren, J. Decobert, and N. Tschertner, "Recent advances in avalanche photodiodes," *IEEE J. Sel. Top. in Quantum Electron.*, vol. 10, no. 4, pp. 777–787, July 2004.
- [53] G. Kinsey, J. Campbell, and A. Dentai, "Waveguide avalanche photodiode operating at 1.55  $\mu\text{m}$  with a gain-bandwidth product of 320 GHz," *IEEE Photon. Technol. Lett.*, vol. 13, no. 8, pp. 842–844, Aug. 2001.
- [54] T. Nakata, T. Takeuchi, K. Makita, Y. Amamiya, Y. Suzuki, and T. Torikai, "An ultra high speed waveguide avalanche photodiode for 40-Gb/s optical receiver," *Proc. of 27th ECOC*, 2001.
- [55] Y. Goh, A. Marshall, D. Massey, J. Ng, C. Tan, M. Hopkinson, J. David, S. Jones, C. Button, and S. Pinches, "Excess avalanche

- noise in  $\text{In}_{0.52}\text{Al}_{0.48}\text{As}$ ,” *IEEE J. Quantum Electron.*, vol. 43, no. 6, pp. 503–507, June 2007.
- [56] P. Yuan, S. Wang, X. Sun, X. Zheng, A. Holmes, and J. C. Campbell, “Avalanche photodiodes with an impact-ionization-engineered multiplication region,” *IEEE Photon. Technol. Lett.*, vol. 12, no. 10, pp. 1370–1372, Oct. 2000.
- [57] S. Wang, R. Sidhu, X. Zheng, X. Li, X. Sun, A. Holmes, and J. C. Campbell, “Low-noise avalanche photodiodes with graded impact-ionization-engineered multiplication region,” *IEEE Photon. Technol. Lett.*, vol. 13, no. 12, pp. 1346–1348, Dec. 2001.
- [58] N. Duan, S. Wang, F. Ma, N. Li, J. Campbell, and L. A. Coldren, “High-speed and low-noise SACM avalanche photodiode with an impact-ionization-engineered multiplication region,” *IEEE Photon. Technol. Lett.*, vol. 17, no. 8, pp. 1719–1721, Aug. 2005.
- [59] I. Watanabe, T. Torikai, and K. Taguchi, “Monte Carlo simulation of impact ionization rates in  $\text{InAlAs-InGaAs}$  square and graded barrier superlattice,” *IEEE J. Quantum Electron.*, vol. 31, no. 10, pp. 1826–1834, 1995.
- [60] I. Watanabe, M. Tsuji, K. Makita, and K. Taguchi, “Gain-bandwidth product analysis of  $\text{InAlGaAs-InAlAs}$  superlattice avalanche photodiodes,” *IEEE Photon. Technol. Lett.*, vol. 8, no. 2, pp. 269–271, 1996.
- [61] Qucs, *Quite Universal Circuit Simulator, User Manual*. <http://qucs.sourceforge.net/docs.html>, 2010.
- [62] H. S. Kim, H. Tian, K. W. Kim, and M. A. Littlejohn, “Electron velocity-field characteristics of  $\text{In}_{0.52}\text{Al}_{0.48}\text{As}$ ,” *Appl. Phys. Lett.*, vol. 61, no. 10, pp. 1202–1204, 1992.
- [63] T. Grasser, T.-W. Tang, H. Kosina, and S. Selberherr, “A review of hydrodynamic and energy-transport models for semiconductor device simulation,” *Proc. of IEEE*, vol. 91, no. 2, pp. 251–274, Feb. 2003.

- [64] K. Y. Choo and D. S. Ong, "The applicability of analytical-band Monte Carlo for modelling high field electron transport in GaAs," *Semicond. Sci. and Technol.*, vol. 19, no. 8, p. 1067, 2004.
- [65] D. S. Ong, K. F. Li, S. A. Plimmer, G. J. Rees, J. P. R. David, and P. N. Robson, "Full band Monte Carlo modeling of impact ionization, avalanche multiplication, and noise in submicron GaAs p+-i-n+ diodes," *J. Appl. Phys.*, vol. 87, no. 11, pp. 7885–7891, June 2000.
- [66] F. M. Buffer, A. Schenk, and W. Fichtner, "Efficient Monte Carlo device modeling," *IEEE Trans. Electron Devices*, vol. 47, pp. 1891–1897, 2000.
- [67] A. Schenk, *Advanced Physical Models for Silicon Device Simulation*, ser. Computational Microelectronics, S. Selberherr, Ed. SpringerWienNewYork, 1998.
- [68] F. Capasso, T. Pearsall, and K. Thornber, "The effect of collisional broadening on Monte Carlo simulations of high-field transport in semiconductor devices," *IEEE Electron Device Lett.*, vol. 2, no. 11, pp. 295 – 297, Nov. 1981.
- [69] M. Lundstrom, *Fundamentals of Carrier Transport*, 2nd ed. Cambridge University Press, 2000.
- [70] E. Azoff, "Generalized energy-momentum conservation equations in the relaxation time approximation," *Solid-State Electron.*, vol. 30, no. 9, pp. 913–917, 1987.
- [71] M. V. Fischetti, D. J. DiMaria, S. D. Brorson, T. N. Theis, and J. Kirtley, "Theory of high-field electron transport in silicon dioxide," *Phys. Rev. B*, vol. 31, no. 12, pp. 8124–8142, June 1985.
- [72] V. Bonc-Bruevic and S. Kalasnikov, *Halbleiterphysik*. VEB Deutscher Verlag der Wissenschaften, 1982.
- [73] J. Barker, "High field collision rates in polar semiconductors," *Solid-State Electron.*, vol. 21, no. 1, pp. 267 – 271, 1978.

- [74] R. McIntyre, "A new look at impact ionization-part i: A theory of gain, noise, breakdown probability, and frequency response," *IEEE Trans. Electron Devices*, vol. 46, no. 8, pp. 1623–1631, Aug. 1999.
- [75] P. Yuan, K. Anselm, C. Hu, H. Nie, C. Lenox, A. Holmes, B. Streetman, J. Campbell, and R. McIntyre, "A new look at impact ionization-part ii: Gain and noise in short avalanche photodiodes," *IEEE Trans. Electron Devices*, vol. 46, no. 8, pp. 1632–1639, Aug. 1999.
- [76] M. Hayat, B. Saleh, and M. Teich, "Effect of dead space on gain and noise of double-carrier-multiplication avalanche photodiodes," *IEEE Trans. Electron Devices*, vol. 39, no. 3, pp. 546–552, Mar. 1992.
- [77] A. Spinelli and A. Lacaita, "Mean gain of avalanche photodiodes in a dead space model," *IEEE Trans. Electron Devices*, vol. 43, no. 1, pp. 23–30, Jan. 1996.
- [78] B. Jacob, P. N. Robson, J. P. R. David, and G. J. Rees, "Fokker-Planck approach to impact ionization distributions in space and time," *J. Appl. Phys.*, vol. 91, no. 8, pp. 5438–5441, Apr. 2002.
- [79] X. Li, X. Zheng, S. Wang, F. Ma, and J. Campbell, "Calculation of gain and noise with dead space for GaAs and  $\text{Al}_x\text{Ga}_{1-x}\text{As}$  avalanche photodiode," *IEEE Trans. Electron Devices*, vol. 49, no. 7, pp. 1112–1117, July 2002.
- [80] C. Jacoboni and L. Reggiani, "The Monte Carlo method for the solution of charge transport in semiconductors with applications to covalent materials," *Rev. Mod. Phys.*, vol. 55, no. 3, pp. 645–705, July 1983.
- [81] S. Ramaswamy and T.-W. Tang, "Comparison of semiconductor transport models using a Monte Carlo consistency test," *IEEE Trans. Electron Devices*, vol. 41, no. 1, pp. 76–83, Jan. 1994.
- [82] M. V. Fischetti, "Monte Carlo simulation of transport in technologically significant semiconductors of the diamond and

- zinc-blende structures - part i: Homogeneous transport," *IEEE Trans. Electron Devices*, vol. 38, no. 3, pp. 634–649, Mar. 1991.
- [83] S. Plimmer, J. David, D. Ong, and K. Li, "A simple model for avalanche multiplication including deadspace effects," *IEEE Trans. Electron Devices*, vol. 46, no. 4, pp. 769–775, Apr. 1999.
- [84] P. J. Hambleton, S. A. Plimmer, J. P. R. David, G. J. Rees, and G. M. Dunn, "Simulated current response in avalanche photodiodes," *J. Appl. Phys.*, vol. 91, no. 4, pp. 2107–2111, 2002.
- [85] P. Hambleton, B. Ng, S. Plimmer, J. David, and G. Rees, "The effects of nonlocal impact ionization on the speed of avalanche photodiodes," *IEEE Trans. Electron Devices*, vol. 50, no. 2, pp. 347–351, Feb. 2003.
- [86] G. Dunn, G. Rees, J. David, S. Plimmer, and D. Herbert, "Monte Carlo simulation of impact ionization and current multiplication in short GaAs pin diodes," *Semicond. Sci. Technol.*, vol. 12, pp. 111–120, 1997.
- [87] S. Chen, K. Xu, and G. Wang, "Monte Carlo investigation of size-dependent impact ionization properties in InP under submicron scale," *J. Lightwave Technol.*, vol. 27, no. 10, pp. 1347–1354, 2009.
- [88] F. Ma, S. Wang, X. Li, K. A. Anselm, X. G. Zheng, A. L. Holmes, and J. C. Campbell, "Monte Carlo simulation of low-noise avalanche photodiodes with heterojunctions," *J. Appl. Phys.*, vol. 92, pp. 4791–4795, Oct. 2002.
- [89] F. Ma, N. Li, and J. Campbell, "Monte Carlo simulations of the bandwidth of InAlAs avalanche photodiodes," *IEEE Trans. Electron Devices*, vol. 50, no. 11, pp. 2291–2294, Nov. 2003.
- [90] D. S. Ong, G. J. Rees, and J. P. R. David, "Avalanche speed in thin avalanche photodiodes," *J. Appl. Phys.*, vol. 93, no. 7, pp. 4232–4239, 2003.

- [91] V. Chandramouli, C. Maziar, and J. Campbell, "Design considerations for high performance avalanche photodiode multiplication layers," *IEEE Trans. Electron Devices*, vol. 41, no. 5, pp. 648–654, May 1994.
- [92] C. Jacoboni and P. Lugli, *The Monte Carlo Method for Semiconductor Device Simulation*, ser. Computational Microelectronics, S. Selberherr, Ed. SpringerWienNewYork, 1989.
- [93] C. Jungemann and B. Meinerzhagen, *Hierarchical Device Simulation - A Monte-Carlo Perspective*, ser. Computational Microelectronics, S. Selberherr, Ed. SpringerWienNewYork, 2003.
- [94] K. Tomizawa, *Numerical Simulation of Submicron Semiconductor Devices*. Artech House, 1993.
- [95] M. V. Fischetti and S. E. Laux, "Monte Carlo analysis of electron transport in small semiconductor devices including band-structure and space-charge effects," *Phys. Rev. B*, vol. 38, no. 14, pp. 9721–9745, Nov. 1988.
- [96] R. W. Hockney and J. W. Eastwood, *Computer Simulation Using Particles*. McGraw-Hill, 1981.
- [97] W. Fawcett, A. Boardman, and S. Swain, "Monte Carlo determination of electron transport properties in gallium arsenide," *J. Phys. Chem. Solids*, vol. 31, pp. 1963–1990, 1970.
- [98] G. U. Jensen, B. Lund, T. A. Fjeldly, and M. Shur, "Monte Carlo simulation of semiconductor devices," *Computer Physics Communications*, vol. 67, no. 1, pp. 1–61, 1991.
- [99] T. Brudevoll, T. A. Fjeldly, J. Baek, and M. S. Shur, "Scattering rates for holes near the valence-band edge in semiconductors," *J. Appl. Phys.*, vol. 67, no. 12, pp. 7373–7382, June 1990.
- [100] J. R. Hauser, M. A. Littlejohn, and T. H. Glisson, "Velocity-field relationship of InAs-InP alloys including the effects of alloy scattering," *Appl. Phys. Lett.*, vol. 28, no. 8, pp. 458–461, 1976.

- [101] B. Ridley, *Quantum Processes in Semiconductors*. Oxford Science Publications, 1995.
- [102] K. Kim and K. Hess, “Ensemble Monte Carlo simulation of semiclassical nonlinear electron transport across heterojunction band discontinuities,” *Solid-State Electronics*, vol. 31, no. 5, pp. 877 – 885, 1988.
- [103] S. Adachi, *Physical Properties of III-V Semiconductor Compounds*. Wiley-VCH, 2004.
- [104] J. Böhrer, A. Krost, and D. B. Bimberg, “Composition dependence of band gap and type of lineup in  $\text{In}_{1-x-y}\text{Ga}_x\text{Al}_y\text{As}/\text{InP}$  heterostructures,” *Appl. Phys. Lett.*, vol. 63, no. 14, pp. 1918–1920, 1993.
- [105] A. Messiah, *Quantum Mechanics*, ser. Computational Microelectronics. Dover Publications, 1999.
- [106] G. Mazzeo, E. Yablonovitch, H. W. Jiang, Y. Bai, and E. A. Fitzgerald, “Conduction band discontinuity and electron confinement at the  $\text{Si}_x\text{Ge}_{1-x}/\text{Ge}$  interface,” *Appl. Phys. Lett.*, vol. 96, no. 21, pp. 213 501 –213 501–3, May 2010.
- [107] C. Wordelman, T. Kwan, and C. Snell, “Comparison of statistical enhancement methods for Monte Carlo semiconductor simulation,” *IEEE Trans. Computer-Aided Design of Integrated Circuits and Systems*, vol. 17, no. 12, pp. 1230 –1235, Dec. 1998.
- [108] A. Pacelli and U. Ravaioli, “Analysis of variance-reduction schemes for ensemble Monte Carlo simulation of semiconductor devices,” *Solid-State Electronics*, vol. 41, no. 4, pp. 599 – 605, 1997.
- [109] C. Jungemann, *Methoden zur Simulation hochenergetischer Elektronen in Ultrakurzkanaltransistoren*. Verlag Shaker, 1995.
- [110] E. Sangiorgi, B. Ricco, and F. Venturi, “MOS2: an efficient MOnTe Carlo Simulator for MOS devices,” *Computer-Aided Design of Integrated Circuits and Systems, IEEE Transactions on*, vol. 7, no. 2, pp. 259 –271, Feb. 1988.

- [111] J. M. Miranda, C. Lin, M. Shaalan, H. L. Hartnagel, and J. L. Sebastian, "Influence of the minimization of self-scattering events on the Monte Carlo simulation of carrier transport in III-V semiconductors," *Semiconductor Science and Technology*, vol. 14, no. 9, p. 804, 1999.
- [112] P. Palestri, N. Barin, D. Esseni, and C. Fiegna, "Stability of self-consistent Monte Carlo simulations: effects of the grid size and of the coupling scheme," *IEEE Trans. Electron Devices*, vol. 53, no. 6, pp. 1433 – 1442, June 2006.
- [113] P. Rambo and J. Denavit, "Time stability of Monte Carlo device simulation," *IEEE Trans. Computer-Aided Design of Integrated Circuits and Systems*, vol. 12, no. 11, pp. 1734 –1741, Nov. 1993.
- [114] T. González and D. Pardo, "Physical models of ohmic contact for Monte Carlo device simulation," *Solid-State Electronics*, vol. 39, no. 4, pp. 555 – 562, 1996.
- [115] F. M. Bufler, A. Schenk, and W. Fichtner, "Proof of a simple time-step propagation scheme for Monte Carlo simulation," *Math. Comput. Simul.*, vol. 62, no. 3-6, pp. 323–326, 2003.
- [116] Synopsys, *Sentaurus Device User Guide, Version Z-2007.03*, Mar. 2007.
- [117] C. Jungemann and B. Meinerzhagen, "On the applicability of nonself-consistent Monte Carlo device simulations," *IEEE Trans. Electron Devices*, vol. 49, no. 6, pp. 1072 –1074, June 2002.
- [118] S. Laux and M. Fischetti, "Issues in modeling small devices," in *Electron Devices Meeting, 1999. IEDM Technical Digest. International*, 1999, pp. 523 –526.
- [119] T. H. Littlejohn M.A., Kim K.W., "High field transport in InGaAs and related heterostructures." Bhattacharya P., 1993.
- [120] T. Windhorn, L. Cook, and G. Stillman, "The electron velocity-field characteristic for n-In<sub>0.53</sub>Ga<sub>0.47</sub>As at 300 K," *IEEE Electron Dev. Lett.*, vol. 3, no. 1, pp. 18 – 20, Jan. 1982.

- [121] K. Brennan and K. Hess, "Theory of high-field transport of holes in GaAs and InP," *Phys. Rev. B*, vol. 29, no. 10, pp. 5581–5590, May 1984.
- [122] P. Hill, J. Schlafer, W. Powazinik, M. Urban, E. Eichen, and R. Olshansky, "Measurement of hole velocity in n-type InGaAs," *Appl. Phys. Lett.*, vol. 50, no. 18, pp. 1260–1262, 1987.
- [123] G.-G. Zhou, A. Fischer-Colbrie, and J. Harris, J.S., "I-V kink in InAlAs/InGaAs MODFETs due to weak impact ionization process in the InGaAs channel," Mar. 1994, pp. 435–438.
- [124] V. Palankovski and R. Quay, *Analysis and Simulation of Heterostructure Devices*, ser. Computational Microelectronics, S. Selberherr, Ed. SpringerWienNewYork, 2004.
- [125] I. Ashour, H. El Kadi, K. Sherif, J.-P. Vilcot, and D. Decoster, "Cutoff frequency and responsivity limitation of AlInAs/GaInAs MSM PD using a two dimensional bipolar physical model," *IEEE Trans. Electron Devices*, vol. 42, no. 2, pp. 231–238, Feb. 1995.
- [126] F. Osaka and T. Mikawa, "Excess noise design of InP/GaInAsP/GaInAs avalanche photodiodes," *IEEE J. Quantum Electron.*, vol. 22, no. 3, pp. 471–478, Mar. 1986.
- [127] Y. Goh, D. Massey, A. Marshall, J. Ng, C. Tan, W. Ng, G. Rees, M. Hopkinson, J. David, and S. Jones, "Avalanche multiplication in InAlAs," *IEEE Trans. Electron Devices*, vol. 54, no. 1, pp. 11–16, Jan. 2007.
- [128] W. Johnson and P. Panousis, "The influence of debye length on the C-V measurement of doping profiles," *IEEE Trans. Electron Devices*, vol. 18, no. 10, pp. 965–973, Oct. 1971.
- [129] H. Kroemer, W. a. Chien, J. S. Harris, and D. D. Edwall, "Measurement of isotype heterojunction barriers by C-V profiling," *Appl. Phys. Lett.*, vol. 36, no. 4, pp. 295–297, Feb. 1980.

- [130] M. Ogawa, H. Matsubayashi, H. Ohta, and T. Miyoshi, "Accurate parameter extraction of heterojunctions based on inverse C-V simulation," *Solid-State Electronics*, vol. 38, no. 6, pp. 1197 – 1207, 1995.
- [131] K. Brennan, "Theoretical study of multi-quantum well avalanche photodiodes made from the GaInAs/AlInAs material system," *IEEE Trans. Electron Devices*, vol. 33, no. 10, pp. 1502 – 1510, Oct. 1986.
- [132] J. Mateos, T. Gonzalez, D. Pardo, V. Hoel, H. Happy, and A. Cappy, "Improved Monte Carlo algorithm for the simulation of delta-doped AlInAs/GaInAs HEMTs," *IEEE Trans. Electron Devices*, vol. 47, no. 1, pp. 250 – 253, Jan. 2000.
- [133] R. Dittrich and W. Schroeder, "Empirical pseudopotential band structure of  $\text{In}_{0.53}\text{Ga}_{0.47}\text{As}$  and  $\text{In}_{0.52}\text{Al}_{0.48}\text{As}$ ," *Solid-State Electronics*, vol. 43, no. 2, pp. 403 – 407, 1999.
- [134] S. Datta, S. Shi, K. Roenker, M. Cahay, and W. Stanchina, "Simulation and design of InAlAs/InGaAs pnp heterojunction bipolar transistors," *IEEE Trans. Electron Devices*, vol. 45, no. 8, pp. 1634 – 1643, Aug. 1998.
- [135] M. Sotoodeh, A. H. Khalid, and A. A. Rezazadeh, "Empirical low-field mobility model for III-V compounds applicable in device simulation codes," *J. Appl. Phys.*, vol. 87, no. 6, pp. 2890–2900, 2000.
- [136] J. Guyaux, A. Degiovanni, P. Thiry, R. Sporcken, and R. Caudano, "Investigation of the AlAsGaAs interface by high resolution electron energy loss spectroscopy," *Appl. Surf. Sci.*, vol. 56-58, no. Part 2, pp. 697 – 702, 1992.
- [137] R. E. Fern and A. Onton, "Refractive index of AlAs," *J. Appl. Phys.*, vol. 42, no. 9, pp. 3499–3500, 1971.
- [138] O. G. Lorimor and W. G. Spitzer, "Infrared refractive index and absorption of InAs and CdTe," *J. Appl. Phys.*, vol. 36, no. 6, pp. 1841–1844, 1965.

- [139] M. Hass and B. Hennis, "Infrared lattice reflection spectra of III-V compound semiconductors," *J. Phys. and Chem. of Sol.*, vol. 23, no. 8, pp. 1099 – 1104, 1962.
- [140] K. Seeger, "Temperature dependence of the dielectric constants of semi-insulating III-V compounds," *Appl. Phys. Lett.*, vol. 54, pp. 1268–1269, Mar. 1989.
- [141] G. A. Samara, "Temperature and pressure dependences of the dielectric constants of semiconductors," *Phys. Rev. B*, vol. 27, no. 6, pp. 3494–3505, Mar. 1983.
- [142] S. Adachi, "Material parameters of  $\text{In}_{1-x}\text{Ga}_x\text{As}_y\text{P}_{1-y}$  and related binaries," *J. Appl. Phys.*, vol. 53, no. 12, pp. 8775–8792, 1982.
- [143] K. Brennan and K. Hess, "High field transport in GaAs, InP and InAs," *Solid-State Electron.*, vol. 27, no. 4, pp. 347 – 357, 1984.